Structure and Electronic Properties of Epitaxial Monolayer WSe$_2$

Von der Fakultät Mathematik und Physik der Universität Stuttgart zur Erlangung der Würde eines Doktors der Naturwissenschaften (Dr. rer. nat.) genehmigte Abhandlung

Vorgelegt von

Avaise Mohammed
aus
Visakhapatnam (Republik Indien)

Hauptberichter	Prof. Dr. Hidenori Takagi
Mitberichter	Prof. Dr. Martin Dressel
Prüfungsvorsitzende	Prof. Dr. Maria Daghofer
Tag der Einreichung	28th August, 2019
Tag der mündlichen Prüfung	11th Oktober, 2019

Max-Planck-Institut für Festkörperforschung
Universität Stuttgart
Deutschland

2019

Contents

Declaration

I declare that this work was done at Max Planck Institute for Solid State Research in Stuttgart and is not used either partially, or completely for any other degree at the University of Stuttgart, or any other institution.

Avaise Mohammed

Abstract

The impact created by the discovery of graphene has been one of the most spectacular ones in condensed matter physics [1, 2]. Although endowed with many exotic structural and electronic properties, its use is limited in electronic devices due to the lack of a band gap. The search has been carried out since to find other low dimensional systems with a non-zero band gap to be used in the development of functional electronic devices [3]. In this regard, transition metal dichalcogenides (TMDCs) are stepping up as one of the candidates. In addition to a finite band gap, the lack of the inversion symmetry and presence of a strong spin-orbit coupling (SOC) makes TMDC an exciting material system to study [4–6].

In order to understand the properties of TMDCs, it is essential to have a reliable method of synthesis and accessibility to manipulate their structural and electronic properties. Many methods are available for the synthesis of thin films such as, exfoliation, chemical vapour deposition (CVD) and molecular beam epitaxy (MBE). Although the thin films, including monolayers, grown by these methods lack a few desirable properties, the research into the physics and device applications has not slowed down. Among TMDCs, monolayer (ML) WSe_2 attracted considerable attention due to its large spin splitting, owing to the aforementioned strong SOC and the broken inversion symmetry, in the valance band.

However, the reported experimental values of the spin splitting are scattered over a wide range. It is speculated that the variation to have an origin in the strain [7]. However, there is no precise strain data available as of now. Furthermore, most of electronic transport studies were limited to responses of resistance to the temperature and the gate voltage. Little work has been done to reveal the spin physics via transport, especially in an atomically thin WSe_2.

The motivation of the present thesis is to synthesize epitaxial tungsten diselenide (WSe_2) thin films down to the ML limit using a modified (*hybrid-*) pulsed laser deposition (*h*-PLD). This will provide us an opportunity to investigate the precise structural and electronic properties. We compare our experimental data with our first principles calculations of the electronic band structure to obtain an experimental reference point of the spin splitting with respect to the strain. Furthermore, we hole dope WSe_2 thin films to study the spin properties of the charge carriers in the valance band. With this, we intend to answer some of the open questions from the previous studies in the properties of atomically thin WSe_2, including monolayer.

Multiple experimental techniques were employed to confirm the monolayer. In-situ reflection high energy electron diffraction (RHEED) is used to identify the ML WSe_2 with the evolution of line streaks in the two dimensional (2D) limit replacing the three dimensional (3D) Bragg spots of the bulk substrate. Thereafter, Raman scattering is used to distinguish the ML WSe_2 using the absence of 310 cm^{-1} which, in contrast, develops in bilayer and thicker thin films of WSe_2. These techniques are being widely used among TMDC researchers to identify ML from thicker flakes after exfoliation. In addition, atomic force microscopy (AFM) is used to map the surface morphology and identify the islands of WSe_2 on different substrates.

After demonstrating that the monolayer of WSe_2 could be fabricated by PLD, we focus on quantitative evaluation of their lattice structure, which is essential in examining the strain effect.

Synchrotron based X-ray diffraction (XRD) and grazing incidence X-ray diffraction (GIXRD) are used to study the crystal structure of ML WSe_2. We have found the orientation locking between the ML WSe_2 and the substrates. WSe_2 [10$\bar{1}$0] is aligned with Al_2O_3 [10$\bar{1}$0] on Al_2O_3 (0001) substrates and WSe_2 [10$\bar{1}$0] is aligned with graphene [10$\bar{1}$0] on monolayer graphene (MLG)/SiC (0001) substrates. Epitaxial strain of the ML WSe_2 films on different substrates are uncovered. The in-plane lattice parameter is estimated to be 3.2721 Å on Al_2O_3 (001) and 3.2768 Å on MLG/SiC (001) corresponding to compressive strain of 0.3% and 0.16% with respect to the bulk lattice constant of WSe_2, respectively

Electronic structure has been investigated by angle resolved photoelectron spectroscopy (ARPES) using monolayer WSe_2 grown on conducting MLG on SiC substrate. We revealed electronic bands with high quality, from which we evaluated the spin splitting of the valance bands at the **K**-point in the Brillouin zone. The spin splitting (Δ_{so}) is measured to be 0.465 eV. Furthermore, we uncovered a charge transfer between the graphene substrate and the ML WSe_2. The effect of the strain on the Δ_{so} was thoroughly examined using first principles calculations.

Stoichiometric WSe_2 is semiconducting and insulating ($\gg$MΩ) below room temperature. To study the transport of strongly spin-orbit coupled valance bands of WSe_2, we performed Nb doping of WSe_2 which is expected to hole-dope the system. By using an alloy target (W-Nb), we succeeded in creating conducting WSe_2 films and measuring the resistance down to 2 K. The carrier density evaluated by the Hall Effect matched well with a nominal Nb concentration of the alloy target. Temperature dependence of resistivity indicated variable-range hopping [8]. Low temperature angle-dependent magnetoresistance clearly showed the sign of quantum interference effects (weak anti-localization and weak localisation) which are sensitive to the direction of the applied magnetic field with respect to the current. Using the Hikami-Larkin-Nagaoka (HLN) theory [9,10], we estimated the phase and spin coherence lengths. Coherence lengths are in the range of tens

of nanometres at low temperatures. From the preliminary data analysis, Dyakonov-Perel mechanism seems to be responsible for the spin relaxation at low temperatures in our heavily p-doped WSe$_2$ thin films.

As outlined above, epitaxial films created by h-PLD enabled (i) collection of quantitative structural data by a diffraction technique, (ii) revealing electronic band structure by ARPES, and (iii) control of conductivity in WSe$_2$ by hole doping. Thus, we not only provide an experimental platform to study spin-orbit coupling effects in monolayer WSe$_2$ with flexible design possibilities, but also provide quantitative structural and electronic information that is essential for constructing quantitative theory.

Zusammenfassung

Die Physik der kondensierten Materie ist einer der fundamentalen Zweige der Physik. Sie befasst sich mit der Untersuchung der Eigenschaften von Materie. Wir sind von verschiedenen Arten von Materialien umgeben. Um diese in vollem Umfang nutzen zu können, müssen wir ihre Eigenschaften kennen und verstehen. Unter der Fülle verschiedener Arten von Materialien beeinflussten keine den Fortschritt des Menschen so wie die Halbleitermaterialien wie Silizium, weshalb inoffiziell auch vom *Silizium*-Zeitalter gesprochen wird [11,12].
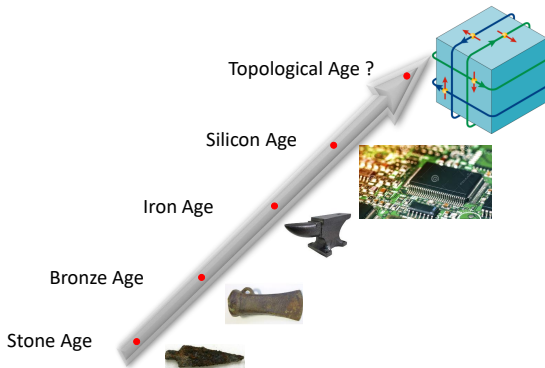

Abbildung 1: Verschiedene Stadien der Menschheitsgeschichte zusammen mit den repräsentativen Materialien ihrer Zeit.

Halbleitermaterialien weisen eine elektronische Leitfähigkeit auf, die zwischen der von reinen Metallen und Isolatoren liegt. Es gibt zwei Möglichkeiten, die Leitfähigkeit in einem Halbleiter zu ändern: Dotierung und elektrisches Feld (Gate). Im Vergleich zur Dotierung ermöglicht das Gating eine flexible Manipulation der Leitfähigkeit. Auf diese Weise kann der Ladungsfluss zwischen Source und Drain über ein externes Feld gesteuert werden. Die Zustände der Leitfähigkeit (*on*) und der Nichtleitfähigkeit (*off*) der Ladung sind die binäre Basis einer Transistor-basierten Computerarchitektur.

Die Erfindung des Transistors hat die Elektronikindustrie radikal verändert. Mit der Verbesserung der Synthese von hochwertigem Silizium stieg die Leistungsfähigkeit elektronischer Geräte drastisch an. Elektronik auf Siliziumbasis stößt jedoch an seine Grenzen. Das Moore'sche Gesetz besagt, dass sich die Dichte der Komponenten auf integrierten Schaltkreisen in regelmäßigen Abständen verdoppelt. In der Vergangenheit wurde eine Verdoppelung alle zwei Jahre beobachtet [13, 14]. Gleichzeitig schrumpft die Größe der Transistoren ständig. Mit abnehmender Größe wird der Quantentunneleffekt zum Problem bei der Manipulation der Ladung. Solche Tunnelprozesse ermöglichen einen Ladungsfluss, selbst wenn sich der Transistor im *off*-Zustand befindet. Darüber hinaus verursacht die hohe Dichte an Bauteilen Probleme beim Wärmemanagement [15]. Daher müssen wir über die Grenzen einer auf Ladungszuständen basierenden Elektronik hinausblicken.

Wir befinden uns in einer Übergangsphase des elektronischen Zeitalters. Nachdem die Manipulation der elektronischen Ladung sicher beherrscht wird, bestehen die Bemühungen weltweit darin, den Spin-Freiheitsgrad des Elektrons zu nutzen, um effiziente Elektronik-Bauelemente zu fertigen [16–21]. Im Gegensatz zu elektronischem Speicher steckt Nutzung des Spins in Logikbausteinen noch in den Kinderschuhen, obwohl vor einigen Jahrzehnten schon ein viel beachtetes theoretisches Konzept veröffentlicht wurde [22].

In diesem Zusammenhang kommen die Materialwissenschaf-

ten ins Spiel, und zwar in zweifacher Hinsicht. Auf der einen Seite bei der Nutzung bekannter elektronischer Zustände für innovative Anwendungen, und auf der anderen Seite bei der Entdeckung und dem Verstehen neuer Eigenschaften. Bei der Entwicklung von hocheffizienten Bauteile der nächsten Generation eröffnen niederdimensionale Materialien eine neue Perspektive.

Die Entdeckung von Graphen ist wohl eine der spektakulärsten im Bereich der Festkörperph-ysik [1, 2]. Obwohl Graphen viele ungewöhnliche strukturelle und elektronische Eigenschaften besitzt, ist seine Anwendung in elektronischen Bauteilen aufgrund der fehlenden Bandlücke begrenzt. Mit Blick auf den Einsatz in funktionalen elektronischen Bauteilen wird daher nach niedrigdimensionalen Systemen mit einer Bandlücke ungleich Null geforscht [3]. In dieser Hinsicht zählen Übergangsmetalldichalkogenide (TMDCs) zu den vielversprechendsten Kandidaten. Zusätzlich zu einer endlichen Bandlücke machen das Fehlen von Inversionssymmetrie und die starke Spin-Bahn-Kopplung (SOC) TMDCs zu einem interessanten Materialsystem, das es zu untersuchen gilt [4–6].

Um die Eigenschaften von TMDCs zu verstehen, sind zuverlässige Synthesemethoden und die Möglichkeit ihre strukturellen und elektronischen Eigenschaften zu manipulieren unerlässlich. Zur Synthese von Dünnfilmen stehen viele Methoden zur Verfügung, z. B. Abblätterung (Exfoliierung), chemische Gasphasenabscheidung (CVD) und Molekularstrahlepitaxie (MBE). Obwohl den mit diesen Methoden gezüchteten Dünnfilmen, einschließlich einlagiger Schichten, einige wünschenswerte Eigenschaften fehlen, wird ihre Erforschung unvermindert fortgesetzt. Unter den TMDCs erregte einlagiges (ML) WSe_2 aufgrund seiner großen Spinaufspaltung im Valenzband infolge der zuvor erwähnten starken SOC und der gebrochenen Inversionssymmetrie beträchtliche Aufmerksamkeit. Die angegebenen experimentellen Werte der Spinaufspaltung aus ARPES-Untersuchungen sind jedoch über einen weiten Wertebereich gestreut. Es wird vermutet, dass die Variation der Messergebnisse durch Dehnung der einlagigen Proben verursacht

wird [7]. Jedoch sind derzeit keine genauen Daten zum Dehnungs-verhalten, speziell aus Untersuchungen mit Beugungsmethoden, verfügbar. Auch gibt es nur wenige Arbeiten, die die Spinphy-sik anhand von Transporteigenschaften beleuchten, insbesonde-re für atomar dünne WSe_2-Schichten. In der bekannten Lite-ratur wird über die Modulation die Ladungsträgerdichte unter Verwendung von elektrostatischen Gattern berichtet. Dies führt zu einer weiteren symmetriebrechenden Komponente in die be-reits bezüglich der Inversion asymmetrischen Monolage. Ein Spin-Momentum-Locking-Effekt könnte die Komplexität erhöhen, eine Wirbel-Spintextur (konventioneller Rashba-Typ) könnte mit dem ursprünglichen Ising-Typ mischen [23–25].
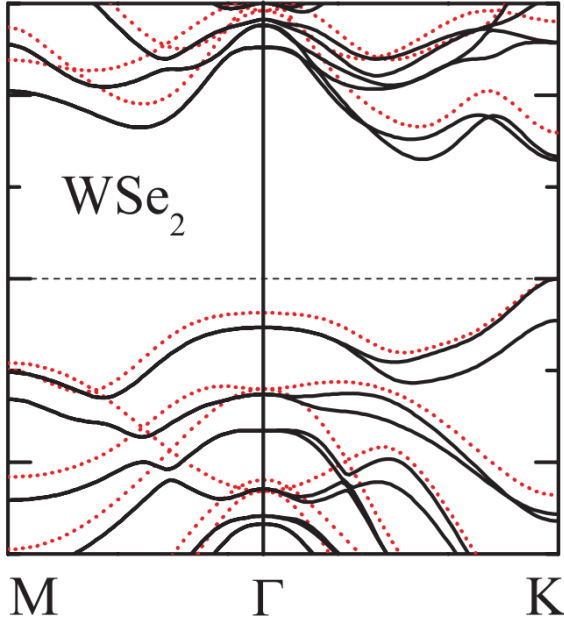

Abbildung 2: Die elektronische Bandstruktur von ML WSe_2 aus Dichtefunktional-Rechnungen mit SOC (durchgehend) und ohne SOC (gepunktet), aus Ref. [26].

Das Ziel der vorliegenden Arbeit ist die Synthese ultra-dünner,

epitaktisch gewachsener Wolframdiselenid (WSe$_2$) Dünnfilme bis hin zu einer Monolage (ML) mittels modifizierter gepulster Laserabscheidung (engl.: *hybrid*-pulsed laser deposition, *h*-PLD), um die strukturellen und elektronischen Eigenschaften sehr genau zu untersuchen. Wir vergleichen unsere Daten mit den Ergebnissen von Dichtefunktional-Berechnungen der elektronischen Bandstruktur um einen experimentellen Referenzspunkt für die Abhängigkeit der Spinaufspaltung von der Dehnung der Schicht zu erhalten. Weiterhin werden lochdotiere WSe$_2$-Dünnfilme synthetisiert, um die Spineigenschaften der Ladungsträger im Valenzband zu untersuchen. Damit wollen wir einige der Fragen zu den Eigenschaften dünner Filme von WSe$_2$ einschließlich einlagiger Proben beantworten, die in bisherigen Untersuchungen noch offen blieben.

In dieser Arbeit haben wir die Eignung der *h*-PLD-Methode für die Synthese qualitativ hochwertiger WSe$_2$-Dünnfilmen bis hin zu einlagigen Proben nachgewiesen. Die Einschränkungen, die andere Methoden bei der Synthese von ML WSe$_2$ aufweisen, konnten überwunden werden. *h*-PLD kann auch für das Wachstum anderer TMCDs angewandt werden. Der große Vorteil unserer Methode ist ein aufbauendes (bottom up) Vorgehen im Ultrahochvakuum mit der zusätzlichen Möglichkeit, die Proben mit verschiedenen Elementen dotieren zu können. Das bottom-up-Vorgehen führt zu einem Einrasten der kristallografischen Achsen in makroskopischer Ausdehnung (10×10 mm^2). Ein solche Eigenschaft ermöglicht die Durchführung hochgenauer Beugungsexperimente, die bei mechanisch abgeblätterten Proben nicht möglich sind. Darüber hinaus wird durch die Ultrahochvakuum-Bedingungen in der Wachstumskammer eine Verunreinigung der Probe verhindert, ein entscheidender Vorteil bei der Durchführung von oberflächenspezifischen Experimenten wie ARPES. Die Verschiebung des Fermi-Niveaus gelang auf zuverlässige Weise durch die Dotierung mit verschiedenen Elementen. Schließlich konnten wir das Wachstum einer Van-der-Waals-Heterostruktur von ML WSe$_2$ auf Graphen nachweisen.
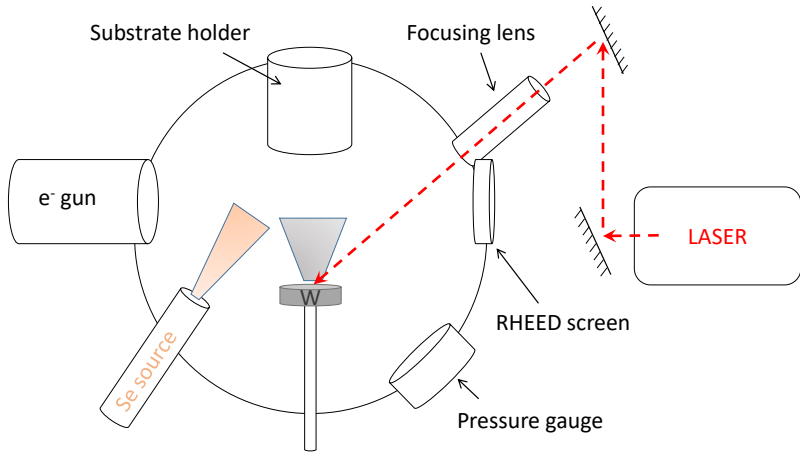
Abbildung 3: Schematische Darstellung des *Hybrid*-Systems zur gepulsten Laserabscheidung (*h*-PLD) und dessen Hauptkomponenten.

Mehrere experimentelle Techniken wurden angewandt, um die einlagige Struktur von ML WSe_2 zu bestätigen. Mit der in-situ Beugung hochenergetischer Elektronen bei Reflexion (engl.: reflection high-energy electron diffraction, RHEED) kann ML WSe_2 identifiziert werden durch das Auftauchen von Beugungslinien im zweidimensionalen (2D) Grenzfall, welche die dreidimensionalen (3D) Bragg-Punkte des Bulk-Substrats ersetzen. In Raman-Streuexperimenten unterscheidet sich ML WSe_2 von zweilagigen und dickeren WSe_2-Filmen durch das Fehlen der Anregung bei $310 \, \mathrm{cm}^{-1}$. Diese Techniken werden in der TDMC-Forschung weitgehend genutzt, um ML WSe_2 nach Abblätterung von dickeren Flocken zu unterscheiden. Zur Abbildung der Oberflächenmorphologie und zur Identifikation von WSe_2-Inseln auf verschiedenen Substraten wurde die Rasterkraftmikroskopie (AFM) eingesetzt.

Die in der *h*-PLD gewachsenen Dünnfilme ermöglichten die genaue Bestimmung von Strukturdaten von mehr- und einlagi-

gen Schichten. Besonders durch das Einrasten der kristallografischen Achsen konnten hochpräzise Beugungsexperimente mit Synchrotron-Strahlung durchgeführt werden und die epitaktische Beziehung zwischen ML WSe$_2$ und verschiedenen Substraten sowie die epitaktische Verspannung der Schichten aufgedeckt werden.
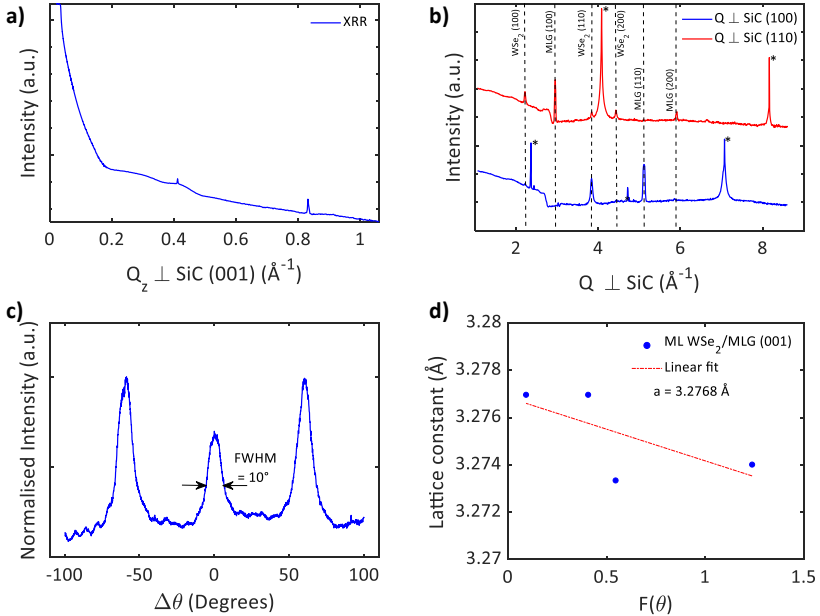

Abbildung 4: a) XRR von ML WSe$_2$ auf einem Substrat von MLG (001) auf SiC (001). b) GIXRD für zwei senkrechte Richtungen des Substrats SiC. c) Rocking-Scan des (110)-Peaks von WSe$_2$. d) Streudiagramm mit linearer Anpassung zur Abschätzung des in-plane Gitterparameters.

Sowohl Röntgenbeugung mit Synchrotron-Strahlung (XRD) als auch Röntgenbeugung mit streifendem Einfall (engl: Grazing incidence X-ray diffraction, GIXRD) wurden zur Bestimmung der Kristallstruktur von ML WSe$_2$ eingesetzt. Zwischen ML WSe$_2$ und den Substraten wurden die folgenden Orientierungs-Beziehungen

festgestellt. Auf Al_2O_3 (0001) Substrat ist WSe_2 [10$\bar{1}$0] mit Al_2O_3 [10$\bar{1}$0] gleichgerichtet. Auf einem Substrat von einer Lage Graphen auf SiC, (MLG)/SiC (0001) ist WSe_2 [10$\bar{1}$0] mit Graphen [10$\bar{1}$0] gleichgerichtet. Der in der Ebene liegende Gitterparameter von ML WSe_2 wurde auf Al_2O_3 (001) zu 3,272 Å und auf MLG/SiC (001) zu 3,277 Å bestimmt. Dies entspricht einer Druckverformung von 0,3 % beziehungsweise 0,16 % im Vergleich zu Bulk WSe_2.
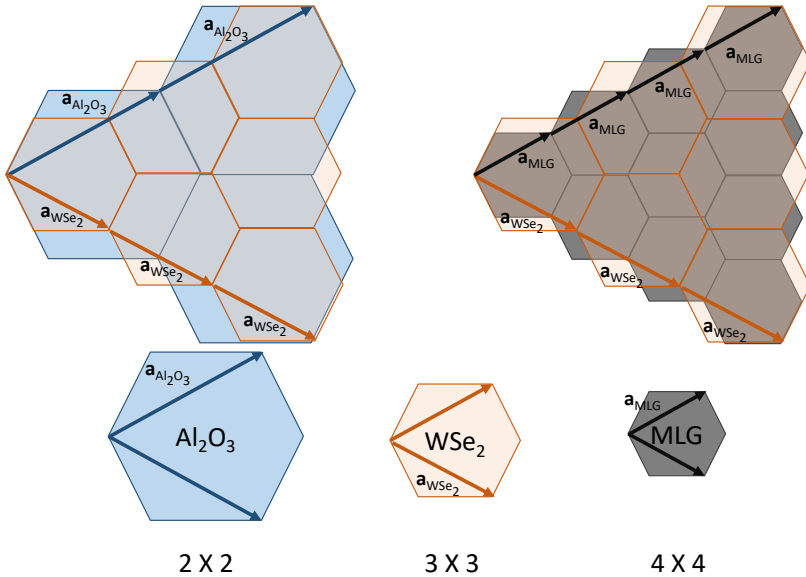
Abbildung 5: Gitterbeziehung von ML WSe_2 auf Al_2O_3 (001) und auf MLG.

Unter Ausnutzung der eingerasteten kristallografischen Achsen konnte die Spinaufspaltung des Valenzbandes am **K**-Punkt mit ARPES eindeutig gemessen werden, so wie theoretisch vorhergesagt. Der Wert für die Spinaufspaltung in ML WSe_2 (Δ_{so}) beträgt 0,465 eV. In Übereinstimmung mit den Kristallstrukturen aus Beugungsexperimenten deutet dieser Wert auf ein Fehlen von Inversionssymmetrie hin. Die Abhängigkeit von Δ_{SO} von der Ver-

spannung wurde mit der Dichtefunktionalmethode theoretisch bestimmt. Aus der Kombination der experimentellen Beugungs- und ARPES-Daten mit den berechneten Daten kann ein Phasendiagramm bezüglich Verspannung und Spinaufspaltung erstellt werden, welches in Zukunft bei der Optimierung opto-elektronischer Eigenschaften von Nutzen sein wird. Die ARPES-Messungen zeigten auch einen Ladungstransfer zwischen MLG und ML WSe_2, welcher zu n-dotiertem ML WSe_2 führte. Diese Erkenntnis ist für die Einstellung des Fermi-Niveaus in Abhängigkeit vom Ladungstransfer in Van-der-Waals-Heterostrukturen von Bedeutung, so wie beispielsweise in Heterostrukturen von ML WSe_2 und supraleitendem $NbSe_2$, wo unter Ausnutzung des Proximity-Effekts exotische Paarungsmechanismen erwartet werden.
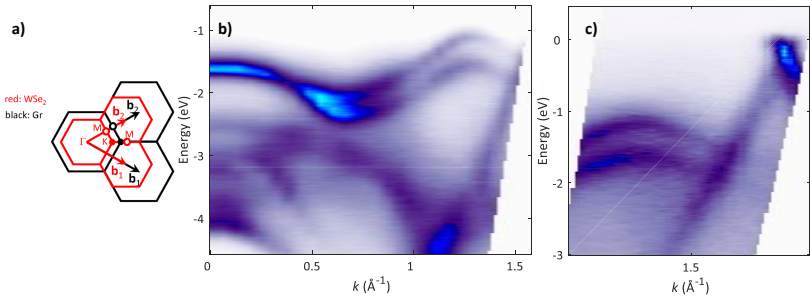

Abbildung 6: a) ML WSe_2 und Graphen, überlagert im reziproken Raum. b) ARPES-Daten von ML WSe_2, gemessen entlang der Richtung **Γ**-**K**, zeigen deutlich die Spinaufspaltung des Valenzbands. c) ARPES-Daten zeigen den Dirac-Punkt von Graphen und Teile des Valenzbands von ML WSe_2.

Stöchiometrisch zusammengesetztes WSe_2 ist unterhalb der Raumtemperatur ein Isolator ($\gg$ MΩ). Um die Transporteigenschaften im Zusammenhang mit den stark Spin-Bahn-gekoppelten Valenzbändern in WSe_2 zu untersuche, wurden das System mit Niob dotiert, um lochdotierte Schichten zu erzeugen. Durch Verwendung eines W-Nb-Legierungstargets gelang es uns, leitende WSe_2-Schichten zu erzeugen und deren Widerstand bis zu Tem-

peraturen von 2 K zu messen. Die über den Hall-Effekt bestimm-
te Ladungsträgerdichte ist in Einklang mit der nominalen Nb-
Konzentration des Legierungstargets. Die Temperatur-Abhängigkeit
des Widerstands wiest auf einen variable-range hopping Mecha-
nismus hin [8]. Der winkelabhängige Magnetowiderstand bei tiefer
Temperatur zeigt deutliche Anzeichen von Quanteninterferenzef-
fekten (schwache Antilokalisierung und schwache Lokalisierung),
die von der Richtung des angelegten Magnetfelds in Bezug auf
die Stromrichtung abhängen. Phasen- und Spin-Kohärenzlängen
wurden mit Hilfe der Hikami-Larkin-Nagaoka-Theorie (HLN) ab-
geschätzt [9, 10]. Die Kohärenzlä-ngen liegen bei niedrigen Tem-
peraturen im Bereich von einigen zehn Nanometern. Nach einer
vorläufigen Analyse der Daten scheint in den stark p-dotierten
WSe_2-Dünnfilmen der Dyakonov-Perel-Mechanismus [27, 28] für
die Spinrelaxation bei tiefen Temperaturen verantwortlich zu sein.

Mit diesen Versuchen wird gezeigt, dass die Beeinflussung des
Fermi-Niveaus durch chemische Dotierung mit Nb möglich ist,
und dass ein Isolator-Metall-Übergang erzeugt werden kann. Dies
ist ein bedeutender Schritt hin zu wirksam dotieren TMDCs, die
eine Untersuchung der Spineigenschaften in Abhängigkeit vom
Fermi-Niveau ermöglichen, ohne dass wie z.B. beim Gating durch
Anlegen eines elektrischen Feldes zusätzliche symmetriebrechende
Komponenten eingeführt werden. Eine anisotrope Magnetleitfä-
higkeit in Abhängigkeit von der Richtung des Magnetfelds konnte
nachgewiesen werden. Bei senkrecht zum Strom angelegtem ma-
gnetischem Feld erwies sich die Spindephasierungszeit als lang
verglichen mit der Phasenkohärenzzeit. Diese Eigenschaft könnte
für Spintronic-Anwendungen interessant werden, bei denen Spin-
ströme stabil gegenüber Streueffekten sein müssen auf einer Län-
genskala die dem Abstand der Elektroden entspricht. Bei parallel
zum Strom angelegtem magnetischem Feld ist die Spindephasie-
rungslänge allerdings deutlich kürzer. Solche feldrichtungsabhän-
gigen Magnetotransport-Eigenschaften wurden zum ersten Mal
in dotiertem WSe_2 beobachtet. Die Ursachen müssen in Zukunft
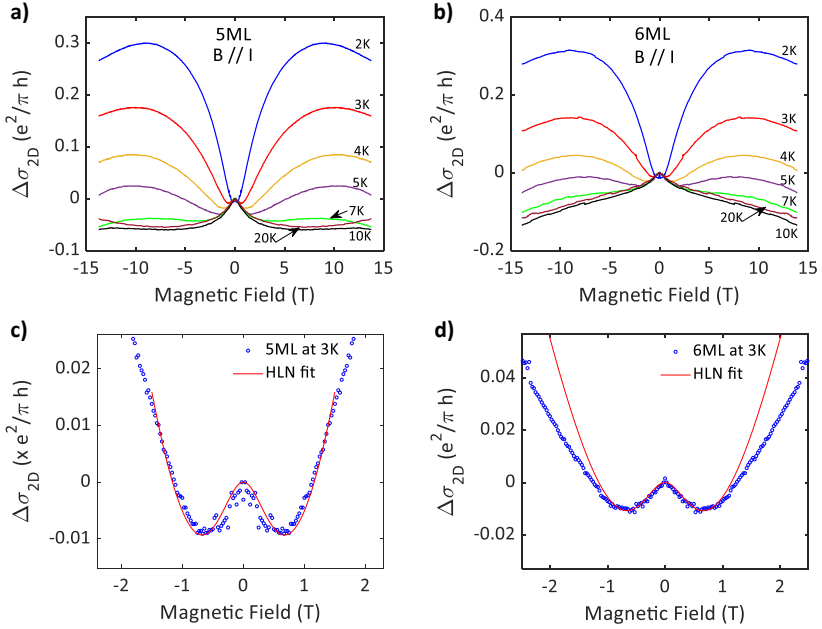noch genauer untersucht werden.

Abbildung 7: a) Leitfägigkeit von 5ML $Nb_{0.1}W_{0.9}Se_2$ gewachsen auf Al_2O_3 (001) Substrat im Magnetfeld parallel zur Stromrichtung. b) dto. von 6ML $Nb_{0.1}W_{0.9}Se_2$. c) Magnetleitfähigkeit bei 3 K von 5ML $Nb_{0.1}W_{0.9}Se_2$ und HLN-Anpassung. d) dto. von 6ML $Nb_{0.1}W_{0.9}Se_2$.

Zusammenfassend gesagt, erweitert der neue Syntheseweg den Zugang zur Physik und zu Anwendungen von TMDCs. Drei wesentliche Ergebnisse sind in dieser Arbeit dokumentiert. (1) Dünnfilme von WSe_2 konnten durch ein bottom-up Vorgehen mit h-PLD bis hin zu einlagigen Schichten synthetisiert werden. Umfangreiche Untersuchungen der strukturellen (XRD/GIXRD) und elektronischen Eigenschaften (ARPES) von ML WSe_2 wären mit abgeblätterten Proben nicht möglich gewesen. Im Gegensatz zu epitaktisch gewachsenen Schichten ist die Orientierung von abgeblätterten Dünnfilmen willkürlich und die begrenzte Größe der Proben erschwert sehr die Anwendung von GIXRD, da der Strahl

bei der Anordnung des streifenden Einfalls sich über 10 mm erstreckt. Der epitaktische Aufbau bietet auch einen Bezugsrahmen zur Anordnung der Proben in hochgenauen Messungen mit Synchrotron-Strahlung. (2) Mittels GIXRD und ARPES konnten strukturelle und elektronische Eigenschaften sehr genau gemessen werden. Die experimentellen Ergebnisse wurden Daten aus Dichtefunktional-Bandstruktur-Rechnungen gegenübergestellt, wobei der Einfluss der epitaktischen Verspannung berücksichtigt wurde. Damit konnten wir den sehr geringen Einfluss der Verspannung auf die Spinaufspaltung in unseren epitaktisch gewachsenen WSe$_2$-Schichten herausarbeiten. Die Ergebnisse stellen den ersten hochgenauen experimentellen Bezugswert für die Spinaufspaltung unter Verspannung dar. (3) Mit der h-PLD steht eine wirksame Methode zur Verfügung, um das Fermi-Niveau durch Dotierung in die gewünschte Position zu verschieben. In WSe$_2$-Schichten mit einer Dicke von wenigen Atomlagen wurde durch Dotierung ein Übergang vom Isolator zum Metall herbeigeführt. Chemische Dotierung hat aus zweierlei Gründen Vorteile gegenüber dem Gating. Erstens wird der Symmetriebruch, der für einlagige Proben charakteristisch ist, nicht durch Effekte eines angelegten elektrischen Feldes überlagert. Zweitens verhindert die Gatterelektrode eine experimentelle Untersuchung von ML WSe$_2$ mittels STM/STS, womit in Zukunft neuartige Paarungsmechanismen der Supraleitung untersucht werden sollen. Der in dieser Arbeit aufgezeigte Syntheseweg und die Dotierungsmöglichkeiten öffnen eine Tür zur Erzeugung künstlicher Heterostrukturen in eine Weise die bestens geeignet ist, die Physik von Van-der-Waals-Grenzflächen zu untersuchen. german

1. Introduction

1.1 Background

Condensed matter physics is one of the fundamental branches of physics. It deals with the study of properties of matter. We are surrounded by different types of materials. To utilize various types materials to their fullest requires us to know and understand their properties. Due to the significance of materials, the human history is classified based on the material of technology of the age. Which is the *Three Age System* for the *stone*, the *bronze*, and the *iron* ages [29, 30].

We have come a long way from the classification of matter into classical elements of air, earth, water, fire and aether [31] to a modern classifications based on their physical, mechanical, chemical, magnetic and electronic properties. Just as the classical physical states of matter, solid, liquid, and gaseous is updated with plasma [32], superconductivity (SC) [33–35], superfluidity [36], Bose-Einstein condensate (BEC) [37, 38] etc.; the electronic states of conductor, semiconductor and insulator is updated with topological insulators (TI) [39], Dirac and Weyl metals and semimetals [40–44] etc. Among the plethora of different kinds of materials, none influenced the human progress like the semiconducting materials such as silicon. Therefore, our present

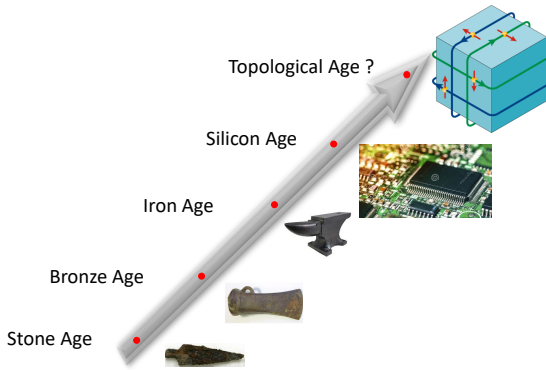era is unofficially known as the *silicon* age [11,12].

Figure 1.1: Different stages of human history along with the representative material of the age.

Semiconducting materials have the electronic conductivity somewhere between that of pure metals and insulators. The electronic conductivity of the semiconductor can be altered in two possible ways. First by adding impurities, a process known as *doping* and second, by creating an electric field in a process known as *gating*. Compared to doping, gating allows flexibility in the manipulation of the conductivity. This allows us to control the flow of charge between the source and the drain using an external field. The states of conductivity (*on*) and non-conductivity (*off*) of the charge enabled the binary basis for the computer architecture with the use of transistors.

The invention of transistor radically changed the electronic industry. With subsequent refinement in the synthesis of high quality silicon, the efficiency of the electronic devices increased drastically. However, the state-of-the-art silicon based transistor is facing a few challenges. The Moore's law states that the density of components on the integrated chip doubles at a regular interval. Original prediction was doubling every two years [13, 14]. Consequently, the size of the transistors keeps shrinking down.

As the size goes down, the quantum tunnelling effect becomes a problem in the manipulation of the charge. Such tunnelling processes allows the charge to flow even when the transistor is in the *off* state. In addition, the high density of components creates problem in the heat management [15]. Hence, we need to look beyond the charge based electronic devices.

We are in the transition period of the electronic age. After mastering the manipulation of the electronic charge, global effort is to incorporate and utilize the spin degree of freedom of the electron to realize efficient devices [16–21]. In such devices, it is the spin that carries the information and can be manipulated with external fields. Earliest report of the spin dependent transport in a heterostructure is the tunnelling between the ferromagnetic films [45]. With the discovery of giant magnetoresistance in a heterostructure with ferromagnetic materials [46, 47], the efficiency of data storage has increased tremendously [21] due to miniaturization of the reader head. As of now, memory devices which work on both tunnelling and giant magnetoresistance phenomena are available in the market. Compared to the application towards memory devices, utilizing spin for a logic device is still in its infancy despite the influential theoretical proposal that has been made a few decades ago [22].

In the forefront of such an endeavour is the field of material science. Efforts are being made to utilise the current known electronic states for innovative applications in parallel to discovering and understanding newer properties. With an emphasis on miniaturisation and higher efficiency of the next generation devices, low dimensional materials offer a new perspective. Even though the physio-chemical properties of graphene are extremely robust to ambient conditions with excellent electro-elastic properties among the 2D materials, it is less likely to be implemented in functional electronics. The drawback of graphene which limits its use in modern electronic devices is the lack of a band gap.

The search is on for other low dimensional electronic systems. Among them, transition metal dichalcogenides (TMDCs)
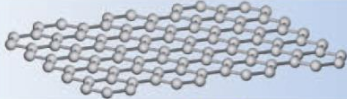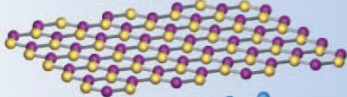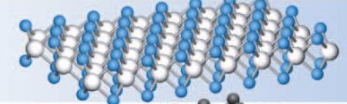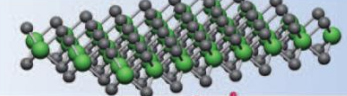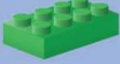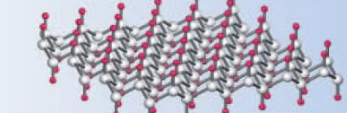
Figure 1.2: Some of the 2D materials that could be used alone or in combination with each other like Lego, creating van der Waals heterostructures [3].

are stepping up to fill this gap left by graphene with their non-zero band gap [48]. Although the single layer MoS_2 is obtained in 1986 [49], not much work has been done in the field of low dimensional systems. It is only after the successful synthesis of a free standing graphene in 2004 [50] that the global research efforts are refocused on two dimensional (2D) materials [51].

Study of low dimensional TMDCs could have double benefits of addressing the device applications as well as creating a platform for the investigation of novel physical phenomena. For this reason, we are motivated to synthesise and investigate one of the TMDCs, ML WSe_2. The following part of this chapter provides an overview of the TMDCs and the motivation to select ML WSe_2 as a material of interest for this thesis work.

1.2 Transition metal dichalcogenides

1.2.1 Introduction

2D materials are crystalline materials consisting of a single layer of atoms as in the case of graphene, phosphorene and silicene etc. or of multiple layer units as in the case of TMDCs [3, 5, 52, 53]. These systems are generally called the *van der Waals* materials [3,4,54]. Signature of a van der Waals material is a strong covalent bonding within the layer and a weak van der Waals interaction between the layers. This allows for thinning down bulk material to the 2D limit.

Figure 1.3: Periodic table with transition metals and chalcogenides highlighted [55].

Transition metal dichalcogenides (TMDCs) are one of the earliest materials to form on earth with MoS_2 samples dating back to 2.9 billion years [56,57]. The physical properties of bulk TMDCs were extensively studied in the 20th century [58,59]. TMDCs are well known for their tribological properties [60,61] and they have been investigated as dry lubricants [62,63]. These materials have been identified to have wide range of mechanical, chemical and

electronic applications as well as novel systems harbouring exotic physical phenomena [3–6, 15, 48, 52, 55, 64–82].

Different TMDC compounds are available with various stoichiometries and crystal structures. Even though some of the TMDCs share a similar crystal structure, they exhibit wide ranging electronic properties such as semiconducting, insulating and even superconducting [6, 15, 48, 52, 66, 68, 72, 77, 80, 82]. In order to fully appreciate the significance of the monolayer TMDCs, we start with the bulk properties and proceed to those of monolayer.

1.2.2 Bulk TMDC

Crystal structure

TMDCs are van der Waals materials. In them, the transition metal layer is sandwiched between the chalcogen layers forming a unit layer with strong covalent bonding within and different unit layers held together with van der Waals forces. TMDCs can be found in various polymorphs labelled such as 1T, 2H, and 3R etc. The letter signify the type of symmetry (here T:trigonal, H:hexagonal & R:rhombohedral) and the number indicates the number of layers in a unit cell. In the 1T phase, the chalcogen atoms surround the transition metal atom forming an octahedral. 2H phase consists of two unit layers in which the chalcogen atoms forms a prism around the transition metal. There exists a center of inversion in both of these types. In the case of 2H-MX_2, there are two unit layers such that the transition metal in the upper layer is placed above the chalcogen atoms in the bottom layer. Therefore, the bulk 2H-MX_2 shows symmetry space group of $P6_3/mmc$ (space group no. 194).

The layered nature of TMDCs gives rise to anisotropic structural and electronic properties. Among TMDCs, the bonding is between the transition metal and the chalcogen atoms through four electrons of metal to fill the bonding states. The charges on the transition metal and the chalcogen atoms are +4 and -2, respectively. The lack of dangling bonds makes the surface
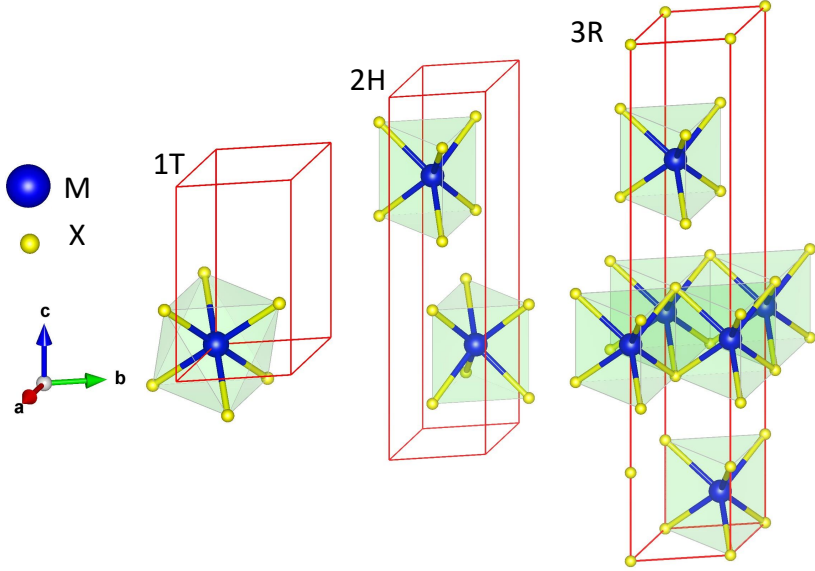
Figure 1.4: Three major polymorphs, 1T, 2H, and 3R of transition metal dichalcogenides MX_2 [59,83,84].

cleavable, stable, and less reactive.

Electronic band structure

In an *octahedral* coordination for the 1T type polymorph, the d-orbitals are split due to the crystal field into two groups, e_g (d_{z^2} and $d_{x^2-y^2}$) and t_{2g} (d_{xy}, d_{yz} and d_{xz}). In the case of a *trigonal prismatic* coordination of 2H polymorph, the d-orbitals are split into 3 groups, a_1 (d_{z^2}), e ($d_{x^2-y^2}+d_{xy}$) and e' ($d_{yz}+d_{xz}$). Depending on the transition metal atom involved, different orders of filling of the electronic bands are possible. By going from lower group to the higher the number of electrons from the transition metal atoms increase, thereby filling the higher orbitals.

Schematic figure of the density of states at the $\mathbf{\Gamma}$-point and the filling for various transition metals from different groups in the
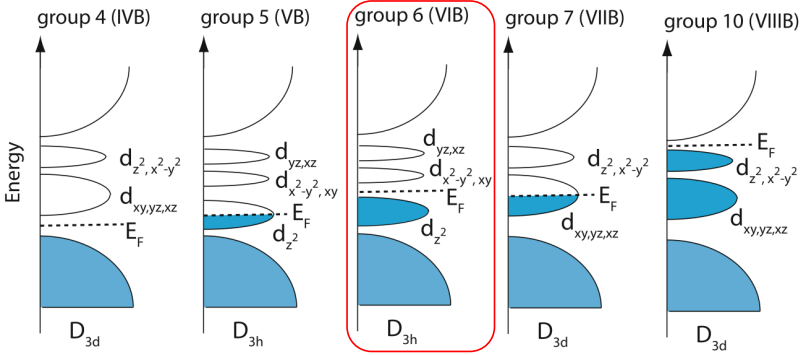
Figure 1.5: DOS at the Γ of TMDCs for different transition metal groups in the periodic table and crystal symmetry showing the difference between the octahedral and trigonal prismatic (of MX_2 {M: Mo, W; X: S, Se} highlighted in red box) coordinations. Schematics reproduced from Ref. [56].

periodic table along with the crystal symmetry is shown in the Fig.1.5. Depending on the geometry, the type of orbital splitting due to the crystal field and the character of the orbitals change as indicated in the Fig.1.5.

In the case of MX_2 (M: Nb, Mo, Ta, W; X: S, Se, Te) with group 5 and 6 transition metals, the major polymorph is 2H with symmetry space group $P6_3/mmc$. Since the crystal structure is the same, the difference in the electronic properties can be understood in terms of electron filling. Possible different electronic states observed in MX_2 are summarised in the Tab.1.1. Since the group 5 elements Nb and Ta are having 1 electron in the d-orbital, the d_{z^2} is half filled and is completely filled in the case of group 6 elements of Mo and W which has 2 electrons when forming MX_2 compounds. This gives rise to metallic and semiconducting states respectively.

	S$_2$	Se$_2$	Te$_2$
Nb	Metal Superconducting CDW	Metal Superconducting CDW	Metal
Ta	Metal Superconducting CDW	Metal Superconducting CDW	Metal
Mo	Semiconducting ML: 1.8 eV Bulk: 1.2 eV	Semiconducting ML: 1.5 eV Bulk: 1.1 eV	Semiconducting ML: 1.1 eV Bulk: 1.0 eV
W	Semiconducting ML: 1.9 eV Bulk: 1.4 eV	Semiconducting ML: 1.7 eV Bulk: 1.2 eV	Semiconducting ML: 1.1 eV

Table 1.1: Different electronic states of TMDCs as published in Ref. [15].

1.2.3 Monolayer TMDC

Crystal structure

The monolayer limit of previously mentioned polymorphs consists of a single unit layer. Each unit layer consists of three atomic layers, a transition metal layer sandwiched between two chalcogen layers. The transition metal atoms form a triangular lattice and dictates the electronic properties of the monolayer TMDCs significantly.

Unlike 1T, 2H polymorph is much more interesting due to explicit *broken* inversion symmetry in the monolayer compared to the bulk. In the case of 2H polymorph, with the 2H→1H transition, the symmetry reduces from D$_{6h}$→D$_{3h}$ and the space group changes from $P6_3/mmc$ (space group no. 194) → $P\bar{6}m2$ (space group no. 187) [26]. When going from bulk to the monolayer, the unit cell gets a mirror plane symmetry within the layer and more importantly, the inversion symmetry present in the bulk is lost in the monolayer limit making it *non-centrosymmetric* material.

Here, we define the real and reciprocal space 1H-MX$_2$. The real space lattice vectors as shown as red arrows in the Fig.1.6 can be written as:

$$\mathbf{a}_1 = a\mathbf{x}; \mathbf{a}_2 = a\left(\frac{1}{2}\mathbf{x} + \frac{\sqrt{3}}{2}\mathbf{y}\right). \tag{1.1}$$
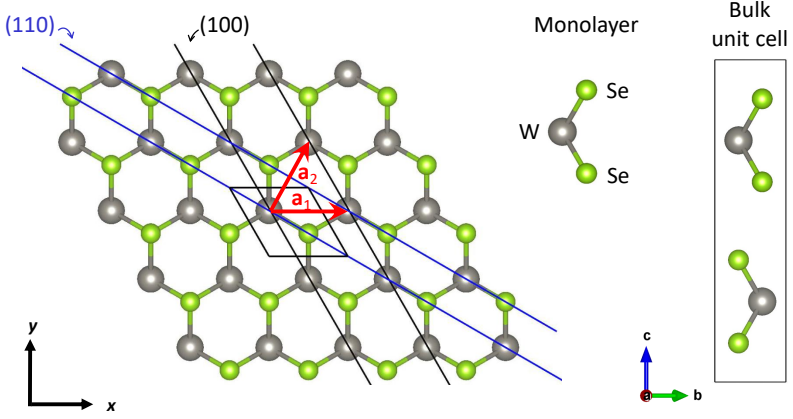
Figure 1.6: Crystal structure of MX$_2$. On the left side is the top view of the crystal structure with the unit cell indicated with a black parallelogram. Lattice planes are shown as black and blue lines for (100) and (110) lattice planes, respectively. The unit vectors are shown in red. Side view of the monolayer MX$_2$ and of the unit cell are shown on the right side.

The corresponding reciprocal lattice vectors are given by:

$$\mathbf{b}_1 = \frac{2\pi}{a}\left(\mathbf{x} - \frac{1}{\sqrt{3}}\mathbf{y}\right); \mathbf{b}_2 = \frac{2\pi}{a}\frac{2}{\sqrt{3}}\mathbf{y}. \tag{1.2}$$

This leads to a hexagonal Brillouin zone for the triangular lattice of ML MX$_2$. Centre of the Brillouin zone is the high symmetry point of $\mathbf{\Gamma}$, vertices are indicated by $\mathbf{K}$ and the midpoint
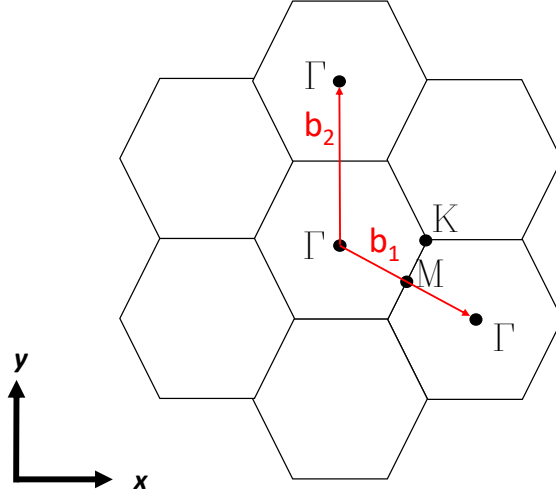
Figure 1.7: Reciprocal space of monolayer MX$_2$. High symmetry points and the reciprocal vectors are indicated on the Brillouin zone using Eqs.1.2.

of sides are denoted by **M**. These high symmetry points are important when we discuss about the electronic band structure.

Electronic band structure

The electronic band structure of monolayer TMDCs, in particular those with space group symmetry of D_{3h}, have two striking features compared to the band structure of bulk TMDCs. First, the indirect band gap in the bulk changes to direct band gap in the monolayer limit. This is related to number of W atoms in the unit cell being reduced from two to one as we go from bilayer to monolayer. It can be most easily seen at the **Γ**-point (Fig.1.8), where topmost valence bands are split for bilayers. Together with this, there is also a subtle splitting along the lowest conduction band in the **Γ–K** direction. Both of these contribute to the indirect to direct band gap transition. This can be understood basically in

terms of bonding and anti-bonding orbital formation between the atoms in two adjacent layers for bilayer case, which is absent in the monolayer.

The evolution of the band structure in 2H-MoS$_2$ calculated from the first principles is shown in the Fig.1.8. As can be observed in the Fig.1.8, the valance band maximum is at Γ and the conduction band minimum is in between the **K** and Γ which results in the indirect transitions. In the case of monolayer 1H-MoS$_2$ (which is a non-centrosymmetric and have trigonal prismatic coordination), the valance band maximum and the conduction minimum are shifted to **K** resulting in direct band gap transitions. The semiconducting state is due to the filled top most valance band with 2 electrons from the transition metal atom in a MX$_2$ compound.

The direct band gap leads to an intense photoluminescence (PL). The broad peaks in the spectra shown in Fig.1.9 corresponds to the direct excitonic transitions from the spin split valance bands to the conduction band with Δ_{so}=0.15 eV. This is very close to the value of 0.148 eV, predicted by theory in Ref. [86]. Such a transition from an indirect to a direct band gap and the resulting PL has attracted many to find opto-electronic applications [15,87–96].

Second, the lack of inversion symmetry in the monolayer limit splits the valance band into two spin polarised bands at the **K** [97]. This effect can be understood as a *Rashba* effect. When the time reversal symmetry is preserved and the space inversion symmetry is broken, the Kramer's degeneracy is lifted.

Inversion symmetry breaking and its consequence

Atomic SOC itself does not offer energy level splitting between up and down spins. However, atomic SOC together with inversion breaking in solids provide a mechanism for splitting between otherwise degenerate up and down spin states. This is in general called the Rashba effect, and is schematically shown in Fig.1.10. Although the above symmetry argument dictates that
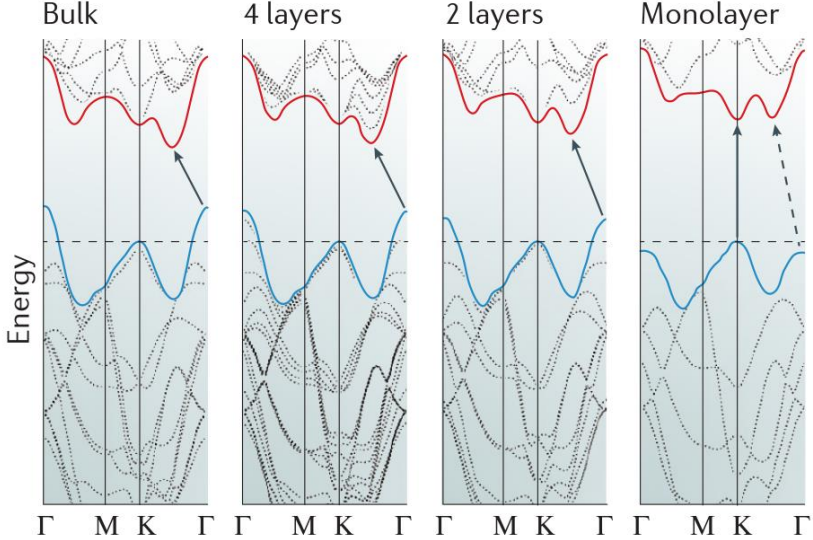
Figure 1.8: Evolution of the electronic band structure of 2H-MoS_2 calculated using first principles for different thickness as shown. The indirect transitions are indicated with arrows from the valance band to the conduction band and direct transition in the monolayer limit. Image reproduced from Ref. [75,85].

$E(k,\uparrow) \neq E(k,\downarrow)$, and thus should result in energy splitting for the up and down spins when inversion symmetry is broken, this alone does not allow us to obtain any clue on how large such effect could be in real materials. In the following, we first explain this for materials that show conventional Rashba effect (e.g. Au(111) surface) and later explain the case for monolayer WSe_2. This will enable us to clarify the uniqueness of monolayer WSe_2.

We first briefly mention SOC in atoms. In the rest frame of an electron, the nucleus orbits around it. The orbiting nucleus generates an effective magnetic field which the electron experiences. Depending on the orientation of the spin with respect to the effective magnetic moment coming from orbital motion, the energy of the electron changes. This results in the lifting of the energy
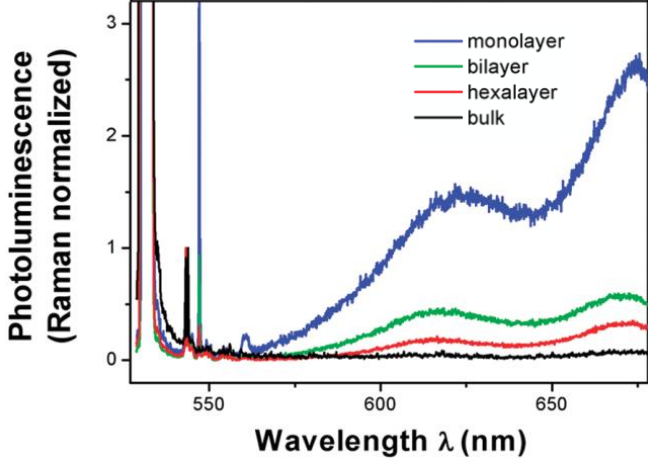
Figure 1.9: Photoluminescence spectra of 2H-MoS$_2$ with different thickness reported by Ref. [85]. PL spectra is strong in the case of ML MoS$_2$ and the two broad peaks correspond to the excitonic spectra from the spin split bands with Δ_{so}=0.15 eV.

degeneracy as a consequence of the SOC. In a non-relativistic approximation of the Dirac equation, a SOC term can be seen in the total Hamiltonian [98].

$$H_{SOC} = -\frac{\hbar}{4m_0^2c^2}\boldsymbol{\sigma}\cdot\mathbf{p}\times(\boldsymbol{\nabla}V_0). \tag{1.3}$$

The magnitude of splitting is quantified in terms of SOC constant α [$H_{SOC} = \alpha\mathbf{L}\cdot\mathbf{S}$ and $\alpha_{nl} = \frac{2}{2l+1}(\epsilon_{nlj+} - \epsilon_{nlj-})$] which is 0.005 Ry (0.068 eV) for Mo, 0.019 Ry (0.258 eV) for W, and 0.045 Ry (0.608 eV) for Au [99]. This corresponds to the energy splitting between the different total angular momentum ($\mathbf{J}$) states of the valance electrons but there are still double degeneracy coming from time reversal symmetry, thus spin up and down states are not split.

We have seen that atomic SOC does not separate two spin states in isolated atoms. Then why, after introducing inversion

14
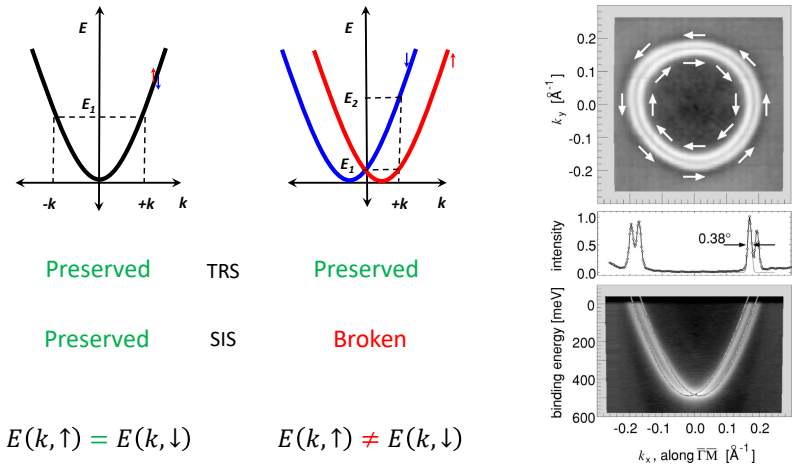
Figure 1.10: The illustration of Rashba effect with time reversal symmetry (TRS) and space inversion symmetry (SIS) indicated. On the right is the experimental evidence of Rashba spin splitting and spin texture in Au(111) as reported by [100].

breaking, is the spin degeneracy lifted in the solids? Although this can be understood in multiple theoretical schemes such as $\mathbf{k} \cdot \mathbf{p}$ perturbation theory [101] and first-principles calculation [102], in the following we use tight-binding approach [103, 104]. In a tight binding model, the electronic band structures arise due to the overlap of the neighbouring orbitals. The key to understand the Rashba spin splitting within such scheme is to consider *off-diagonal* coupling between orbitals that are allowed by reduced symmetry (i.e, by inversion breaking). We first examine an example for the spin splitting for the surface state of Au(111), which was first experimentally observed in Ref. [100] and shown in the Fig.1.10. The tight binding Hamiltonian for Au (111) is evaluated based on the model developed in the Ref. [103].

$$ H = \sum t_{ab}(\mathbf{R}_i - \mathbf{R}_j) \, |p_a(\mathbf{R}_i), \sigma\rangle \, \langle p_b(\mathbf{R}_j, \sigma| + \alpha \mathbf{L} \cdot \mathbf{S}, \quad (1.4) $$

where p_a is the orbital basis function and the overlap matrix element $t_{ab}(\mathbf{R}_i - \mathbf{R}_j)$ is given by:

$$
\begin{cases}
w\cos^2\theta_{ij} + 0.3w\sin^2\theta_{ij} & \text{for} \quad (a,b) = (x,x), \\
1.3w\cos\theta_{ij}\sin\theta_{ij} & \text{for} \quad (a,b) = (x,y) = (y,x), \\
w\sin^2\theta_{ij} - 0.3w\cos^2\theta_{ij} & \text{for} \quad (a,b) = (y,y), \\
0.1w\cos\theta_{ij} & \text{for} \quad (a,b) = (x,z) = (z,x), \\
0.1w\sin\theta_{ij} & \text{for} \quad (a,b) = (y,z) = (z,y), \\
-0.3w & \text{for} \quad (a,b) = (z,z),
\end{cases}
\tag{1.5}
$$

where, $\mathbf{R}_i$ and $\mathbf{R}_j$ are the nearest neighbours, $w = \frac{\alpha}{0.2}$ and α is the SOC constant. As highlighted in the following matrix (calculated in eV), the p_x orbitals hybridise with p_z orbitals in the absence of inversion symmetry which are otherwise orthogonal. To capture what causes spin splitting, we evaluate the tight binding Hamiltonian for Au (111) at momentum position 10% away from the $\mathbf{\Gamma}$-point in the $\mathbf{\Gamma}$-$\mathbf{K}$ direction $(\overline{k} = (\frac{4\pi}{30a}, 0))$, using the above Hamiltonian.

$$\hat{H} = \begin{array}{c|cccccc}
 & |p_x\uparrow\rangle & |p_y\uparrow\rangle & |p_z\uparrow\rangle & |p_x\downarrow\rangle & |p_y\downarrow\rangle & |p_z\downarrow\rangle \\
\hline
\langle p_x\uparrow| & 5.7699 & -\frac{\alpha}{2}i & 0.3769i & 0 & 0 & -1 \\
\langle p_y\uparrow| & \frac{\alpha}{2}i & 6.4022 & 0 & 0 & 0 & -\frac{\alpha}{2}i \\
\langle p_z\uparrow| & -0.3769i & 0 & 5.2166 & 1 & \frac{\alpha}{2}i & 0 \\
\langle p_x\downarrow| & 0 & 0 & 1 & 5.7699 & \frac{\alpha}{2}i & 0.3769i \\
\langle p_y\downarrow| & 0 & 0 & -\frac{\alpha}{2}i & -\frac{\alpha}{2}i & 6.4022 & 0 \\
\langle p_z\downarrow| & -1 & \frac{\alpha}{2}i & 0 & -0.3769i & 0 & 5.2166 \\
\end{array}$$

Au

In the absence of SOC (α=0), the tight binding matrix gives three double degenerate eigenvalues. As can be noticed in the matrix, there is an imaginary off-diagonal coupling between $p_x \uparrow$ ($\downarrow$) and $p_z \uparrow$ ($\downarrow$) (highlighted in the matrix). Usually, the p_x and p_z are orthogonal and we should not see any hybridisation between them. The reason we see such a coupling term is that the inversion symmetry is broken in the z-axis which lifts the strict orthogonality between p_x and p_z. When the SOC is introduced (α=0.608 eV), the spin degeneracy is lifted which also result in a mixing between all three orbitals. Now, we explicitly show two pairs of eigenfunctions where Rashba splitting is large (A) and small (B).

$$
\begin{aligned}
|\psi_A, +\rangle = &- 0.0431 \, |p_x, \uparrow\rangle - 0.0173i \, |p_y, \uparrow\rangle - 0.7056i \, |p_z, \uparrow\rangle \\
&+ 0.0431i \, |p_x, \downarrow\rangle - 0.0173 \, |p_y, \downarrow\rangle - 0.7056 \, |p_z, \downarrow\rangle, \\
|\psi_A, -\rangle = &+ 0.0052 \, |p_x, \uparrow\rangle - 0.0186i \, |p_y, \uparrow\rangle + 0.7068i \, |p_z, \uparrow\rangle \\
&+ 0.0052i \, |p_x, \downarrow\rangle - 0.0186 \, |p_y, \downarrow\rangle - 0.7068 \, |p_z, \downarrow\rangle, \\
|\psi_B, +\rangle = &- 0.6571 \, |p_x, \uparrow\rangle + 0.2610i \, |p_y, \uparrow\rangle + 0.0117i \, |p_z, \uparrow\rangle \\
&- 0.6571i \, |p_x, \downarrow\rangle + 0.2610 \, |p_y, \downarrow\rangle - 0.0117 \, |p_z, \downarrow\rangle, \\
|\psi_B, -\rangle = &+ 0.6473 \, |p_x, \uparrow\rangle - 0.2828i \, |p_y, \uparrow\rangle - 0.0326i \, |p_z, \uparrow\rangle \\
&- 0.6473i \, |p_x, \downarrow\rangle + 0.2828 \, |p_y, \downarrow\rangle - 0.0326 \, |p_z, \downarrow\rangle.
\end{aligned}
$$
$$(1.6)$$

We point out two prominent features in the Rashba split pair (A). First, the contribution of p_z is sizable. This is in line with our expectation that out-of-plane inversion breaking should enable the coupling of p_z with otherwise orthogonal p_x and p_y states, and thus in the Rashba split pair, p_z should be finite. Second, due to the spin direction (in-plane and pointing to y for (k_x,0)) that we analyze in the following, we expect appreciable energy difference to occur between $p_x + ip_z$ and $p_x - ip_z$ like orbitals. As we can see, not only there is a finite contribution from such orbitals in Eq.1.6 but also the coefficient of orbital for p_x differ within the pair (note that atomic SOC alone will not induce en-

ergy splitting between $p_x \uparrow + i p_z \uparrow$ and $p_x \downarrow - i p_z \downarrow$). Thus, we can capture the essential physics of the Rashba spin splitting in the tight binding model. Namely, (i) the inversion-breaking induced off-diagonal coupling (ii) which induces energy splitting in orbital angular momentum$-$like states. We note that for the Au (111) case, the magnitude of the spin splitting evaluated at the **k**-point (10% away from **Γ**) is $\sim$0.04 eV, which is less than $\sim$10% of the atomic spin orbit coupling of elemental gold (0.608 eV). This can be understood because the eigenfunction (Eq.1.6) is not exactly matching that of angular momentum states $l = +1$ and $l = -1$ states ($p_x + i p_z$ and $p_x - i p_z$: note that quantisation axis is taken along y here) $-$ not only the coefficients for p_x and p_z are mismatched, but also there is some p_y component not contributing to the spin splitting at this specific **k**-point. Thus, we can see that only a small (but finite!) component of the "*pure*" angular momentum states are contributing to the Rashba split pair, making the overall spin splitting smaller than the spin orbit coupling energy. A similar effect is observed at $-\overline{k} = (-\frac{4\pi}{30a}, 0)$, but with opposite spin polarity as shown below.

$$
\begin{aligned}
|\psi_A, -\rangle = &+ 0.0431 \,|p_x, \uparrow\rangle + 0.0173i \,|p_y, \uparrow\rangle - 0.7056i \,|p_z, \uparrow\rangle \\
&+ 0.0431i \,|p_x, \downarrow\rangle + 0.0173 \,|p_y, \downarrow\rangle + 0.7056 \,|p_z, \downarrow\rangle, \\
|\psi_A, +\rangle = &- 0.0052 \,|p_x, \uparrow\rangle + 0.0186i \,|p_y, \uparrow\rangle + 0.7068i \,|p_z, \uparrow\rangle \\
&+ 0.0052i \,|p_x, \downarrow\rangle - 0.0186 \,|p_y, \downarrow\rangle + 0.7068 \,|p_z, \downarrow\rangle, \\
|\psi_B, -\rangle = &- 0.6571 \,|p_x, \uparrow\rangle + 0.2610i \,|p_y, \uparrow\rangle - 0.0117i \,|p_z, \uparrow\rangle \\
&+ 0.6571i \,|p_x, \downarrow\rangle - 0.2610 \,|p_y, \downarrow\rangle - 0.0117 \,|p_z, \downarrow\rangle, \\
|\psi_B, +\rangle = &- 0.6473 \,|p_x, \uparrow\rangle + 0.2828i \,|p_y, \uparrow\rangle - 0.0326i \,|p_z, \uparrow\rangle \\
&- 0.6473i \,|p_x, \downarrow\rangle + 0.2828 \,|p_y, \downarrow\rangle + 0.0326 \,|p_z, \downarrow\rangle.
\end{aligned}
$$
$$(1.7)$$

Next, we explain another important consequence of the Rashba effect $-$ its *spin texture* in momentum space. With the splitting of the bands, a spin texture is created which rotates in the momentum plane. Because of two different spin types, the spins in

the two Fermi circles rotate in opposite directions.

The direction of the spin in the Fermi circle can be calculated using the spin expectation operator. For this, we need to derive the eigenfunctions at each **k**-point corresponding to the eigenvalues of the parabolic dispersion in the Fig.1.10. Around the **Γ**-point, the parabolic band structure resembles that of a free particle. Hence, we can approximate the Hamiltonian with a free particle model as:

$$H = \frac{\mathbf{p}^2}{2m} + \alpha_R(\mathbf{e}_z \times \mathbf{p}) \cdot \sigma, \qquad (1.8)$$

where, m is the mass of the electron and α_R is the empirical parameter proportional to the gradient of the electric field [103, 105]. The corresponding eigenvalues are calculated to be:

$$E = \frac{\hbar^2 k^2}{2m} \pm \alpha_R \hbar k. \qquad (1.9)$$

The spin splitting is evident from the eigenvalues shown in the Eq.1.9. The parabolic bands have a linear term added and subtracted. The corresponding eigenfunctions are:

$$\begin{aligned}
\psi_1(r) &= e^{ikr}(|\uparrow\rangle + ie^{i\theta_k} |\downarrow\rangle), \\
\psi_2(r) &= e^{ikr}(ie^{-i\theta_k} |\uparrow\rangle + |\downarrow\rangle),
\end{aligned} \qquad (1.10)$$

where, θ_k is the angle of the **k** with respect the x-axis. The spin expectation values on three directions can be calculated for the eigenfunctions shown in the Eq.1.10. The spin expectation

values are:

$$\langle s_{x1} \rangle = \frac{\hbar}{2}(ie^{i\theta_k} - ie^{-i\theta_k}), \begin{cases} 0 & \text{for } \theta_k=0 \\ -\hbar & \text{for } \theta_k=\pi/2 \end{cases}$$

$$\langle s_{y1} \rangle = \frac{\hbar}{2}(e^{i\theta_k} + e^{-i\theta_k}), \begin{cases} \hbar & \text{for } \theta_k=0 \\ 0 & \text{for } \theta_k=\pi/2 \end{cases}$$

$$\langle s_{z1} \rangle = 0,$$

(1.11)

and,

$$\langle s_{x2} \rangle = \frac{-\hbar}{2}(ie^{i\theta_k} - ie^{-i\theta_k}), \begin{cases} 0 & \text{for } \theta_k=0 \\ \hbar & \text{for } \theta_k=\pi/2 \end{cases}$$

$$\langle s_{y2} \rangle = \frac{-\hbar}{2}(e^{i\theta_k} + e^{-i\theta_k}), \begin{cases} -\hbar & \text{for } \theta_k=0 \\ 0 & \text{for } \theta_k=\pi/2 \end{cases}$$

$$\langle s_{z2} \rangle = 0.$$

What these spin expectation values represent is the direction of the spin at two different momentum points ((k_x,0) and (0,k_y)) for two different eigenfunctions given by the Eq.1.10. This precisely represent the rotation of the spin direction in the Fermi circle as shown in the Fig.1.10. Such a *vortical* spin texture in the xy-plane is the manifestation of the conventional Rashba effect.

The case of ML TMDC is very different. As mentioned earlier, the d-orbitals split into three levels due to crystal field in a trigonal prismatic coordination at the $\mathbf{\Gamma}$. The lowest energy orbital is the d_{z^2} with $l_z = 0$. Next lowest orbitals are $d_{x^2-y^2}$ and d_{xy}, which are orthogonal and degenerate at $\mathbf{\Gamma}(\overline{k}=(0,0))$. As we move towards the $\mathbf{K}$-point ($\overline{k}=(\frac{4\pi}{3a},0)$), the $d_{x^2-y^2}$ and d_{xy} orbitals not only hybridise, but do so in a way that form a giant energy splitting ($\sim$4 eV) between $l = +2$ ($d_{x^2-y^2} + id_{xy}$) and $l = -2$ ($d_{x^2-y^2} - id_{xy}$) −like states in angular momentum basis. The tight binding Hamiltonian for a ML WSe$_2$ is used

as provided in Ref. [86] to calculate the matrix elements.

$$H = \sum E_{\mu\nu}^{ij}(\mathbf{R}) \left|\phi_\mu^i(\mathbf{r}),\sigma\right\rangle \left\langle\phi_\nu^j(\mathbf{r\text{-}R}),\sigma\right| + \alpha\mathbf{L}\cdot\mathbf{S}, \tag{1.12}$$

where ϕ_μ is the basis function of the d-orbitals and $E_{\mu\nu}$ is the coupling term.

$\hat{H}$	$\lvert d_{z^2}\uparrow\rangle$	$\lvert d_{xy}\uparrow\rangle$	$\lvert d_{x^2-y^2}\uparrow\rangle$	$\lvert d_{z^2}\downarrow\rangle$	$\lvert d_{xy}\downarrow\rangle$	$\lvert d_{x^2-y^2}\downarrow\rangle$	
$\langle d_{z^2}\uparrow\rvert$	0.621	0	0	0	0	0	
$\langle d_{xy}\uparrow\rvert$	0	-0.445	$i(\alpha-1.71)$	0	0	0	
$\langle d_{x^2-y^2}\uparrow\rvert$	0	$-i(\alpha-1.71)$	-0.445	0	0	0	
$\langle d_{z^2}\downarrow\rvert$	0	0	0	0.621	0	0	
$\langle d_{xy}\downarrow\rvert$	0	0	0	0	-0.445	$-i(\alpha-1.71)$	
$\langle d_{x^2-y^2}\downarrow\rvert$	0	0	0	0	$i(\alpha-1.71)$	-0.445	WSe$_2$

Here, α is the SOC constant for W (0.258 eV). Because the inversion symmetry is broken, the spin degeneracy is lifted. The diagonal term gives the on-site energy of the orbitals, whereas the off-diagonal terms represents the hopping energy between the different orbitals (highlighted in the

23

matrix). It is critical to see that there is a huge off-diagonal hopping term between d_{xy} and $d_{x^2-y^2}$ even for $\alpha = 0$, which makes these orbitals split in energy into $l = +2$ and $l = -2$ −like states. The reason for the exceptionally large spin splitting in the case of ML TMDCs can be attributed to this fact − namely, the resultant hybridised orbital states coming from inversion breaking is split in energyninto almost "*pure*" angular momentum states, $l = +2$ and $l = -2$ −like states. The eigenfunctions calculated for the two giant spin split ($\sim$0.5 eV) pairs (A and C) and degenerate (B) pair at $\mathbf{K}$ $(\frac{4\pi}{3a}, 0)$ are:

$$
\begin{aligned}
|\psi_A, +\rangle &= + 0.7071i \, |d_{xy}, \downarrow\rangle + 0.7071 \, \left|d_{x^2-y^2}, \downarrow\right\rangle, \\
|\psi_A, -\rangle &= + 0.7071i \, |d_{xy}, \uparrow\rangle + 0.7071 \, \left|d_{x^2-y^2}, \uparrow\right\rangle, \\
|\psi_B, +\rangle &= + |d_{z^2}, \downarrow\rangle, \\
|\psi_B, -\rangle &= + |d_{z^2}, \uparrow\rangle, \\
|\psi_C, +\rangle &= - 0.7071i \, |d_{xy}, \uparrow\rangle + 0.7071 \, \left|d_{x^2-y^2}, \uparrow\right\rangle, \\
|\psi_C, -\rangle &= - 0.7071i \, |d_{xy}, \downarrow\rangle + 0.7071 \, \left|d_{x^2-y^2}, \downarrow\right\rangle.
\end{aligned}
\tag{1.13}
$$

This is in stark contrast to the case of Au (111) surface. Here only d_{xy} and $d_{x^2-y^2}$ are hybridised with equal contribution and none from d_{z^2}. The spin degeneracy is lifted in both A and C pairs and preserved in B. The spin polarisation of the pairs A and C are opposite and we should expect them to switch places at **-K**. And it is observed to be the case as the calculated eigenfunctions at **-K** $(-\frac{4\pi}{3a}, 0)$ are as follows:

$$
\begin{aligned}
|\psi_C, +\rangle &= - 0.7071i \, |d_{xy}, \uparrow\rangle + 0.7071 \, \left|d_{x^2-y^2}, \uparrow\right\rangle, \\
|\psi_C, -\rangle &= - 0.7071i \, |d_{xy}, \downarrow\rangle + 0.7071 \, \left|d_{x^2-y^2}, \downarrow\right\rangle, \\
|\psi_B, +\rangle &= + |d_{z^2}, \downarrow\rangle, \\
|\psi_B, -\rangle &= + |d_{z^2}, \uparrow\rangle, \\
|\psi_A, +\rangle &= + 0.7071i \, |d_{xy}, \downarrow\rangle + 0.7071 \, \left|d_{x^2-y^2}, \downarrow\right\rangle, \\
|\psi_A, -\rangle &= + 0.7071i \, |d_{xy}, \uparrow\rangle + 0.7071 \, \left|d_{x^2-y^2}, \uparrow\right\rangle.
\end{aligned}
\tag{1.14}
$$

Using the eigenfunctions of the Hamiltonian describing the case of ML TMDCs which represent the giant spin split valance bands at the **K**-point, we proceed to calculate the spin direction.

$$\begin{aligned}
|\psi_A, +\rangle =& \frac{1}{\sqrt{2}} \left| d_{x^2-y2} \uparrow \right\rangle + \frac{i}{\sqrt{2}} \left| d_{xy} \uparrow \right\rangle, \\
|\psi_A, -\rangle =& \frac{1}{\sqrt{2}} \left| d_{x^2-y2} \downarrow \right\rangle + \frac{i}{\sqrt{2}} \left| d_{xy} \downarrow \right\rangle.
\end{aligned} \tag{1.15}$$

With these eigenfunctions, we use the spin operators to calculate the direction of the spins in the spin split valance bands at the **K**-point. The spin expectation values are calculated to be:

$$\begin{aligned}
\langle s_{xA+} \rangle &= 0, \\
\langle s_{yA+} \rangle &= 0, \\
\langle s_{zA+} \rangle &= -\frac{\hbar}{2},
\end{aligned}$$

and,

$$\begin{aligned}
\langle s_{xA-} \rangle &= 0, \\
\langle s_{yA-} \rangle &= 0, \\
\langle s_{zA-} \rangle &= \frac{\hbar}{2}.
\end{aligned} \tag{1.16}$$

This is a quite different result compared to the conventional Rashba spin texture. Here the spin are aligned along or opposite to the z-axis, perpendicular to the momentum xy-plane (*Ising*-type). This may look like a Zeeman splitting, but it is not the case. The reason is that in a Zeeman splitting the spin polarisations are same at opposite momentum points such as **K** and **-K**. In the case of ML TMDCs however, the spin polarisation is switched at the opposite momentum points. This is a consequence of the preserved time reversal symmetry. Such a large splitting ($\sim$0.5 eV) results in extremely high effective magnetic field ($\sim$4000 T) experienced by the carriers in the spin polarised bands. Hence the
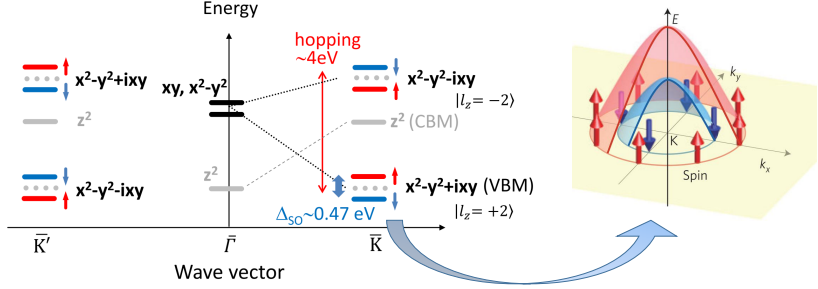
Figure 1.11: The d-orbitals close to the Fermi level are shown at Γ and $\mathbf{K}$ points. The $l = 0$ is the lowest energy orbital at the Γ-point. The $l = \pm 2$ splits into two levels sandwiching the d_{z^2} orbital at the $\mathbf{K}$-point. They in turn split into two sublevels due to the broken inversion symmetry and strong SOC [106]. On the right is the illustration of spin splitting in the valance bands at $\mathbf{K}$ as well as the orientation of the spins, reproduced from Ref. [23].

spin properties of the carriers in these spin polarised bands could be quite different from conventional materials. The evolution of the d-orbitals from Γ to $\mathbf{K}$ is shown in the Fig.1.11 along with the spin spin polarisation in the valance bands at the $\mathbf{K}$-point which is same as the spin expectation values calculated in the Eq.1.16. Such an effect in the ML TMDCs makes them a unique system to observe different new properties and phenomena that we will discuss in the following section.

1.3 Monolayer TMDCs as an arena for novel physics

We have seen that just as in the case of graphene and graphite, the properties of ML TMDCs are drastically different from bulk TMDCs. In stark contrast to bulk TMDCs, the monolayer TMDCs exhibit novel and exotic properties. First among them is the direct bandgap transition in the monolayer limit with a gap in the

visible region. This has immediate applications in opto-electronic devices [15, 26, 55, 107, 108]. Furthermore, the crystal symmetry in the monolayer limit creates a two valley system. The valley degree of freedom couples with spin of the carriers to show coupled spin-valley physics. Such a system is governed by special optical selection rules, in which a circularly polarised light can be used to manipulate the valley degree of freedom. In addition to these, monolayer TMDCs also allows us to study fundamental physical phenomena [109], including topological states [66, 79] and gauge fields induces by strain [78, 110, 111] etc.
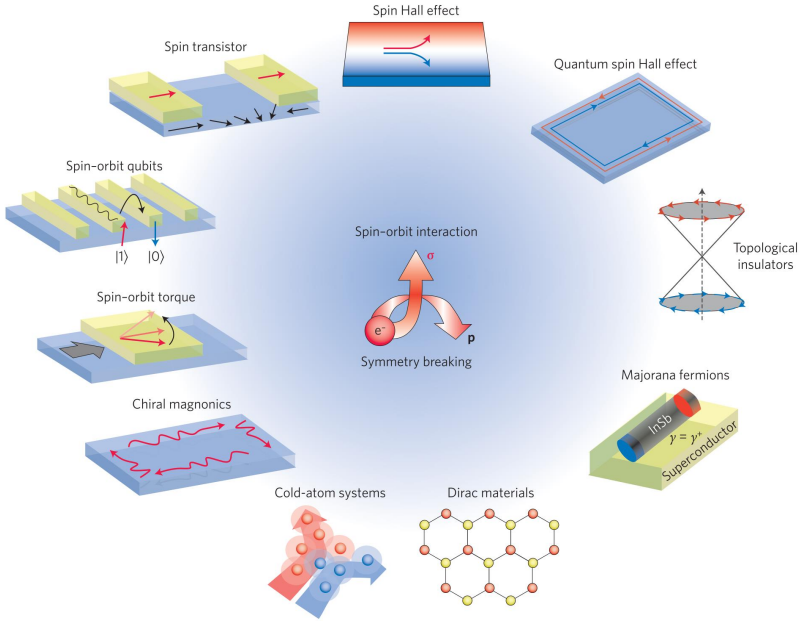

Figure 1.12: Strong spin-orbit coupling and broken inversion symmetry opens up new avenues of interesting electronic properties. This is an illustration of different sub-fields in which both magnetization and spin can be manipulated using electric fields to access various novel states. Illustration taken from Ref. [109].

1.3.1   Novel properties of monolayer TMDCs for device realisation

Coupled spin-valley physics

The two major distinctions of TMDCs with graphene is the explicit broken inversion symmetry in the monolayer limit and the strong SOC. Among TMDCs, due to the crystal structure with triangular lattice of the transition metal two distinct valleys arise. Because of the large separation of the valleys in the momentum space, the valley index remain robust against scattering. Based on these two properties, Xiao at. al. [97] predicted the presence of valley Hall effect. In the valley Hall effect, the carriers with different valley index flow opposite in the presence of in-plane electric field which is experimentally observed by Ref. [74]. The inversion asymmetry can also lead to valley dependent optical selection rules for the interband transitions, with experimental results reported by Ref. [112, 113].

The strong SOC due to heavy transition metal splits the spin degeneracy (Kramers degeneracy) of d-orbitals in the presence of an inversion asymmetry. Time reversal symmetry requires the spin splitting to be opposite in the different valleys. This feature can be exploited for the development of spin based physics and applications. The combination of spin and valley degrees of freedom could give rise to a platform with coupled spin and valley physics.

Carriers in the bands at $\mathbf{K}$ can be described with a massive Dirac equation [97]. This leads to a valley Hall effect to be present along with the spin Hall Effect. The spin or valley relaxation is suppressed as carrier scattering among opposite valleys is not allowed due to contrasting spin splitting. The coupling of spin and valley indices leads to concomitant valley-dependent optical selection rules, allowing us to manipulate the carriers with various combinations of these indices.

The robustness of spin and valley Hall effects are related to the spin and valley relaxation times and lengths. Valley index can be
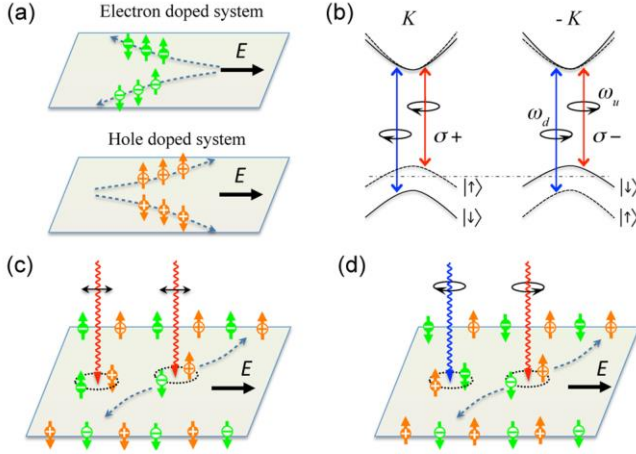
Figure 1.13: Coupled spin and valley physics in monolayer TMDCs. (a) Valley and spin Hall effects in electron and hole-doped systems. (b) Valley and spin optical selection rules. (c) Spin and valley Hall effects of electron and holes excited by polarised optical fields. (d) Spin and valley Hall effects of electrons and holes excited by two colour optical fields with opposite circular polarisation. Illustration taken from Ref. [97].

flipped when scatterers with the size of the unit cell are present. Spin flipping happens in the presence of local magnetic defects or scattering sites. In the absence of such scattering centers, the carriers are expected to have long spin and valley relaxation lengths and times. Spin and valley Hall effects leads to spin and valley carriers build up at the sample boundaries and has a potential to be exploited in the fabrication of coupled devices of spintronics and valleytronics [114–116]. This is one of the major applications of the monolayer TMDCs. To realise devices with these materials requires high quality and reliable growth techniques.

1.3.2 Applications of ML TMDCs to study exotic phenomena

Topological superconductivity

Topological superconductivity has been a holy grail in modern condensed matter physics. There have been many proposals for the realisation of a topological superconductivity [117–121]. The basic idea is to couple a normal superconductor with a topological insulator to achieve induced superconductivity in the latter though a proximity effect [122]. Another exotic paired state is the pairing with finite momentum known as FFLO state, after the proposals of Fulde and Ferrell and Larkin and Ovchinnikov [123,124]. Previous attempts in realising such modulated superconductors is by creating spin imbalance using magnetic fields [125] with exception of [126].

Hsu et. al. [72] laid out an alternate approach for the realisation of topological and modulated superconductivity. This is a dual to strategy of Fu and Kane [117], which can be realised in time reversal invariant (TRI) non-centrosymmetric system where the pair of Fermi surfaces are centred at opposite momenta $\pm\mathbf{k}$ with spin polarised electrons. The proposal is to lift the spin degeneracy in the momentum space and bring the Fermi level in between the spin split valance bands. This situation could be realized in a ML TMDCs. In such spin split double valley system, two different pairing possibilities arise. First is the intervalley pairing between opposite momenta and the other is an intravalley pairing with finite center-of-mass momentum.

Realising a topological superconductivity is highly appealing. To observe such an exotic state requires us to create a heterostructure of superconductor and spin split material (monolayer TMDC in the present context). Moreover, the Fermi level in the monolayer TMDC needs to be fine-tuned with the help of gating or doping to be in between the spin polarised bands. Unlike the gating which is a barrier for the STM experiments, doping allows for flexibility that could be achieved with our deposition tech-
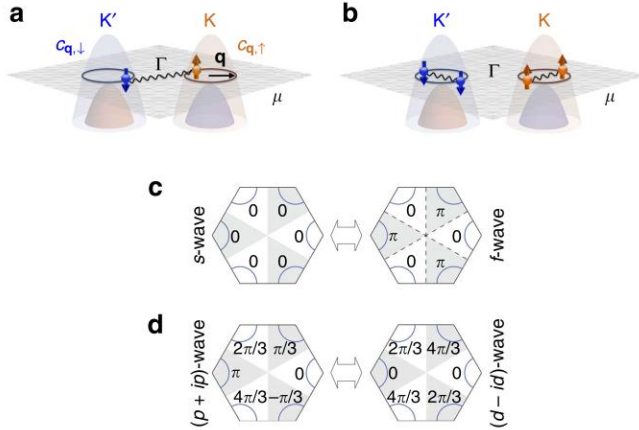
Figure 1.14: Spin split double valley centred at $\mathbf{K}$ and $\mathbf{K}'$ with Fermi level between the spin polarised valance band. (a) Intervalley pairing (b) intravalley pairing. (c) and (d) are the candidate gap functions for the intervalley pairing allowed by the symmetry group C_{3v}. Illustration reproduced from Ref. [72].

nique. This idea is the bigger agenda of which creating a clean and reliable growth method is one of its part.

Emergent gauge fields

In addition to the topological states that can be achieved by TMDCs, another fascinating phenomenon involving an interplay of mechanical and electronic properties can be found in them [78]. In thin films such as graphene, gauge like field emerge due to mechanical strain, corrugations or defects [110, 111]. Among TMDCs, such defects or impurities modulate the surface curvature of the thin films and affect the properties of electrons. In the presence of such a curvature, the thin film loses its mirror symmetry. This leads to two effects; first, the chirality would not be a good quantum number and second, the orbital wave functions are rotated with respect to local normal giving rise to

gauge fields. Such an effect could be observed by measuring the local density of states modified by the curvature in a scanning tunnelling microscopy.
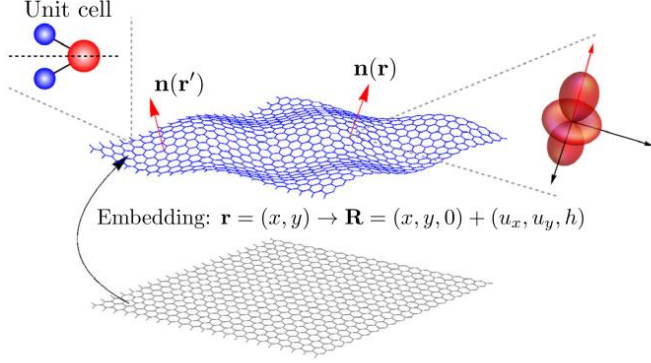

Figure 1.15: Corrugated TMDC crystal in the 2H phase as a membrane. Red arrows are the local normal vectors. Unit cell of one transition metal and two chalcogenide atoms is shown with mirror plane in dashed line. The rotation of the orbitals is shown with respect to local normal. Illustration reproduced from Ref. [78].

Potential to observe this phenomena is very real. Although the chances of ripples and corrugations to be present are much more in an exfoliated monolayers, there are no reports yet to our knowledge which used monolayers grown with bottom up approach. This is a relatively unexplored phenomena that we could study in the future with h-PLD grown monolayer TMDCs.

1.4   Why monolayer WSe_2?

We have seen that atomically thin TMDCs provides an arena for a rich variety of novel physics. Among the TMDCs, we have selected WSe_2 as a material of interest for this thesis. Here we elaborate some of the reasons for us to focus specifically on WSe_2. Firstly, although the band structure of monolayer WSe_2

qualitatively looks similar to that of ML MoS$_2$, detailed exci-
tonic energy scheme was found to be different. Namely, dark
(non emitting) exciton forms the lowest energy level for W based
TMDCs (WS$_2$ and WSe$_2$) unlike the Mo based ones (MoS$_2$ and
MoSe$_2$) [113, 127–130]. Thus, comparative study on Mo and W
materials could lead to a deeper understanding of excitonic and
optical properties of TMDC monolayers. Second, strong SOC of
W compared to Mo makes the spin splitting in the valence band
larger for W-based TMDCs, reaching the largest value of 430-510
meV for WSe$_2$ [7, 131, 132]. The latter point is what we would
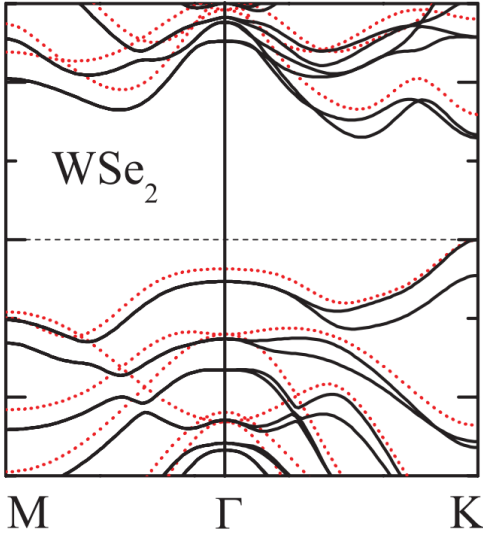like to focus in this thesis.

Figure 1.16: The elec-
tronic band structure
of ML WSe$_2$ calcu-
lated from the first
principles with SOC
(solid) and without
SOC (dotted), as re-
ported by Ref. [26].

There are a few advantages in studying monolayer WSe$_2$ for
its large spin splitting. First, the large spin splitting opens up a
possibility to tune the Fermi energy in such a way that only one
component of spin is occupied at a given **K**-point. If the spin
splitting is less than 10 meV as for the case of many Rashba ma-
terials, such fine tuning will be difficult. Thus, the spin splitting
of the order of 0.5 eV is tremendously advantageous to explore
spin dependent phenomena in transport. Second, because ML

WSe$_2$ has the largest spin splitting, this also means that it has the largest effective magnetic fields associated with it (~ 4000 T). This means that the effect brought about by the spin-momentum locking effect is maximal among any other known material. Finally, this fact, combined with the distinct form of spin texture where spin always points perpendicular to the 2D plane (Ising type spin splitting), makes WSe$_2$ the most appealing platform to study interesting physics that can be induced by the interplay of SOC and other electronic phase. Most notable possibility along this line is the engineered topological superconductivity by the use of proximity effect.

1.4.1 What has been done with monolayer WSe$_2$?

Initially, MoS$_2$ attracted most of the attention among TMDCs. However recently, WSe$_2$ is also becoming a target of intensive research because of a few distinct features compared to Molybdenum based systems and also in part due to the largest spin splitting [26, 86, 97]. Starting with the synthesis and characterisation, some of the important previous studies on ML WSe$_2$ will be reviewed here.

TMDC thin films, including ML WSe$_2$, have been synthesised using different methods. There are two basic approaches, first is the top down and the second being the bottom up. Top down methods starts with high quality single crystals and thin down to the ML limit either by using mechanical force, or liquid exfoliators. Bottom up approach, on the other hand, starts with constituent elements as a raw material to grow the required thin film. ML WSe$_2$ has been synthesized using mechanical exfoliation [133–147], chemical vapour deposition (CVD) [87,91,95,148–162], molecular beam epitaxy (MBE) [163–166], and pulsed laser deposition (PLD) [60,61,63,167–174].

Just as in the case of molybdenum, tungsten dichalcogenides also have a transition from an indirect to a direct band gap in the monolayer limit. The optical spectra of monolayer WSe$_2$ is sharper compared to that of the bulk, but with significant overlap
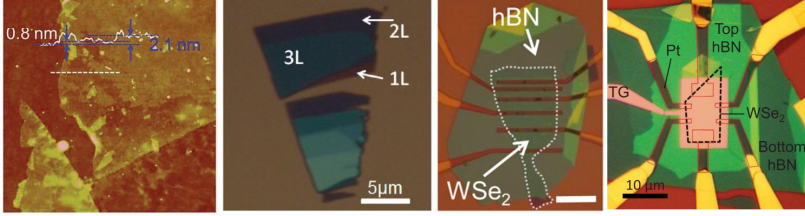
Figure 1.17: Evolution of the quality of ML WSe$_2$ as inferred by optical microscopy images from different groups. Sources from left to right, [133, 134, 140, 142].
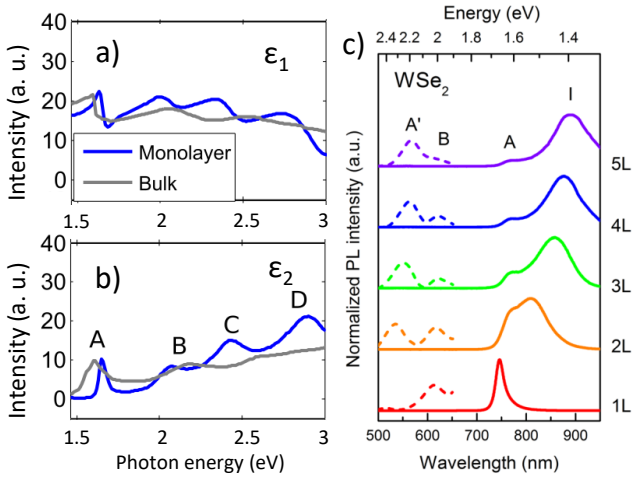

Figure 1.18: (a,b) Components of complex dielectric function of ML WSe$_2$ compared with bulk. The spectral features are broadened in the bulk, but the overlap with ML limit is significant [108]. (c) Photoluminescence spectra of 2H-WSe$_2$ with different thickness, including monolayer as reported by Ref. [92].

as shown in Fig.1.18(a,b) [108]. Thus, only using optical spectra for the identification of a monolayer could allow some room for uncertainty. On the other hand, the spectral features of PL are drastically different between monolayer and bilayer TMDCs as

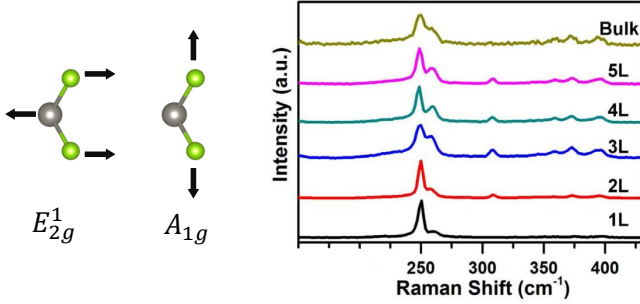shown in Fig.1.18(c) [92]. Hence, PL is widely used in the TMDC community to reliably identify the monolayers.

Figure 1.19: The phonon modes E^1_{2g} and A_{1g} in the ML TMDCs. These modes are degenerate and located at 250 cm^{-1} in the Raman spectra of ML WSe$_2$. Raman spectra of WSe$_2$ with different thickness, including monolayer limit obtained with 514.5 nm laser. Two signatures of ML WSe$_2$ are the degeneracy of the two modes and the absence of the peak at 310 cm^{-1} [175].

Similarly, the Raman spectra change between the bulk and monolayer samples of WSe$_2$. There are two prominent features as can be seen in the Fig.1.19. The degeneracy of E^1_{2g} and A_{1g} in the monolayer WSe$_2$ is lifted in the thicker samples. Second, the peak at 310 cm^{-1} absent in the monolayer starts to evolve in the thicker samples. These features in Raman response are often used in identifying the monolayers as well [175,176].

The electronic band structure of identified monolayer WSe$_2$ could be directly visualized using ARPES. Due to the broken inversion symmetry and strong SOC, the spin degeneracy is expected to be lifted at the **K**-point in the Brillouin zone. Ref. [177] reported the largest spin splitting of 0.513 eV in an exfoliated ML WSe$_2$. They compared the experimental data with the first principles calculation and found the splitting to be far from expected 450-470 meV. On the other hand, ARPES of the MBE grown samples showed the spin splitting in the range of 0.43 eV to 0.5

eV [7,131,132]. The large variation of the spin splitting is thought
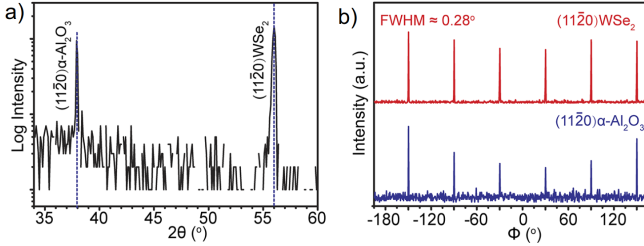to be arising due to the strain in the ML WSe$_2$ [7].

Figure 1.20: Laboratory based (a) in-plane XRD and (b) in-plane
rocking scan of the ML WSe$_2$ grown on Al$_2$O$_3$ (001) using CVD
technique as reported by Ref. [162].

Despite the importance of clarifying quantitative strain, to our
knowledge, only two groups undertook the laboratory based X-
ray diffraction studies of WSe$_2$ thin films [162,166]. Among them,
only Ref. [162] reported the X-ray diffraction of ML WSe$_2$. ML
WSe$_2$ was grown by CVD method on Al$_2$O$_3$ (001) substrate. A
crystallographic orientation locking was found between the mono-
layer and the substrate, which was also found in 10ML WSe$_2$ by
Ref. [166]. Authors of these studies, however, do not report on
quantitative values for in-plane lattice constant and strain. This
may be related to the limited accuracy (low signal to noise ra-
tio) in the data taken by laboratory based XRD especially for a
monolayer material.

Largely based on the experimental techniques being devel-
oped in the past decade to study graphene, the electronic trans-
port properties of monolayers of TMDCs were being investigated.
Most often FETs are fabricated and the electron or hole proper-
ties were studied, such as Refs. [140,178,179]. Although such an
effort is crucial for device applications, very few investigated the
spin related phenomena that could arise in the transport in these
materials.

Although little transport study has been performed to mea-

sure spin properties in a few layer TMDCs, one notable exception is the work [28] which revealed spin relaxation time via quantum transport. For this purpose, a dual gated exfoliated ML $MoS2_2$ is used. The inverse relation between the estimated spin relaxation time and the momentum relaxation time suggests Dyakonov-Perel mechanism for the spin relaxation of the electrons. As of now, no such studies were conducted on ML WSe_2 or investigated in the hole doped region which is critically important to examine the effect of large spin splitting.

1.4.2 What needs to be done with monolayer WSe_2?

I will restate the open questions from the previous studies here. There is a large variation in the experimentally measured value of the spin splitting in the ML WSe_2 among the ARPES studies. It is speculated that the variation might have its origin in the strain of the monolayer samples [7]. However, there is not any precise estimation of the strain using any diffraction techniques. Furthermore, although some work has been performed on the general electrical transport, systematic investigation of the spin properties in the hole doped ML WSe_2 is still missing. Among the available literature, the carrier density is modulated using electrostatic gates. This introduces another symmetry-breaking component to an already inversion asymmetric monolayer which could bring complexity in the form of spin-momentum locking effect. Namely, vortical spin texture (conventional Rashba type) could be mixed to the pristine Ising type [23–25].

To address these questions, we propose a new bottom up approach to synthesise ML WSe_2. This should result in an epitaxial effect in the grown ML WSe_2. Such an epitaxy facilitates high precision structural characterisation using synchrotron based XRD/GIXRD to evaluate precise strain present in the monolayer. Simultaneously, we perform ARPES experiment to map the electronic band structure of the ML WSe_2. These two experiments along with our first principles calculations should provide an experimental reference of strain and magnitude of spin

splitting. Moreover, instead of gating our WSe$_2$ thin films, we plan to modulate the Fermi level towards the valance bands using Nb as a dopant. This removes the complication of additional symmetry-breaking gate and represent realistic environment to study the spin properties of the carriers in the valance bands of WSe$_2$. Based on such a novel synthesis route for ML WSe$_2$ and the fabrication of van der Waals heterostructures, new artificial materials with tailored properties could be created.

1.5   Motivation of the present work

In order to move into a new era of materials, it is essential to understand their physical characteristics. Since the new class of material platform associated with new device or physics often comprises heterostructures consisting of different materials, it is important to know the behaviour of a material prepared in a way it can be incorporated in such a complex structure. Besides this requirement set by a potential usefulness in technology, the possibilities to explore new avenues of physics in low dimensions are immense. In both pathways toward future, a clean and reliable method to synthesise materials is crucial.

In this thesis work, the open questions in the field of atomically thin TMDCs raised in the previous section will be addressed. To achieve this goal, we need to overcome a few challenges. They are, (1) the synthesis of an epitaxial ML WSe$_2$, (2) measurement of the precise lattice parameters, (3) direct probe of the electronic band structure and (4) study the spin or valley properties of the carriers in the valance band.

1. First challenge is to establish a clean and reliable technique to grow ML WSe$_2$ in a bottom up approach. To overcome the drawbacks of the methods currently used to synthesise TMDCs, in particular WSe$_2$ thin films, we propose new method of *hybrid*-PLD as an alternative. Using this technique, we demonstrate the synthesis of WSe$_2$ thin

films down to the monolayer limit. Moreover, we will show evidence for the synthesis of a prototypical van der Waals heterostructure of ML WSe$_2$ and graphene.

2. We aim to obtain insights into epitaxial effects on the ML WSe$_2$ due to the substrates. Since strain is known to have drastic effect on the electronic properties of WSe$_2$, and also because quantitative evaluation of strain in monolayer WSe$_2$ is scarce in existing literature, our objective is to fill the missing knowledge.

3. Use ARPES to map out the electronic band structure of an epitaxially grown ML WSe$_2$. In particular, we directly probe the magnitude of the spin splitting in the valance band at the **K**-point and compare it with the theoretical prediction and past experiments in related systems. Using available experimental techniques and first principles calculations, a possible phase space for the magnitude of spin splitting as a function of epitaxial strain could be constructed.

4. After detailed structural and electronic characterisation of ML WSe$_2$ grown on different substrates, we study the electronic properties in hole doped WSe$_2$ thin films. With this we not only demonstrate the efficiency of doping with our technique, but provide an alternative to the gating technique to study the carrier transport in the valence band.

With the evidence of synthesis of ML WSe$_2$ and prototypical van der Waals heterostructure, we expect to extend this technique for the fabrication of other artificial heterostructures. Thus, the created artificial materials would allow us to explore the physics hidden in lower dimensions such as the possibility of induced superconductivity in the spin polarised bands.

1.6　The strategy and structure of the thesis

The present thesis work is to create giant spin-split system of ML WSe$_2$ using epitaxial bottom up approach. This approach will provide a platform to study electronic properties in a spin split material, with a future prospect of coupling them with other electronic phases.

We start with the development of a novel technique for the synthesis of ML WSe$_2$. Followed by the structural and electronic characterisation using X-ray diffraction (XRD) and angle resolved photoemission spectroscopy (ARPES) to estimate the strain and confirm the spin splitting of the valance bands.

Four major experimental milestones to be addressed in this thesis are as follows. First, a unique and versatile method for the fabrication of epitaxial ML is addressed. Second, experimental techniques suitable for the identification of monolayer are introduced. Third, detailed structural and electronic characterization is performed on epitaxial films of ML WSe$_2$ identified in the second step. And finally, a direct measurement of doping effects that could modulate the electronic properties in epitaxial films is provided.

The key questions related to these milestones are: Is it possible to fabricate and demonstrate the synthesis of ML WSe$_2$? Is it possible to quantitatively evaluate the substrate effects on the physical properties in ML WSe$_2$? Is the spin splitting observed at the **K**-point in the Brillouin zone as predicted by theoretical work? And is it possible to change the electronic conductivity of WSe$_2$ thin films by doping with another element?

Our strategy can be summarized as follows:

1. Use of unique method for TMDC film growth that has a few distinct merits (such as doping) compared to conventional CVD and MBE. *Hybrid*-pulsed laser deposition is proposed in this context.

2. Emphasis on direct and precise determination of structure

and strain in monolayer materials. Synchrotron based grazing-incidence XRD (GIXRD) is adopted with this motivation.

3. Use of ultra-high vacuum (UHV) based direct character-ization tools which are compatible with our growth tech-nique. Angle-resolved photoemission and X-ray photoemis-sion (XPS) spectroscopies were utilized taking advantage of h-PLD being a UHV-based technique.

4. Use Nb as an elemental substitution of W in the WSe_2 thin films to manipulate the electronic conductivity.

The following part of this thesis is structured as follows; Chap-ter 2 consists of explanation of different experimental and theoret-ical methods used in the present thesis, starting with *hybrid*-PLD to synthesize ML WSe_2, followed by characterization techniques and band structure calculations using the first principles method. Chapters 3 - 6 deal with the results and discussion of the different experiments performed with ML WSe_2. The first critical step is a demonstration of ML WSe_2. Then we clarify the electronic band structure and strain effect directly by ARPES and synchrotron-based XRD, respectively. Finally we show the electronic trans-port properties of hole-doped WSe_2 thin films. Chapter 7 sum-marizes the results and elaborates the significance of the present thesis.

2. Experimental and theoretical methods

2.1 Thin film deposition

2.1.1 Introduction

Thin films are synthesised using one of the many available deposition techniques. Among them, physical vapour deposition methods, such as CVD and MBE are simple in working principle. CVD uses either chemical compound or precursors in a vacuum sealed tube with differential temperature gradient. The compound vaporizes from the hot region to be deposited on substrate at cooler region of the tube with the help of transport gas such as, Ar or H_2. Although high quality thin films are deposited using CVD, and number of layers is difficult to be controlled.

In contrast, MBE is much better suited for precise number of layers of the deposited thin film. Usually, MBE employs Knudsen cell (k-cell) or effusion cell (e-cell) for evaporation of the chemical components. For materials such as transition metals with very low vapour pressures, electron beam (e-beam guns) evaporators are used. Major drawback of e-beam gun is relative difficulty in controlling the flux rate and the increased complexity, especially when multiple materials need to be evaporated using this

approach as required for doping or heterostructures.

2.1.2   Pulsed laser Deposition (PLD)

To overcome these issues, PLD is used. PLD has been around
since immediately after the invention of lasers in the 1960s. In
PLD, the laser of sufficiently high energy density is focused on
a target of the material that is to be evaporated. Forgotten and
rediscovered in the 1980s as a powerful tool to deposit epitaxial
oxide superconducting thin films. This was because it was chal-
lenging to deposit thin films with multiple cations with different
evaporative properties in a right stoichiometry to realize super-
conducting thin films. The main characteristics of this method
are the stoichiometric transfer of the target material and simplic-
ity of the setup and its operation [180].

Laser with a UV wavelength and nanosecond pulse width is
strongly absorbed by small volume of the target. Depending on
the optical properties of the target material and the laser used,
photons penetrate ($\sim$10 nm) the surface into the bulk of the tar-
get. The electric field of the laser pulse is strong enough to ionize
the atoms at the surface of the target and excites the electrons
in the bulk, which heats up the material and evaporates. The
plasma plume of evaporated material moves in highly forward
direction towards the substrate. Stoichiometric transfer of the
target material, creation of energetic elemental species, and wide
range of workable background pressure makes PLD suitable for
the growth of many class of materials including, layered systems,
nanorods and even biomaterials [181].

2.1.3   Practical aspects of PLD

The laser energy density, or laser *fluence*, determines the absorp-
tion behaviour of the target material. When the fluence is low, the
target is heated and material is ejected due to evaporation pro-
cess. The evaporation flux is dependent on the vapour pressures
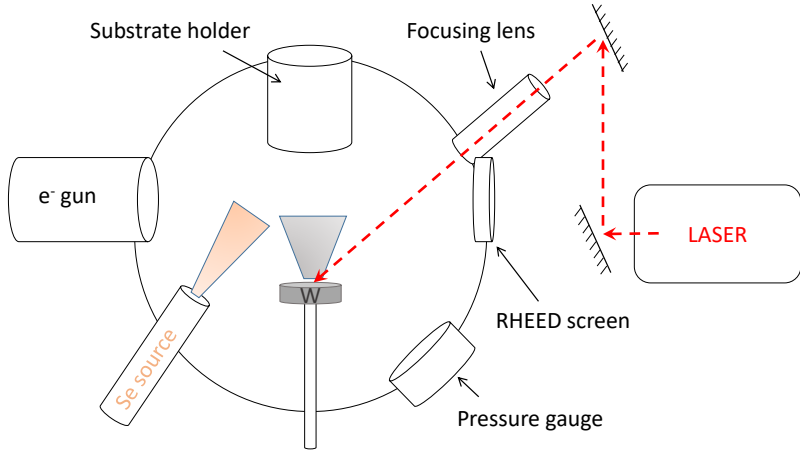of constituent elements. As the fluence is increases, it absorbs

Figure 2.1: Schematics of *hybrid*-Pulsed laser deposition system showing major components.

the energy more than needed for evaporation. At higher fluence, the excess energy absorbed is used to create plasma of the target material and imparts high kinetic energies to it [182, 183].

The target can be of different phase than the desired thin film, as long as the stoichiometry remains the same. The rate of deposition can be manipulated by changing the target properties. Single crystal target can be used if it has sufficiently high absorption coefficient. Or create polycrystalline target to incorporate grain boundaries and cracks, which enhances absorption of the laser energy. Single crystal metal target have slow deposition rate due to high reflectivity and thermal conductivity. When a composite target is used, the process however, falters as the time progresses due to differential evaporation of elements in the target and changes the target composition and consequently the deposited thin films.

Background gas can introduce two functions. First, it reacts with the ablated material to form the desired compound before reaching the substrate. Second, it slows down the ablated mate-

rial. Spectroscopic studies have shown that the kinetic energy of the ablated material to be in the order of several hundred electron volts and the background gas can reduce it to few electron volts [183, 184].

The rate of deposition of the thin films using PLD depends on multiple factors, such as the laser energy density, spot size, the distance between the target and the substrate, and the background pressure, etc. At a constant deposition condition, the thickness can be controlled just by the number of pulses of the laser.

Another significant aspect of PLD is that the growth mode of thin films much different from that of other physical vapour deposition methods such as CVD and MBE. PLD is typically an out of equilibrium process, in which the kinetic effects of the evaporated particles becomes important, whereas in equilibrium process like an MBE, the thermodynamics of the evaporation process takes an important role.

2.1.4   Growth modes of the thin films

Depending on the interaction between the evaporated adatoms and the substrate, the growth modes can be classified into three types [185].

First case is when the interaction between the adatoms is stronger than the interaction of atoms and the substrate, the evaporated material coalesce to form islands. Since the movement of the adatoms on the substrate surface is not smooth, multiple islands starts growing simultaneously. This mode is called *island growth mode or Volmer-Weber growth mode.* Due to the formation of islands, the RHEED intensity decreases drastically with increasing surface roughness.

Second type of growth mode is the other extreme, in which, the interaction between the adatoms is not strong and the atoms can move freely on the substrate surface. The particles move over the surface until they reach the step edge to create a layer of material before forming the next layer. This mode is called
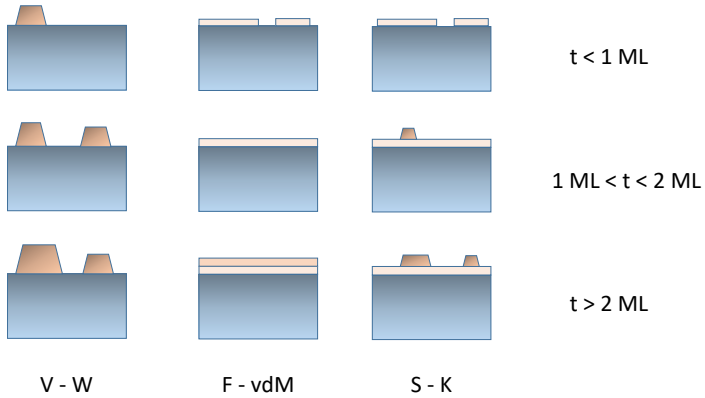
Figure 2.2: Different modes of thin film growth. Volmer-Weber (V-W), Frank–van der Merwe (F-vdM) and Stranski–Krastanov (S-K)

layer by layer mode or Frank–van der Merwe mode. During this process, the RHEED intensity oscillates between low and high corresponding to half covered and fully covered layers of the thin film, respectively.

Third type is in between the above mentioned two modes. Initial layer or few layers start with layer by layer mode and then the interaction between the adatoms creates islands. This is called *layer-island growth mode or Stranski–Krastanov growth mode.*

2.1.5 *hybrid*-Pulsed laser deposition

The present work will demonstrate the feasibility of PLD to synthesise ML WSe$_2$. With this method, we can dope the few layer WSe$_2$ with different element (e.g. Nb) in order to manipulate the Fermi level, to access interesting region in the Brillouin zone. For this thesis work, we developed and custom built a modified pulsed laser deposition system. Different instruments are used

for the growth and characterisation of WSe$_2$ thin films. All the different components of instruments required for the growth and monitor the growth process are mounted on custom designed vacuum chamber. In total we have 14 ports to use for different purposes. The basic components are the target holder that is attached at the bottom and the substrate heater mounted on the top. Thereafter, other instruments come into picture. Other major components that were used during this work include, effusion cells (e-cells), pyrometer, quartz crystal monitor (QCM), RHEED gun and screen, and most important of all, the turbomolecular pumps.
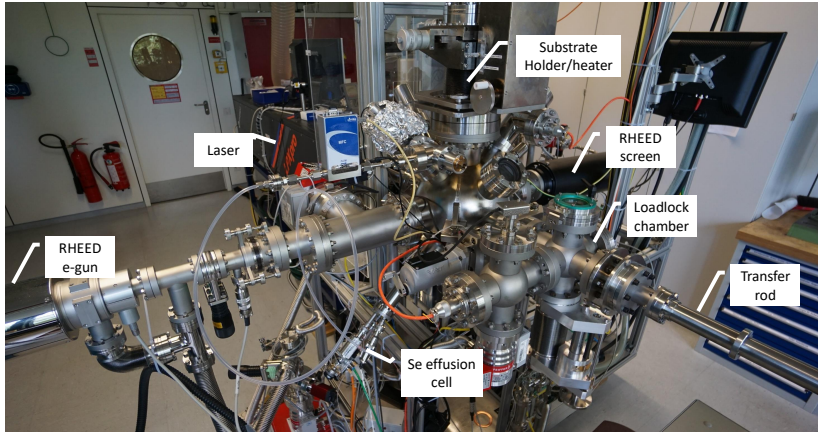
Figure 2.3: *hybrid*-Pulsed laser deposition system used during the present work.

For the deposition of WSe$_2$ thin films, we have to overcome a few of the problems discussed in the methods of thin film deposition. They are,

1. evaporate low vapour pressure transition metal, tungsten (W)

2. avoid degradation of the target material

3. simplify the doping process

To address the first problem, we use excimer laser to evaporate tungsten. Throughout the thesis work, we have used high duty excimer laser, *LPXPro 210* from COHERENT. It uses KrF as working gas for a laser output with 248 nm wavelength. Using this we can obtain maximum of 800 mJ which can be reduced with attenuators or an *iris* aperture. The advantage of iris compared to attenuators is that we can maintain same energy density with lower total energy averaged over the iris area. The duration of each pulse is 20 ns, whereas the number of pulses and the frequency of pulses can be programmed to the suitable need. The laser optics is optimised to have a spot size of 1×2 mm^2 on the target. This results in fluence in the range of $\sim$ 3-7 J cm^{-1} depending on the energy incident on the laser window.

And the second issue is solved using pure tungsten target and supply selenium (Se) using an effusion cell. Tungsten (99.99%) discs of diameter 7-12 mm and thickness of 5-8 mm are pressed into stainless steel conical pucks. These pucks are placed in target holders which are mounted on a custom designed target exchange and rotation mechanism. The target exchanger, has a capacity of 3 different targets. This allows us to change between different targets during the deposition of thin films, which is quite an important feature that enables us to dope the thin films or create heterostructures without breaking the vacuum. This mechanical contraption is quite simple in principle and working. It allows each target to rotate, which results in fresh surface for the laser pulse. Otherwise, the target suffers cavitation and the direction of the flux could change away from the substrate.

Effusion cells are mounted to evaporate chalcogen element. This allows us to evaporate high vapour pressure elements, such as Se with a stable flux. Se pellets (99.999%) are filled into pBN crucible, which is placed into the e-cell. pBN is used to withstand the large changes in the temperature of Se which puts additional sheer stress on the crucible walls. This is noticed to break quartz crucibles. Hence the use of quartz crucible is discontinued. The density of the heating element at the mouth of the crucible is
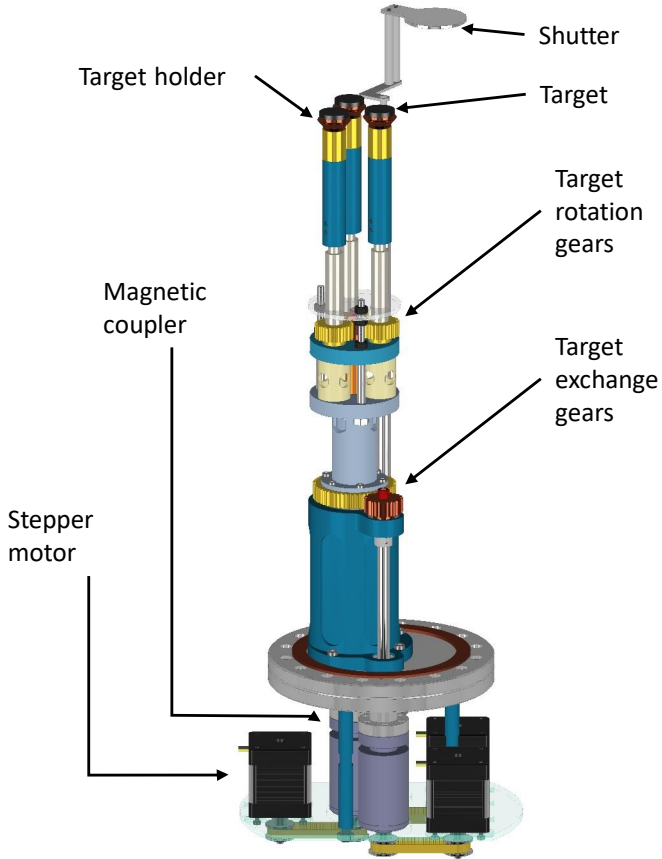
Figure 2.4: Custom designed target exchanger with different parts labelled.

higher to avoid Se build up, which could block the Se flux. In addition, it is fitted with a pneumatic shutter to allow or stop the flux instantaneously. The angle of the effusion cell is focused towards the substrate from the side ports.

This is a *hybrid* approach because it combines the functions of both PLD and MBE. This technique is also known as MBE

assisted PLD or laser assisted MBE. We would call this *hybrid* deposition as *hybrid*-pulsed laser deposition (*h*-PLD). The third issue of doping is simplified because we need to simply switch the target or use an alloy, which we used for the present thesis.

Before starting the deposition, we check the rate of Se flux using a QCM. We start with pristine quartz crystal with resonant frequency of 6 MHz. As the Se starts depositing on the crystal the frequency changes allowing us to measure the thickness of the Se film deposited. Knowing the rate of change of thickness, the flux of Se is estimated. Throughout our experiments, we have used Se flux at an average rate of ~1.5 Å/s.

Another significant asset of our deposition chamber is the RHEED. We have installed RHEED-30 from STAIB instruments. This includes a differential pumping system that allows to use RHEED in relatively higher pressures. The energy of the electrons can be varied between 500 eV to 30 keV. We have used 10 keV throughout this thesis work. In addition, electron beam rocking and steering system enables us to access different parts of the sample. Although RHEED is used to monitor the growth of thin films, our deposition conditions, especially high Se atmosphere limited its use only in the beginning and at the end. So we were able to observe the 3D Bragg spots from substrate in the beginning and line streaks in the end due to two dimensionality of the grown ML WSe_2.

During the deposition and for post deposition annealing processes, we have custom designed substrate heating system. We have used high vacuum compatible magnetically coupled manipulator to fix our heating elements. 1 mm thin graphite coil with $2\ \Omega$ resistance is used as substrate heating element. This is connected to the vacuum flanges with electrical feedthrough electrodes with metallic bands made out of silver. A metallic cage is built around the heating element which holds the substrate holder without touching the heating elements. This distance between he graphite coil and the substrate is 10 mm. The temperature of the substrate is initially calibrated with a pyrometer and the tem-
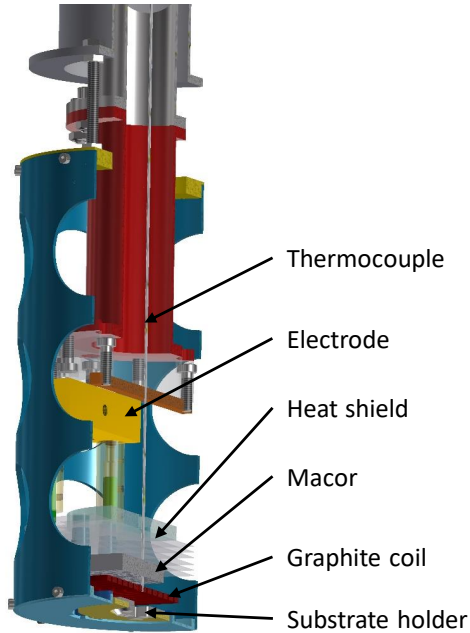
Figure 2.5: Substrate heater with different components labelled.

perature is measured at the centre of the graphite coil using a
thermocouple. To protect the silver bands behind and focus the
heat generated to the substrate, a heat shield is made out of *ma-
cor* and tantalum metal sheets are placed in the form of a stack.

2.2 X-ray diffraction (XRD)

2.2.1 Introduction

X-ray diffraction (XRD) is one of the most important methods to
investigate the structure of matter, in which the electrons scatters
the incident X-rays. This method is successful with both simple
and complex materials. Using the angles and the intensity of the
scattered X-rays, 3-dimensional atomic crystal structure can be

determined. With the subtle changes in the angle of diffraction, stresses, disorder and impurities, etc. can also be evaluated. Being one of the widely used techniques, great amount of literature such as [186] is already available. Here we present the basic ideas required for understanding of our diffraction experiments.

In most cases, monochromatic X-rays are used. Monochromatic X-ray beams are characterized by its fixed wavelength λ or its equivalent wavenumber $k = 2\pi/\lambda$. The oscillating electric field is described by a sine wave or with more compact complex form.

The spatial and temporal information can be incorporated into a simple expression for the electric field as,

$$\mathbf{E}(\mathbf{r}, t) = E_0 e^{i(\mathbf{k} \cdot \mathbf{r} - \omega t)} \hat{\varepsilon}. \tag{2.1}$$

This is the Maxwellian description of electromagnetic waves. From quantum mechanical perspective, monochromatic beam can be quantized into photons with energy $\hbar\omega$ and momentum $\hbar\mathbf{k}$. Intensity of the beam is the number of photons passing through an area per unit time. We can estimate the wavelength for a given energy of X-ray beam from the following expression,

$$\lambda[] = \frac{hc}{\varepsilon} = \frac{12.398}{\varepsilon[keV]}. \tag{2.2}$$

2.2.2 Scattering from an electron

Starting with the basic unit of scattering, the electron is forced to oscillate in the electric field of X-rays. This electron acts like a secondary source emitting the scattered X-rays. In most cases, the scattered X-rays have the same wavelength as the incident one. This is the case of *elastic* scattering. In the case of *inelastic* scattering, the incident ray is scattered with different wavelength, resulting in Compton scattering. However the momentum vector can change even in the elastic scattering. This leads to the definition of the *scattering vector*, $\mathbf{Q}$ which satisfies the following relation,
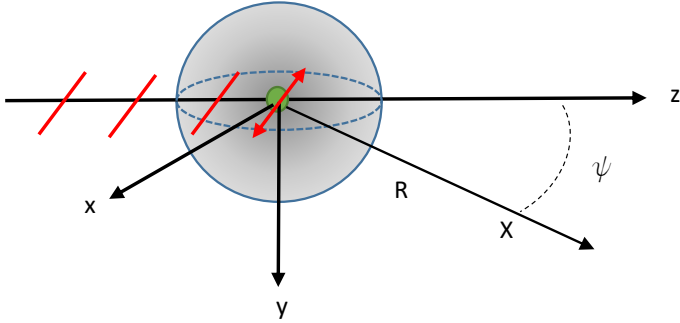
Figure 2.6: The classical description of the scattering of an X-ray by an electron. The electric field of an incident plane wave sets an electron in oscillation which then radiates a spherical wave. The incident wave propagates along the z axis and has its electric field polarised along x. The wave crests of the incident wave lie in between those of the scattered spherical wave because of the 180° phase shift in Thomson scattering.

$$\hbar\mathbf{Q} = \hbar\mathbf{k} - \hbar\mathbf{k}', \qquad (2.3)$$

where $\hbar\mathbf{k}$ and $\hbar\mathbf{k}'$ are the initial and final momenta. And $\mathbf{Q}$ is expressed in the units of $\mathring{A}^{-1}$. The ability of an electron to scatter is expressed in terms of *scattering length*, which can be derived from classical description for the electromagnetic fields. The scattered field at position X at a distance R from the scattering section and an angle of ψ is

$$E_{rad}(R,t) = -\left(\frac{e^2}{4\pi\epsilon_0 mc^2}\right) E_{in}\frac{e^{ikR}}{R}\cos\psi. \qquad (2.4)$$

The prefactor of the spherical wave $\frac{e^{ikR}}{R}$ is denoted by r_0, known as *Thomson scattering length*. The factor of $\cos\psi$ governs the acceleration of the electron, observed to be decreasing at X

with increasing ψ. It is zero at $\psi = \pi/2$. The intensity of the radiation is defined to be the square of the electric or the magnetic field, we can express a new parameter, *differential cross-section*. The differential cross-section for the Thomson scattering is given by,

$$\left(\frac{d\sigma}{d\Omega}\right) = \frac{I_{sc}}{I_0 \Delta\Omega} = r_0^2 \cos^2\psi. \tag{2.5}$$

This expression can be generalized as,

$$\left(\frac{d\sigma}{d\Omega}\right) = r_0^2 P, \tag{2.6}$$

where P is the polarization factor which depends on the X-ray source.

$$P = \begin{cases} 1 & \text{synchrotron: vertical scattering plane} \\ \cos^2\psi & \text{synchrotron: horizontal scattering plane} \\ \frac{1}{2}(1 + \cos^2\psi) & \text{unpolarised source} \end{cases}$$

$$\tag{2.7}$$

Polarization factor for the synchrotron source arise due to the horizontal plane of electron orbit. Since the acceleration is in the horizontal plane, the emitted X-rays are linearly polarized in the plane and elliptically polarized in out-of-plane.

2.2.3 Scattering from an atom and unit cell

Next step is to consider the scattering of X-rays by an atom with Z electrons. Classically speaking, the electron distribution is specified by the charge density $\rho(r)$. The scattered field is the superposition of contributions from different charge volume elements. Let the incident and scattered momenta be $\mathbf{k}$ and $\mathbf{k}'$, then the phase difference between them is $\Delta\phi = (\mathbf{k} - \mathbf{k}') \cdot \mathbf{r} = \mathbf{Q} \cdot \mathbf{r}$. Assuming $|k| = |k'|$, the scattering vector yields to be $|Q| = 2|k|\sin\theta$. The scattering volume element $d\boldsymbol{r}$ at $\mathbf{r}$ contributes an amount

-$r_0\rho(\mathbf{r})d\mathbf{r}$ to the scattered field with a phase factor of $e^{i\mathbf{Qr}}$. Total scattering length of an atom is

$$-r_0 f^0(\mathbf{Q}) = -r_o \int \rho(\mathbf{r})e^{i\mathbf{Qr}}d\mathbf{r}. \qquad (2.8)$$

$f^0(\mathbf{Q})$ is the *atomic form factor*. In the limit of $\mathbf{Q} = 0$, all volume elements scatter in phase and the atomic form factor can be taken to be Z, the number of electrons in the atom. On the other limit of large $\mathbf{Q}$, all volume elements scatter out of phase and the atomic form factor becomes *zero*. The core electrons are affected less compared to the valence electrons. This results in the correction factor to include the binding energy of the electron shell, $f'(\hbar\omega)$; and correction factor to include the absorption by $if''(\hbar\omega)$. The full atomic form factor is,

$$f^0(\mathbf{Q},\omega) = f^0(\mathbf{Q}) + f'(\hbar\omega) + if''(\hbar\omega). \qquad (2.9)$$

Extending the idea of scattering length of an atom with form factors to the atoms in the unit cell,

$$f^{uc}(\mathbf{Q}) = \sum_{\mathbf{r}_j} f_j(\mathbf{Q})e^{i\mathbf{Q}\cdot\mathbf{r}_j}. \qquad (2.10)$$

Just as before, $f_j(\mathbf{Q})$ is the atomic form factor of the jth atom in the unit cell. Single unit cell cannot have enough signal to determine the structure of the material. Hence, large number of unit cells are needed to give average signal of oriented atoms.

2.2.4 Scattering from a crystal

A crystal is formed with periodic arrangement of atoms or unit cells. The interference of the X-rays due to the lattice planes formed from periodic arrangement results in the diffraction pattern. Constructive interference occur when the path difference between scattered waves is equal to the integer multiple of the wavelength λ. For an incident wave with an angle θ with the

scattering planes d distance apart the *Bragg's* condition is given by,

$$m\lambda = 2d\mathrm{sin}\theta, \qquad (2.11)$$
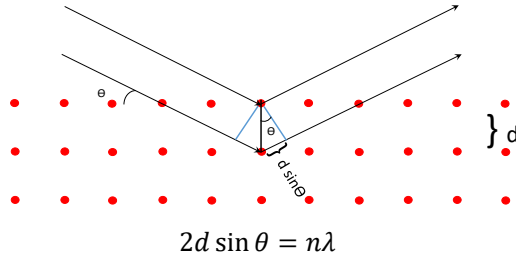

$$2d \sin \theta = n\lambda$$

Figure 2.7: Illustration of Bragg's law of X-ray diffraction.

where m is an integer. By extending the idea of structure factors to the crystal, it can be represented by molecular structure factor summed over the entire crystal.

$$F^{crystal}(\mathbf{Q}) = \sum_{\mathbf{r}_j} F_j^{uc}(\mathbf{Q})e^{i\mathbf{Q}\mathbf{r}_j} \sum_{\mathbf{R}_n} e^{i\mathbf{Q}\mathbf{R}_n}. \qquad (2.12)$$

The first summation is the *unit cell structure factor* and the second one is the sum over the *lattice sites*. The product of scattering vector and the lattice spacing in the second sum leads to Bragg scattering only when the scattering vector is equal to reciprocal lattice vector (Laue condition).

2.2.5 Hexagonal Close-Packed Structure

Though not a Bravais lattice, *hexagonal close-packed* (hcp) structure ranks in important with the body-cantered cubic and face-cantered cubic Bravais lattices; about 30 elements crystallise in

57

the hcp form. Underlying the hcp structure is a simple *hexagonal* Bravais lattice, given by stacking two-dimensional triangular nest directly above each other. The direction of stacking is known as the *c*-axis.

There is an important relation between the lattice planes of the crystal and the reciprocal lattice vectors. The reciprocal lattice vector $\mathbf{G}_{hkl} = h\mathbf{b}_1 + k\mathbf{b}_2 + l\mathbf{b}_3$ is perpendicular to the lattice planes with Miller indices (hkl) and the distance d_{hkl} between two such adjacent planes is for a hexagonal lattice with lattice constants a and c is given by,

$$d_{hkl} = \frac{a}{\sqrt{\frac{4}{3}(h^2 + k^2 + hk) + \left(\frac{a}{c}\right)^2 l^2}}. \tag{2.13}$$

2.2.6 Estimation of lattice constants

Using the Bragg's law, the distance between the lattice planes can be evaluated. With the known lattice distances and the geometry of the crystal structure of the sample, we can estimate the lattice constants. However, there are many factors that could add a contribution to the error in the lattice constants. To minimize the systematic errors in the estimated lattice constant, the *Nelson-Riley* fit is utilised [187], which is given as,

$$F(\theta) = \frac{1}{2}\left(\frac{\cos^2(\theta)}{\theta} + \frac{\cos^2(\theta)}{\sin(\theta)}\right), \tag{2.14}$$

where the angles θ are the peak positions. With the plot of lattice constants as function of $F(\theta)$, the data points fits on a straight line and the intercept gives the lattice constant with reduced error.

2.2.7 Reflectivity and Refractivity

Because of the wave nature of the X-rays, it is natural to expect phenomena of refraction and reflection at the interface between

different media. To describe the refraction, the refractive index n of the media is defined as,

$$n = 1 - \delta + i\beta, \qquad (2.15)$$

where δ is of the order if 10^{-5} in solids and 10^{-8} in air. The imaginary part, β is usually smaller the δ. *Snell's law* related the incident angle α to the refracted angle α' as,

$$\cos\alpha = n\cos\alpha'. \qquad (2.16)$$

For an index of refraction less than *unity*, the X-ray incident at an angle called *critical angle α_c*, undergoes total external reflection. From Eq.2.15 and Eq.2.16, critical angle can be expressed as,

$$\alpha_c = \sqrt{2\delta}, \qquad (2.17)$$

and for simplicity, β is taken as zero. δ and β can be derived from scattering and absorption properties of the medium respectively.

Total external reflection have several important implications. It allows to construct focusing mirrors for the X-rays. At an angle close to critical angle, the wave propagates along the medium as evanescent wave. This increases the surface sensitivity with limited penetration depth. The second feature is exploited in the *grazing incidence X-ray diffraction (GIXRD)*.

2.2.8 Kiessig model

X-rays propagates in a medium depending on the optical properties of that particular medium. When propagates through different media, the X-rays get partly reflected and partly refracted due to difference in the refractive indices at the interface. Using the boundary conditions, Snell's law can be deduced as,

$$n_1\cos\alpha_1 = n_2\cos\alpha_2 \qquad (2.18)$$

where α_1 and α_2 are the angles between the propagation directions of the waves and the interface. With similar argument of boundary conditions, the Fresnel equations can be derived for reflectivity r and transmissivity t in terms of the wave vectors Q_1 and Q_2 in the two media:

$$r(Q_1) = \frac{Q_1 - Q_2}{Q_1 + Q_2}, \qquad t(Q_1) = \frac{2Q_1}{Q_1 + Q_2}. \qquad (2.19)$$
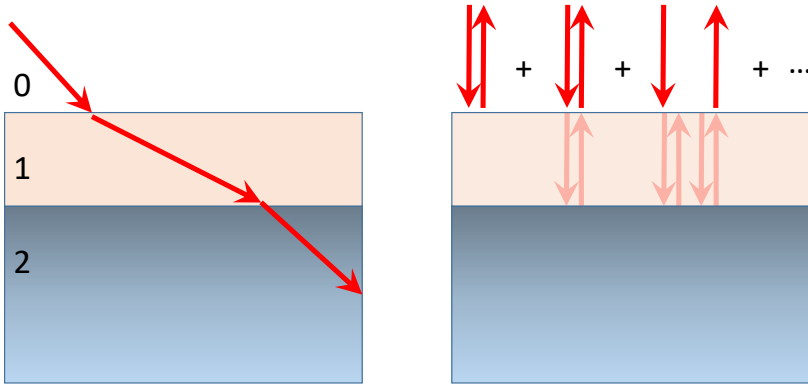

Figure 2.8: Illustration of Kiessig reflections between the thin film and the substrate.

We now use these relations to derive an expression for the reflectivity of X-rays from a thin slab of material. For this purpose, we assume same media (vacuum) on both sides of the slab. Such that $n_0 = n_2 = 1$ and reflectivities $r_{01} = -r_{12} = r$. At the interface part of the X-ray gets reflected and reaches the top boundary to repeat the reflection and refraction phenomena. The transmission contributes to the total reflected amplitude, but with a phase difference given by $p^2 = e^{(iQ_{slab}\Delta)}$. After multiple reflections, the X-ray emerges as a result of interference phenomena from the slab written as the geometric series,

$$r_{slab} = r - trtp^2 - trrrtp^4..... = \frac{r(1 - p^2)}{1 - r^2p^2}. \qquad (2.20)$$

When the intensity of the reflectivity is plotted, the intensity oscillates periodically depending on the thickness of the slab. These oscillations are known as *Kiessig* oscillations. Based on the periodicity, the thickness of the slab can be retro calculated. Even when the slab consists of multiple layers, the Kiessig formula treats the whole slab as one unit and hence fail to reproduce Bragg peak resulting due to the internal structure.

2.2.9   Parratt model

In the case of multilayers, Eq.2.20 can be used to calculate the reflectivity by means of the recursive algorithm introduced by Parratt [188]. By using the Kiessig formula multiple times to represent multiple reflections in between the multilayers of the slab results in reproduction of both the Kiessig oscillations as well as the Bragg peak.
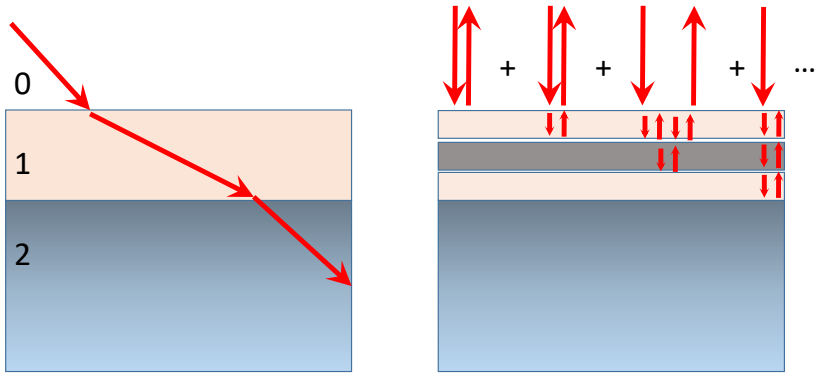
Figure 2.9: Illustration of Parratt recursion between the thin film and the substrate.

The recursive Parratt formula is given by,

$$R_{j-1,j} = \frac{r_{j-1,j} + R_{j,j+1}e^{id_jQ_j}}{1 + r_{j-1,j}R_{j,j+1}e^{id_jQ_j}}, \qquad (2.21)$$

where, $r_{j-1,j} = \frac{Q_{j-1}-Q_j}{Q_{j-1}+Q_j}e^{-\frac{1}{2}Q_{j-1}Q_j\sigma_j^2}$, and σ_j and d_j is the roughness and thickness of the jth layer, respectively. The equation is solved recursively from the bottom interface between WSe$_2$ and the substrate, as described in the main text. The reflectivity from the interface between bottom WSe$_2$ and the substrate is $R_{N,\infty} = \frac{Q_N-Q_{sub}}{Q_N-Q_{sub}}$, where, $Q_j = \sqrt{Q^2 - 8k^2\delta_j + i8k^2\beta_j}$, $\delta_j = 2\pi\rho_j r_e/k^2$, $\beta_j = \mu_j/2k$, $k = \frac{2\pi}{\lambda}$, is the magnitude of the wave vector of the incident X-rays, ρ is the electron density $e/^3$, $r_e(2.82\times10^{-5})$ is the Thomson scattering length, μ is the absorption coefficient $(^{-1})$, $Q = 2k\sin\alpha$ is the wave vector transfer for an incident angle α.

2.2.10 Domain size effects

It should be noted that the reflectivity depends only on the interface properties, and not on the crystallinity of the medium itself. In other words, an unordered layer characterized by well-defined sharp boundaries yields essentially the same reflectivity as a single-crystalline film. However, practical samples are not infinite, but finite in crystalline size. This manifests in the XRD by the means of broadening of the Bragg peaks. Utilizing this effects on Bragg peak, we can calculate average crystal size in the sample using *Debye-Scherrer* formula [189].

$$t = \frac{K\lambda}{B\cos\theta_B}, \tag{2.22}$$

where t is the thickness of the sample in the direction perpendicular to the scattering planes. K is dimensionless constant that depend on the geometry of the scattering object. B is the FWHM of the Bragg peak at an angle θ_B.

2.2.11 Grazing incidence XRD

Conventional XRD involves changing angle of incidence of the X-rays to investigate the internal structure of the material. In doing so the X-rays are made to penetrate deep into the material

with increasing angle of incidence. Such method works well if our
objective is to study the bulk materials. We used such techniques
to confirm the phase of grown WSe_2 thin films. This allowed us
to estimate the out-of-plane lattice constant of the grown WSe_2
thin films.

At ML limit the usual Bragg peak from the out-of-plane lattice
planes is missing. And this is not of our interest in the ML limit.
Our objective is to evaluate the in-plane lattice structure. For this
reason, we need to enhance the surface sensitivity of the X-rays
in order to obtain diffraction signal.
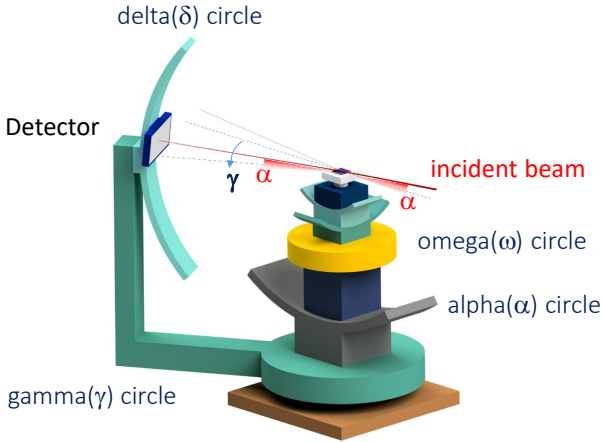
Figure 2.10: Illustration of six circle Eulerian cradle used at
ANKA, Karlsruhe; showing different angles that can be changed
independently.

This can be achieved by reducing the angle of incidence to just
above the critical angle. The X-rays undergoes total reflection
at angles below the critical angle. At critical angel, the X-rays
travel through the medium as an evanescent wave. As the X-
rays are limited to the surface, the diffraction is mainly due to
the surface crystal structure and unaffected by the bulk of the
material. This method is known as the grazing incidence X-ray
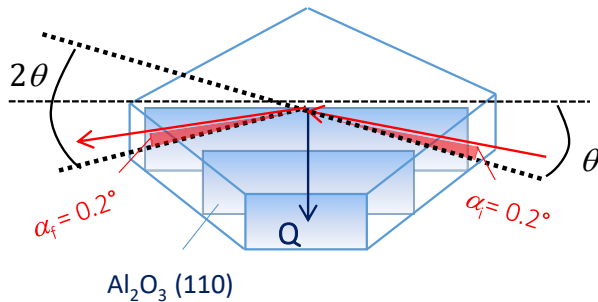
Figure 2.11: Illustration of GIXRD geometry on the substrate, in this case Al_2O_3 (012).

diffraction (GIXRD).

For the investigation of the in-plane crystal structure, we need to able to manipulate different angles of incidence and diffraction. This is achieved using Eulerian cradle with six degrees of freedom.

2.2.12 X-ray sources

MPI, Stuttgart

Our laboratory based XRD experiments were carried out on a custom built X-ray diffractometer. A common X-ray source is an X-ray tube. This consists of an electron source (cathode), which are directed towards a metallic target (anode). The bombardment of the anode with the electrons results in the emission of core electrons. These are filled by the valence electrons emitting X-rays in the process. Here we used Cu as the anode and the doublet is filtered to allow only the Cu k_α. Some of the key parameters of laboratory based X-ray source is summarised in the Tab.2.1.

Compared to the laboratory based X-ray diffractometers, the flux of the X-ray photon is magnitudes of orders larger, known

Energy	8.047 keV
Optics	Silicon Crystal monochromator,
Flux at the sample position	$6.7 \cdot 10^7$ ph/s
Beam size	0.8 mm (Hor) max
Experimental stage	Vertical four circle diffractometer
Detectors	Mythen 1D detector,
Software	SPEC

Table 2.1: Specifications of our laboratory based X-ray diffractometer
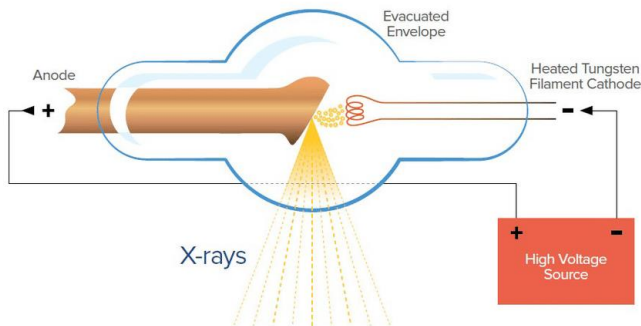
Figure 2.12: A typical X-ray source in the form of a vacuum tube with electron gun and metallic target as anode.

as *brilliance*. Such high brilliance facilitates characterisation of small samples in fraction of the time. In a synchrotron, electrons are injected into a circular orbit and maintained over the duration of the experiments. The circular orbits results in constant change in the acceleration of the electron giving out X-rays tangentially. The X-ray optics and experimental hutches are arranged in tangential directions along the circular orbit.

At a typical synchrotron, the electrons move in a circular ring called the storage ring. It consists of different components to keep
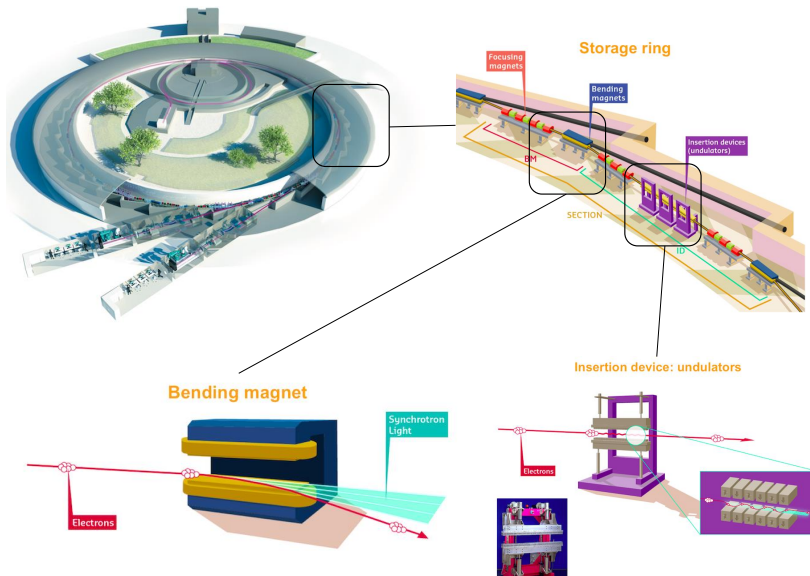
Figure 2.13: A typical layout of a synchrotron with different components. Copied from [190].

the electrons in a fixed orbit using magnets called the bending magnets. In addition the electrons are made to move in wavy path using small magnetic components called the insertion device or the undulators, which increases the intensity of the X-rays emitted. Some of the main optical elements are an Rh coated Si mirror and the double crystal monochromator (DCM). The DCM consists of a flat Si(111) single crystal and a sagittal Si(111) crystal bender for horizontal focusing. Two pairs of horizontal and vertical slits allow to pre-select the beam size on the sample.

MPI, ANKA, Karlsruhe

This beamline is optimized for structural characterization of materials in reduced dimensions like, surfaces, interfaces, thin films

Energy range	6keV to 20 keV
Optics	Double crystal monochromator with pair of Si(111) crystals, second crystal allows horizontal focusing of the beam and Rh coated mirror for vertical focusing
Energy resolution $(\Delta E/E)$	$3 \cdot 10^{-4}$ at 9 keV
Flux at the sample position	10^{12} ph/s
Beam size	0.5 mm (Hor) $\times$ 0.3 mm (Ver)
Experimental stage	Horizontal six circle diffractometer
Detectors	NaI scintillation counter, Mythen 1D detector and Pilatus 100k 2D detector
Software	SPEC

Table 2.2: Key specifications of MPI beamline at ANKA, Karlsruhe

and heterostructures. This facility can be used for the study of crystal truncation rod to investigate the surfaces and buried interfaces; scattering experiments at grazing angles to provide information at nanometre scale depths; specular or off-specular reflectivity measurements to evaluate surface and interface roughness; diffraction measurements to study the phase and structural properties of materials.

The essential component of this beamline is the **2+3 diffractometer**. It can be operated in both horizontal and vertical sample normal modes. Sample stage has four degrees of freedom in the vertical configuration, while horizontal configuration have five degrees of freedom. The detector arm has two degrees of freedom. The whole stage is aligned using theodolite.

I07, Diamond Light Source, Oxford

I07 is a high resolution X-ray diffraction beamline for the investigation of surfaces and interfaces at Diamond Light Source, Oxford. This beamline is optimized for grazing incidence small angle X-ray scattering, X-ray reflectivity and grazing incidence X-ray diffraction.

Energy range	6keV to 20 keV
Optics	Double crystal monochromator with pair of Si(111) crystals, and Kirkpatrick Baez focusing mirrors
Energy resolution ($\Delta E/E$)	$1 \cdot 10^{-4}$
Flux at the sample position	10^{14} ph/s at 10 keV
Beam size	0.1 mm (Ver) $\times$ 0.3 mm (Ver)
Experimental stage	Horizontal six circle diffractometer Hexapod
Detectors	Pilatus 100k 2D detector

Table 2.3: Specifications of I07 beamline at Diamond Light Source, Oxford

Samples can be mounted in either of the two mode; horizontal normal or vertical normal. In both geometries, the sample is mounted on a hexapod, which allows for six degrees of freedom. As in ANKA, different experiments can be performed to investigate the structural properties of the thin films. X-ray reflectivity is used to estimate the thickness of the sample and then moved to grazing incidence X-ray diffraction to evaluate the epitaxial strain in monolayer WSe_2 deposited on different substrates.

The synchrotron ring is circular, however, the electron move in non-circular orbit. It is shaped as forty eight sided polygon. The sudden change in the direction of the electron at the vertices results in exceptionally bright beam of electromagnetic radiation.

2.2.13 Method of measurement

Before starting the experiments, samples were fixed on STOE goniometer using silver paint. Thin layer of silver paint is preferred over double side adhesive tape to avoid misalignments or diffraction from the tape. Silver paint once dry, is reliable to withstand different temperatures or the argon flow at every angle. Great care is taken not to contaminate the film surface with silver or other chemical compounds. Samples were pressed gently with cotton swabs to be horizontally flat on the goniometer. This allows us to fix the sample coordinates with that of the X-ray source. Goniometer is then mounted on custom made stage with inlet and outlet for Ar gas and fitted with Kapton dome over the stage. Measurements were carried out in Ar atmosphere to avoid oxidation on the surface due to local heating at the sample surface. Kapton is used for its mechanical properties to withstand different temperatures and high transmission of X-rays and damage resistant due to radiation. Goniometer is used to allow fine adjustments in the angle to align with the coordinates of the X-ray source.

The stage with goniometer is then mounted on Eulerian cradle with six degrees of freedom. Such degree of freedom allows for measurement in different geometries. Sample is optically aligned using Theodolite to be horizontally flat and center of the X-ray beam. The closer the sample is to the laboratory coordinates, smaller will be the correction factors to the angles during the experiments. Then the alignment is continued using X-rays at a specular condition using NaI point detector. This is the most crucial part of the experiments. Before starting the experiments, the sample coordinates should match that of the source to avoid confusion down the line. Care must be taken not to damage the

detector with direct X-ray beam.

2.3 Band structure calculations

To better understand the electronic properties of the 2D TMDCs, we discuss the electronic band structure of one of the TMDC, ML WSe$_2$. To fully understand the band structure of WSe$_2$, it is useful to start with the description of the crystal field splitting of the d-orbitals of the transition metal. In free atoms and if we neglect spin-orbit coupling (SOC), the d-orbitals of the transition metal are degenerate. The degeneracy is lifted when six chalcogenide atoms surround the transition metal in octahedral coordination, into e_g and t_{2g} levels of d-orbitals. In the case of *trigonal prismatic* 1H-WSe$_2$ the degeneracy d-orbitals of W splits into three different sets of levels, $\{d_{z^2}\}$, $\{d_{xy}$ and $d_{x^2-y^2}\}$, and $\{d_{yz}$ and $d_{zx}\}$. At the $\mathbf{\Gamma}$ point, d_{z^2} is the lowest energy orbital, while d_{yz} and d_{zx} are the highest energy orbitals. However, at the $\mathbf{K}$ point, hybrid orbitals of d_{xy} and $d_{x^2-y^2}$ orbitals sandwich the d_{z^2} orbital. The energy level of the states in the electronic band structure depends on the orientation and degree of overlap between the neighbouring orbitals.

2.3.1 Tight binding model

Contrary to the free electron model where the electrons are represented by plane waves, we start with localized atomic orbitals as basis set to perform band structure calculations. When separated by a large distance, these orbitals are independent of each other's influence. However, as the distance between is reduced, they start to interact with each other and form bonding and anti-bonding states. The matrix elements of the interaction Hamiltonian is referred to as overlap parameters. As the atomic orbitals originating from many atoms reconstruct into bonding and anti-bonding states, the energy of such system evolve from the discrete atomic levels into continuous energy bands.
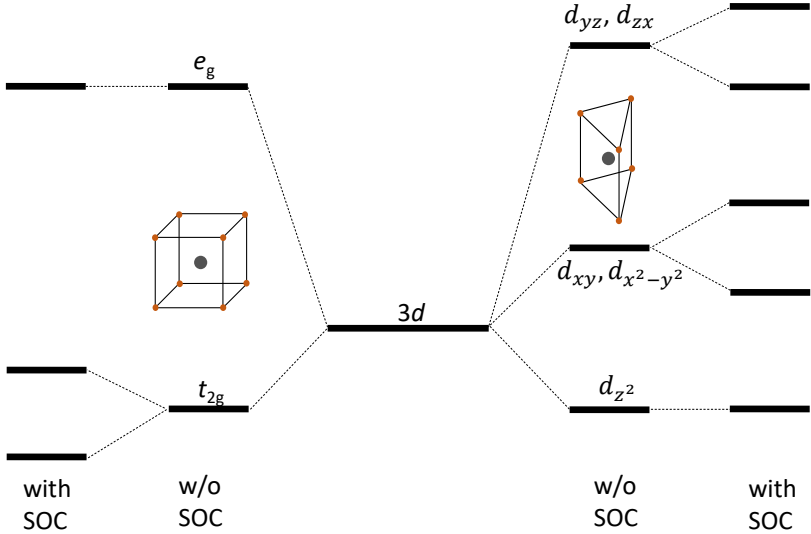
Figure 2.14: The crystal field splitting of the d-orbitals in cubic/octahedral and trigonal prismatic coordination of ligands around the transition metal atom with and without SOC.

The following is the discussion on the three band tight binding model as described by Liu et. al. [86]. Here the band structure of MX$_2$ (M = Mo, W; X = S, Se) is described using three orbitals which are responsible for the bands close to the Fermi level. These are d_{xy}, $d_{x^2-y^2}$ and d_{z^2}. As a first approximation, only the nearest neighbour interactions are included. This is reported to be sufficient to capture the band edge properties, while third nearest neighbour interactions are required to describe features for an entire Brillouin zone. Following their model, we first show the tight-binding result without the spin-orbit coupling, and later include it to describe the effect of SOC on the band structure. In order to calculate the band structure of ML WSe$_2$, we used the lattice parameters $a = b = 3.282$ Å and $c = 12.96$ Å as reported by Ref. [59].

Let the three orbitals near the Fermi level be denoted as $\left|\phi_\mu^j\right\rangle$.

Where, $(\mu = 1, ..l_j)$ in terms of μth basis belonging to j^{th} irreducible representation,

$$\left|\phi_1^1\right\rangle = d_{z^2}; \left|\phi_1^2\right\rangle = d_{xy}; \left|\phi_2^2\right\rangle = d_{x^2-y^2}. \qquad (2.23)$$

The matrix elements of the Hamiltonian H can be obtained as,

$$H_{\mu\mu'}^{jj'}(\mathbf{k}) = \sum_{\mathbf{R}} e^{i\mathbf{k}\cdot\mathbf{R}} E_{\mu\mu'}^{jj'}(\mathbf{R}), \qquad (2.24)$$

in which,

$$E_{\mu\mu'}^{jj'}(\mathbf{R}) = \left\langle \phi_\mu^j(\mathbf{r}) \left| H_0 \right| \phi_{\mu'}^{j'}(\mathbf{r} - \mathbf{R}) \right\rangle. \qquad (2.25)$$

The following is the Hamiltonian for the nearest neighbour d-d hopping after evaluating the matrix elements,

$$H_0(\mathbf{k}) = \begin{bmatrix} h_0 & h_1 & h_2 \\ h_1^* & h_{11} & h_{12} \\ h_2^* & h_{12*} & h_{22} \end{bmatrix}, \qquad (2.26)$$

where,

$$
\begin{aligned}
h_0 &= 2t_0(\cos 2\alpha + 2\cos\alpha\cos\beta) + \epsilon_1, \\
h_1 &= -2\sqrt{3}\sin\alpha\sin\beta + 2it_1(\sin 2\alpha + \sin\alpha\cos\beta), \\
h_2 &= 2t_2(\cos 2\alpha - 2\cos\alpha\cos\beta) + 2\sqrt{3}it_1\cos\alpha\cos\beta, \\
h_{11} &= 2t_{11}\cos 2\alpha + (t_{11} + 3t_{22})\cos\alpha\cos\beta + \epsilon_2, \\
h_{22} &= 2t_{22}\cos 2\alpha + (3t_{11} + t_{22})\cos\alpha\cos\beta + \epsilon_2, \\
h_{12} &= \sqrt{3}(t_{22} - t_{11})\sin\alpha\sin\beta + 4it_{12}\sin\alpha(\cos\alpha\breve{~}\cos\beta), \\
\text{for,}(\alpha, \beta) &= \left(\frac{1}{2}k_x a, \frac{\sqrt{3}}{2}k_y a\right),
\end{aligned}
$$

$$(2.27)$$

where ϵ_j is the on-site energy corresponding to the atomic orbitals $\left|\phi_\mu^j\right\rangle$. The fitting parameters were estimated with the use of first-principles calculated band structure of relaxed ML MX_2. This is

not to fit the entire Brillouin zone, but only to fit the feature at the high symmetry points of $\mathbf{\Gamma}$, $\mathbf{K}$ and $\mathbf{M}$. Including third nearest neighbour interactions, the band structure over entire Brillouin zone is reproduced.
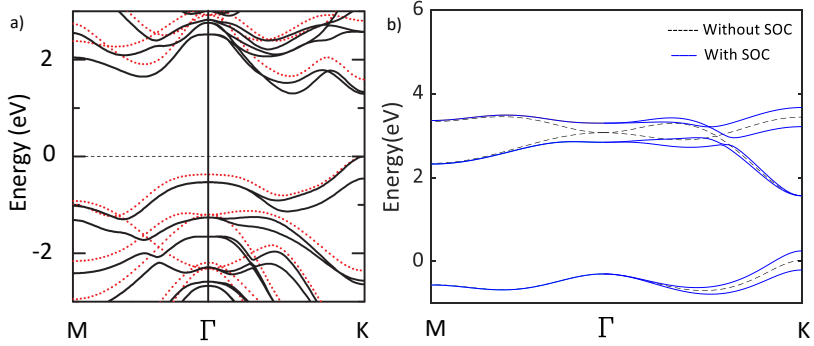
Figure 2.15: Band structure of monolayer 1H-WSe$_2$. a) In red is the band dispersion without spin-orbit coupling and with spin-orbit coupling in black calculated using DFT from Ref. [26]. b) Tight binding simulation with nearest neighbour interactions, as described by Ref. [86].

Due to the heavy transition metal, W, the influence of spin-orbit coupling could be large. Large SOC together with the broken inversion symmetry of ML WSe$_2$ results in large spin splitting as will be shown below. The SOC is included as simple approximation of $\mathbf{L} \cdot \mathbf{S}$ term for the transition metal, W. $\mathbf{L} \cdot \mathbf{S}$ terms are calculated using the following orbitals as the basis; $|d_{z^2}, \uparrow\rangle$, $|d_{xy}, \uparrow\rangle$, $\left|d_{x^2-y^2}, \uparrow\right\rangle$, $|d_{z^2}, \downarrow\rangle$, $|d_{xy}, \downarrow\rangle$, $\left|d_{x^2-y^2}, \downarrow\right\rangle$. The Hamiltonian to add SOC is

$$H_{SOC} = \lambda \mathbf{L} \cdot \mathbf{S} = \frac{\lambda}{2} \begin{bmatrix} L_z & 0 \\ 0 & L_z \end{bmatrix}, \tag{2.28}$$

73

where,

$$L_z = \begin{bmatrix} 0 & 0 & 0 \\ 0 & 0 & 2i \\ 0 & -2i & 0 \end{bmatrix}, \qquad (2.29)$$

is the z component of the orbital angular momentum and λ reflects the strength of the SOC. For the bases used, the matrix elements of $\hat{L}_x$ and $\hat{L}_y$ are zero. Here we can define the total Hamiltonian with SOC as;

$$H(\mathbf{k}) = H_0(\mathbf{k}) + H_{SOC} = \begin{bmatrix} H_0(\mathbf{k}) + \frac{\lambda}{2}L_z & 0 \\ 0 & H_0(\mathbf{k}) - \frac{\lambda}{2}L_z \end{bmatrix}. \qquad (2.30)$$

At the $\mathbf{K}$ point in the Brillouin zone, the conduction band is still degenerate, whereas the valance band splits by $\Delta_{SOC}^v = 2\lambda$. Although this nearest neighbour model is not as accurate as third nearest neighbour model, it still gives results for low energy physics at the Fermi level. Xiao et. al. [97], estimated the Berry curvatures and spin Berry curvatures at $\pm\,\mathbf{K}$ points of the Brillouin zone. Former has opposite sign at $+\mathbf{K}$ and $-\mathbf{K}$, while the latter is the same at both points. Three band tight binding model with nearest neighbour interactions is sufficient to obtain qualitative information at the $\mathbf{K}$ points.

2.3.2 First principles calculations

Tight binding model gives decent qualitative description of the bands near the Fermi level as discussed above. In order to simulate the electronic band structure for the real system of ML WSe_2, it is fruitful to use the first-principles (FP) calculations. We use the real positions of the atoms as given in ICSD, which allows us to calculate the complete band structure including the core levels. The information of the position of atoms is used to simulate the nature of the atomic orbitals overlapping with each other. In order to simulate the ML limit, the interlayer interactions are

suppressed by including large vacuum between the layers. In this thesis, we used 30 Å of vacuum in between the monolayers.

Solving the Schrödinger equation for such many body systems is not practical and hence approximations are needed to breakdown the complicated problem into solvable bits. Using the single particle approximation, many body problem can be solved using functional, in this case, the spatially dependent electron density. The next hurdle is to find the exchange and correlation functional, which are known only in the case of free electron gas. To overcome this, local density approximation (LDA) is used, as functional of electron density only at the coordinates of the calculations. And the extension of this is the generalised gradient approximation (GGA), which includes the gradient of the electron density at the same coordinate. In detail theoretical background can be found in Ref. [191].

We used the linearized augmented plane wave (LAPW) method which provides an accurate simulation of the electronic structure of crystalline solids in the framework of density functional theory. The system of electrons is treated as an electron gas to calculate its ground state using local density approximation. The main parameters are the spin densities $\rho_\sigma(r)$ which comes into the total energy equation as,

$$E_{tot}(\rho_\uparrow, \rho_\downarrow) = T_s(\rho_\uparrow, \rho_\downarrow) + E_{ee}(\rho_\uparrow, \rho_\downarrow) + E_{Ne}(\rho_\uparrow, \rho_\downarrow) + E_{xc}(\rho_\uparrow, \rho_\downarrow) + E_{NN},$$
$$(2.31)$$

where E_{NN} is the repulsive Coulomb energy of the fixed nuclei and the electronic contributions are from the kinetic energy, electron-electron repulsion, nuclear-electron attraction and exchange-correlation. Exchange-correlation has no classical counterpart and its origin is purely quantum mechanical,

$$E_{xc} = \int \mu_{xc}(\rho_\uparrow, \rho_\downarrow)(\rho_\uparrow + \rho_\downarrow)dr. \qquad (2.32)$$

The exchange-correlation energy E_{xc} is used as the exchange-correlation density μ_{xc} times the total electron density. Recent

progress is made by adding the gradient terms of the electron density to the exchange-correlation energy or its corresponding potential. This led to the generalised gradient approximation (GGA) with parameterisations, e.g. PW91 or PBE [192]. There are different forms of μ_{xc} and the one used in this thesis is the one given by Ceperley and Alder by Perdew and Wang [193]. E_{tot} can be minimised using orbitals χ_{ik}^{σ} constrained to construct the spin densities in a periodic systems as,

$$\rho_\sigma(r) = \sum_{i,k} \rho_{ik}^\sigma \left|\chi_{ik}^\sigma(r)\right|^2 . \tag{2.33}$$

Here ρ_{ik}^σ is the occupation number such that $0 \leq \rho_{ik}^\sigma \leq 1/w_k$, where w_k is the symmetry required weight of the point k [191]. Then the variation of E with respect to the density leads to the Kohn-Sham equation,

$$\left[-\nabla^2 + V_{Ne} + V_{ee} + V_{xc}^\sigma\right] \chi_{ik}^\sigma(r) = \epsilon_{ik}^\sigma(r)\chi_{ik}^\sigma(r), \tag{2.34}$$

which must be solved self-consistently in an iterative process. Finding the Kohn-Sham orbitals require the knowledge of the potentials which themselves depend on the spin density and thus on the orbitals.

LAPW method is procedure that simplifies the Kohn-Sham equations as linear optimisation problem for the evaluation ground state density, total energy and the eigenvalues of the many electron systems with a basis set which is adapted to the problem. The adaptation is done by dividing the unit cell into the non-overlapping atomic spheres and the interstitial region. In the atomic spheres, the basis set is the linear combination of the radial functions times spherical harmonics $Y_{lm}(r)$ as,

$$\phi_{\mathbf{k}_n} = \sum_{lm} \left[A_{lm,\mathbf{k}_n} u_l(r, E_l) + B_{lm,\mathbf{k}_n} \frac{d}{dE_l} u_l(r, E_l)\right] Y_{lm}(\hat{\mathbf{r}}), \tag{2.35}$$

where $u_l(r, E_l)$ is the regular solution of the radial Schrödinger equation for energy E_l and the spherical part of the potential inside sphere; $\frac{d}{dE_l} u_l(r, E_l)$ is the energy derivative of u_l evaluated at the same energy E_l. A linear combination of these two functions constitute the linearization of the radial function; the coefficients A_{lm} and B_{lm} are functions of k_n determined by requiring that this basis function matches each plane wave (PW) the corresponding basis function of the interstitial region; u_l and $\frac{d}{dE_l} u_l$ are obtained by numerical integration of the radial Schrodinger equation on a radial mesh inside the sphere [191].

Whereas in the interstitial region a plane wave expansion is used

$$\phi_{\mathbf{k}_n} = \frac{1}{\sqrt{\omega}} e^{i\mathbf{k}_n \cdot \mathbf{r}}. \tag{2.36}$$

The solutions of the Kohn-Sham equations are expanded as the combined basis set of LAPW's according to the linear variation method

$$\psi_{\mathbf{k}} = \sum_n c_n \phi_{\mathbf{k}_n}, \tag{2.37}$$

and the coefficients c_n are determined by the Rayleigh-Ritz variational principle. The convergence of this basis set is controlled by the cut-off parameter which is usually the user defined [191].

In the present thesis, the DFT calculations were performed on ML WSe_2 in which the tensile and compressive strains are incorporated into the calculation by varying the *in-plane* lattice parameter in the steps of 1%. The total volume of the unit cell is maintained as a constant and hence the variation in the *out-of-plane* lattice constant is included. The representative band structure is shown in the Fig.2.16 with spin splitting of 0.45 eV and band gap of 1.42 eV.
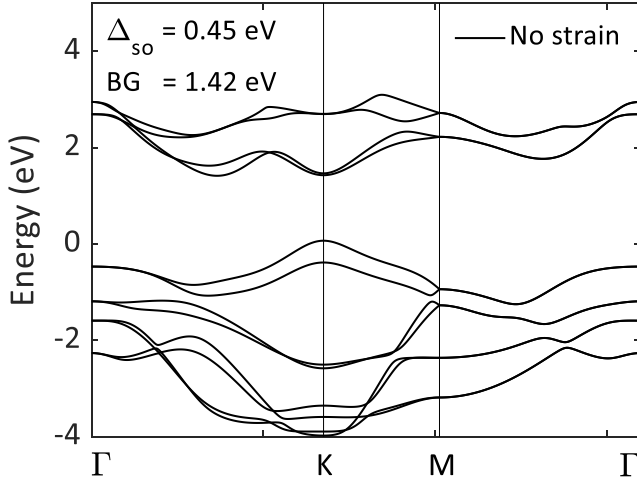
Figure 2.16: Representative band structure calculated for un-strained (Δa=0%) ML WSe$_2$.

2.4 Angle resolved photoelectron spectroscopy (ARPES)

The theoretically calculated electronic band structure of the ML WSe$_2$ can be mapped experimentally using photoelectron spectroscopy. Photoelectron spectroscopy, also known as photoemission spectroscopy, refers to energy measurement of electrons emitted from solid, liquid or gaseous sample using photoelectric effect. This is broad term which includes different techniques depending on the type of radiation as, X-ray or ultraviolet. There are three major types of photoemission spectroscopy. They are,

1. X-ray photoelectron spectroscopy (XPS): Used to study the energy levels of atomic core levels in solids. This technique is also referred as 'electron spectroscopy for chemical analysis (ESCA)', because the core levels have small chemical shifts depending of the chemical environment of the atom of interest. XPS spectra are obtained by irradiating the

78

sample with X-ray while measuring the kinetic energy and the number of electrons that are emitted from the sample.

2. Ultraviolet photoelectron spectroscopy (UPS): Used to study valance energy levels and the chemical bonding. The kinetic energy of the emitted electrons through absorption of ultraviolet light is measured to determine the chemical nature in the valence region.

3. Two-photon photoelectron spectroscopy (2PPE): Advance technique used to optically excite electronic states through pump and probe method. This is time resolved spectroscopy used to study the electronic excitation at the surfaces. It uses picosecond or femtosecond laser pulses in order to photo excite the electrons. After time delay, the excited electron is photo excited electron is photo emitted into a free electron by the second pulse. The kinetic energy and the angle of emission of the photoelectron are measured by an electron analyser.
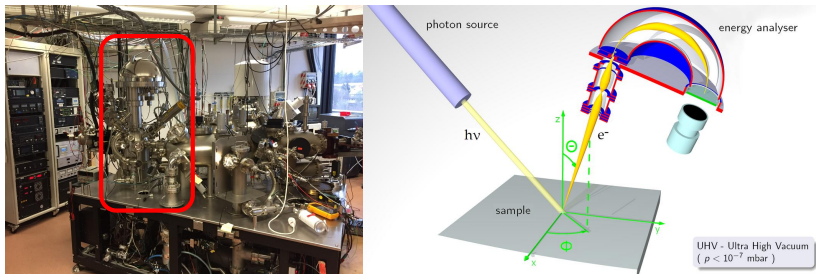
Figure 2.17: Our laboratory based ARPES instrument and the working principle of the semi hemispherical analyser marked in red.

These are some of the most important experimental methods to understand the electronic state of the given material. Depending on the energy, angles involved and polarisation provides information of all occupied states. A much more sophisticated tech-

nique is angle resolved photoemission spectroscopy (ARPES). It used to observe the distribution of the electrons in the reciprocal space of the solids. It is the most direct method to visualize the electronic band structure at the surface of solids. Since both direction and energy of the electrons are measured, the energy and momentum of the valance electron can be estimated resulting in detailed information on band dispersion and the Fermi surface.

Laboratory based sources are the sharp spectral lines of helium at photon energies of 21.22 eV (HeI) and 40.82 eV (HeII). The laboratory based sources are eventually replaced by synchrotron sources, which has very high photon flux and flexibility to change energy from few eV to several keV. Polarisation offers another possibility to study the symmetry of the electron orbitals involved.

Photoelectron spectroscopy can be described in three steps. Absorption of the radiation by the material and resulting photoexcitation of the electron from an occupied state into an unoccupied state, transport of the electron to the surface and crossing the potential barrier at the surface. The later process results in the loss of information regarding the perpendicular component of the electron momentum. Photoemission spectroscopy is highly surface sensitive due to the fact that the mean free path of the electrons is few Å depending on the energy.

During a typical PE experiment, the sample mounted on goniometer is irradiated with monochromatic radiation of energy $h\nu$ and the excited photoelectrons are collected by the electron energy analyser, which measures the kinetic energy and the direction of the electrons. The conservation of energy directly relates the kinetic energy E_{kin} of the photoelectron to the photon energy $h\nu$:

$$E_{kin} = h\nu - E_B - \Phi, \qquad (2.38)$$

where E_B is the binding energy and Φ is the work function of the sample. The kinetic energy E_{kin} is usually measured from the Fermi level E_F of the sample. Technically, the binding energy is

the difference between the total energy of the initial state with N electron and the final state with N-1 electrons.

$$E_B = E^{N-1} - E^N. \tag{2.39}$$

It is not easy to measure the absolute energies of the initial states. Since the state with N electron changes to N-1 electron state, the final system includes the photo hole created by the emission of the electron. This photo hole changes the potential of N-1 electron state. Hence the binding energy E_B is modified as:

$$E_B = h\nu^{\smile} E_{kin} - \Phi - \Delta E_{relax}. \tag{2.40}$$

In reality the delocalized electrons screen the effect of photo hole and the relaxation energy is negligible when mapping the valance states. This is not the case when the core level are to be mapped. And the relaxation energy is to be accounted for when dealing with core levels.

Photon momentum is negligible compared to the momentum of the electrons. In crystalline material the translational symmetry requires the conservation of the electron momentum in the plane of the sample.

$$\hbar k_{i||} = \hbar k_{||} = \sqrt{2mE}\sin\theta. \tag{2.41}$$

Here, $\hbar k$ is the momentum of the emitted electron and $\hbar k_i$ is the initial momentum of the electrons. The non-conservation of the normal component of the electron can be treated by assuming the final crystal states are free electron like.

$$k_{i\perp} = \frac{1}{\hbar}\sqrt{2m(E\cos^2\theta + V_0)}, \tag{2.42}$$

where V_0 is the band depth from the vacuum, including electron work function ϕ. V_0 can be estimated by measuring the kinetic energy of the emitted electrons normal to the surface as a function of the incident photon energy. The dispersion relation between

the binding energy and the wave vector can be determined by solving the equations for the energy and momentum.

2.5 Electronic transport

2.5.1 Drude model

After the discovery of the electron, Paul Drude used the kinetic theory of gases to explain the electrical conductivity of the metals. For this, the following assumptions were made. First, that there is not interactions between electrons and positive ionic cores. Second the collisions are instantaneous, which means that the kinetic energy and hence the momentum is abruptly changes at collisions. Third that the electrons move in straight path in the absence of external electromagnetic fields, whereas the dynamics of electrons in external fields is governed by classical Newton's law of motion. Fourth, the mean free path of the electron is the distance travelled by the electron between collisions, and the reciprocal gives the relaxation time. And finally, that the electrons reach thermal equilibrium with surroundings by collisions.

Ohm's law states the proportionality of the current I flowing in a metal to the potential drop V across the metal. The proportionality constant is the resistance of the metal R, which depends on the dimensions of the metal bar in this case.

$$V = IR. \tag{2.43}$$

The dimensions of the metal bar can be ignored by introducing the resistivity ρ, which is material constant. ρ is the proportionality constant between the electric field $\mathbf{E}$ applied across the metal bar and the current density $\mathbf{J}$. The current density $\mathbf{J}$ is the amount of charge flowing per unit time per unit area perpendicular to the flow of current.

$$\mathbf{E} = \rho\mathbf{J}. \tag{2.44}$$

If n electrons of charge e moves with velocity $\mathbf{v}$, then the current density $\mathbf{J}$ is given by $\mathbf{J} = -ne\mathbf{v}$. For the electrons moving in the presence of an external electric field $\mathbf{E}$, the from the Newton's equation of motion,

$$\mathbf{F} = \frac{m\mathbf{v}}{\tau} = -e\mathbf{E} \implies \mathbf{v} = -\frac{e\mathbf{E}\tau}{m}; \quad \mathbf{J} = \left(\frac{ne^2\tau}{m}\right)\mathbf{E}. \quad (2.45)$$

This leads to the definition of conductivity, which is the inverse of the resistivity and the proportionality factor between the current density and the applied electric field as,

$$\mathbf{J} = \sigma\mathbf{E}; \quad \sigma = \frac{ne^2\tau}{m}; \quad \mu = \frac{e\tau}{m}. \quad (2.46)$$

Here μ is the mobility of the electrons. Using similar argument, the Newton's equation of motion can be used in the presence of impurities or defect and external field.

$$\frac{d\mathbf{P}}{dt} = \mathbf{f}(t) - \frac{\mathbf{P}}{\tau}. \quad (2.47)$$

This implies that the effect of individual electron collisions introduce a frictional damping term into the equation of motion for the momentum per electron.

2.5.2 Hall effect

Hall measurement is one of the basic methods used to characterise the electronic materials. This method allows for direct estimation of charrier density and the mobility. Generally, a slab of material is placed in a magnetic field and current passed across the slab. The electrons accelerate ($\mathbf{F} = q\mathbf{E}$) due to the electric field $\mathbf{E}$ and deflect because of the Lorentz force ($\mathbf{F} = q[\mathbf{v} \times \mathbf{B}]$) due to the magnetic field $\mathbf{B}$. If the electron moves with a drift velocity $\mathbf{v}_d$ and the relaxation time; that is the time between the collisions,

is τ, then we can write the equation of motion of electrons as following,

$$\frac{m\mathbf{v}_d}{\tau} = e[\mathbf{E} + \mathbf{v}_d \times \mathbf{B}]. \tag{2.48}$$

Rewriting this for the equation of motion in xy plane as,

$$\left[\begin{array}{cc} m/e\tau & -B \\ +B & m/e\tau \end{array} \right] \left[\begin{array}{c} v_x \\ v_y \end{array} \right] = \left[\begin{array}{c} E_x \\ E_y \end{array} \right].$$

Using the relation (3.41), $\mathbf{J}=en\mathbf{v}$;

$$\left[\begin{array}{cc} m/e\tau & -B \\ +B & m/e\tau \end{array} \right] \left[\begin{array}{c} J_x/en \\ J_y/en \end{array} \right] = \left[\begin{array}{c} E_x \\ E_y \end{array} \right],$$

such that,

$$\left[\begin{array}{c} E_x \\ E_y \end{array} \right] = \sigma^{-1} \left[\begin{array}{cc} 1 & -\mu B \\ +\mu B & 1 \end{array} \right] \left[\begin{array}{c} J_x \\ J_y \end{array} \right],$$

where $\sigma = en\mu$ and $\mu = e\tau/m$. Rewriting in terms of resistivity tensor;

$$\rho_{xx} = \sigma^{-1}, and \quad \rho_{yx} = -\rho_{xy} = (\mu B)/\sigma = B/en. \tag{2.49}$$

$$\left[\begin{array}{c} E_x \\ E_y \end{array} \right] = \left[\begin{array}{cc} \rho_{xx} & \rho_{xy} \\ \rho_{yx} & \rho_{yy} \end{array} \right] \left[\begin{array}{c} J_x \\ J_y \end{array} \right].$$

This suggests that the longitudinal resistance is constant, whereas the transverse or the Hall resistance increases linearly with magnetic field $\mathbf{B}$. Practically, the rectangular slab is used for such an experiment, where the current flows in the x-axis, magnetic field is applied perpendicular to the slab in the z-axis to observe Hall voltage and hence the Hall resistance in the y-axis.

$$E_x = \rho_{xx} J_x; \quad E_y = \rho_{yx} J_x. \tag{2.50}$$

where $I = J_x W, V_x = E_x L$ with W being the width of the sample and L being the length, and $V_H = E_y W$. Using these relations, we get,

$$\rho_{xx} = \frac{V_x}{I}\frac{W}{L}, and \quad \rho_{yx} = \frac{V_H}{I}. \qquad (2.51)$$

Using the Eq.3.45, we the expressions for the carrier density n,

$$n = \left[e\frac{d\rho_{yx}}{dB}\right]^{-1}, \qquad (2.52)$$

and the mobility μ of the carriers,

$$\mu = \frac{1}{en\rho_{xx}}. \qquad (2.53)$$

Depending on the sign of the Eq.2.52, the type of carrier, i.e., if electrons or holes can be interpreted. There are two widely used geometries. One is the van der Pauw geometry which has only 4 contacts and the other of 5 contacts in the Hall bar geometry. We have used van der Pauw geometry with $W=L$ for simplicity.

2.5.3 Quantum mechanical model

Although classical picture gives satisfactory explanation of the electronic properties in macroscopic scale, quantum effects starts to get prominent in the mesoscopic/microscopic description of the electronic transport in materials.

According to quantum mechanics, the particles behaves as if it is a wave and satisfy Schrödinger equation. Schrödinger equation is analogue of wave equation for matter. Schrödinger equation gives the evolution of matter wave described by a wave function $\Psi(\mathbf{r}, t)$. The Schrödinger equation for one dimensional wave function $\Psi(x, t)$ can be written as,

$$-\frac{\hbar^2}{2m}\frac{\partial^2}{\partial x^2}\Psi(x,t) + V(x)\Psi(x,t) = i\hbar\frac{\partial}{\partial t}\Psi(x,t), \qquad (2.54)$$

which describes the evolution of the wave function in a potential $V(x)$. The wave function can be decoupled into spatial and temporal parts. For a free particle, i.e., in the absence of potential, the time independent Schrödinger equation simplifies to,

$$-\frac{\hbar^2}{2m}\frac{\partial^2}{\partial x^2}\psi(x,t) = E\psi(x). \qquad (2.55)$$

The solutions of this equation is plane waves, $\psi(x) = exp(\pm ikx)$, which leads to the energy states of the particle as a function of the wavenumber k. Classically, this is a situation with pure kinetic energy and no potential energy for the particle.

$$E(k) = \frac{\hbar^2 k^2}{2m}. \qquad (2.56)$$

This fact can be used to deduce the momentum p as $p = \hbar k$. Using the relation between the energy and frequency yields, the following two relations that are central to the basic quantum mechanics, as quantisation of energy and momentum.

$$E = \hbar\omega = h\nu, and \quad p = \hbar k = \frac{h}{\lambda}. \qquad (2.57)$$

It is possible to confine the particle in a region by manipulating the potentials. The simplest of these cases is the confinement of the particle in one dimensional potential well. The potential at the edges is infinite that the particle cannot escape and there is no potential in the well, and hence behave like a free particle. This leads the quantisation of the energy levels, in which the particle can be with corresponding wave function. This is known as a 'Quantum Well'. Similar configurations can be created in two and three dimensions.

The situation is quite different in the case of the electron in a periodic lattice of materials. The potentials for the particle are periodic and the wave functions that satisfy such a configuration are called Bloch wave functions. This gives rise to a series of energy states that combine to form a band for energy as a function of momentum wavenumber.

There are two major regions in the band structure of materials. They are the valance band and the conduction band. The level up to which the electrons can occupy the energy state at absolute zero is called the Fermi level. Since the electrons are Fermions, they obey the Fermi-Dirac distribution. At higher temperatures the electrons start to populate the levels higher than the Fermi level. Depending where this Fermi level is located, the materials are classified as electronic conductors, insulators and semiconducting. The method to calculate the band structure of materials is discussed on the introduction.

As we are treating the electrons as waves, it is natural to introduce few characteristic lengths. These lengths create a reference with respect to which the dimensions of the electronic conductivity is treated. For example, if the dimensions of the conductor is much larger than the characteristic lengths, then the conductor shows Ohmic character. These lengths are, the de Broglie wavelength, the mean free path and the phase relaxation length. As the Fermi wavenumber increases with the square root of the electron density, the corresponding wavelength decreases as the square root of the electron density.

$$\lambda_F = 2\pi/k_f = \sqrt{2\pi/n_s}. \tag{2.58}$$

The mean free path is the distance the electron moves in the material before the initial momentum is destroyed. This is very large in pure crystalline material. However in reality, the defects, impurities and the phonon vibrations affect the path of the electron. Hence, the momentum relaxation time is related to the collision time. For an electron with Fermi velocity v_F and momentum relaxation time τ_m, the mean free path is given by,

$$L_m = v_F \tau_m. \tag{2.59}$$

To understand the concept of phase relaxation length, the following thought experiment is needed. Suppose the electron moves in a material from point A to point B in two different arms of the circular loop. Since the length of the arms are equal, the phase

acquired by the electron in both arms is equal and interfere con-
structively. Suppose a magnetic field is applied perpendicular to
the plane of the arms, the phase of the electron can be manipu-
lated relative to each other. This can lead to cycles of constructive
and destructive interferences. In reality once again, the electron
can scatter from the impurities in the arms which could change
the relative phase of the electron between the arms. However, if
the scatters are rigid, the relative phase is constant. The situation
changes drastically, when the scatters are randomly fluctuating.

$$L_\phi = v_F \tau_\phi. \tag{2.60}$$

The phase relaxation length can be related to the relaxation
time with Fermi velocity as the proportionality constant. This is
the case when the phase relaxation length is of the same order or
smaller than the momentum relaxation time. It is the case with
the high mobility semiconductors. In the case of low mobility
semiconductors, the momentum relaxation time is much shorter
than the phase relaxation time. This leads to random scatter-
ing of the electrons and the motion of electron is not ballistic
any more, but diffusive. The root mean square of the distance
travelled by the electron can be found by summing the square of
lengths in random direction trajectories. Hence,

$$L_\phi^2 = v_F^2 \tau_m \tau_\phi / 2. \tag{2.61}$$

Or in other words,

$$L_\phi^2 = D\tau_\phi, \tag{2.62}$$

where $D = v_F^2 \tau_m / 2$ is the diffusion coefficient.

2.6 Miscellaneous techniques

2.6.1 Electron diffraction

Electron diffraction is one of the standard methods to investigate
the structure of thin films. It can be used to obtain the crystal-

lographic information as well as the surface atomic structure. As
in every diffraction methods, the crystallographic nature can be
obtained by the periodicity of the diffraction pattern and hence
the symmetry, and the relative intensities provide information on
the atomic position in the crystal structure. The LEED is mostly
used to investigate clean and crystalline surfaces. The intensity
of the current used could be damaging to study the adsorbents
on the surface of the samples.

Standard LEED consists of electron gun and the suitable
screen to capture the Bragg spots. The wavelength of the electron
beam with voltage V applied, can be estimated with the following
expression.

$$\lambda = \frac{h}{p} = \frac{h}{\sqrt{2meV}} = \sqrt{\frac{150.412}{V}}[].\qquad(2.63)$$
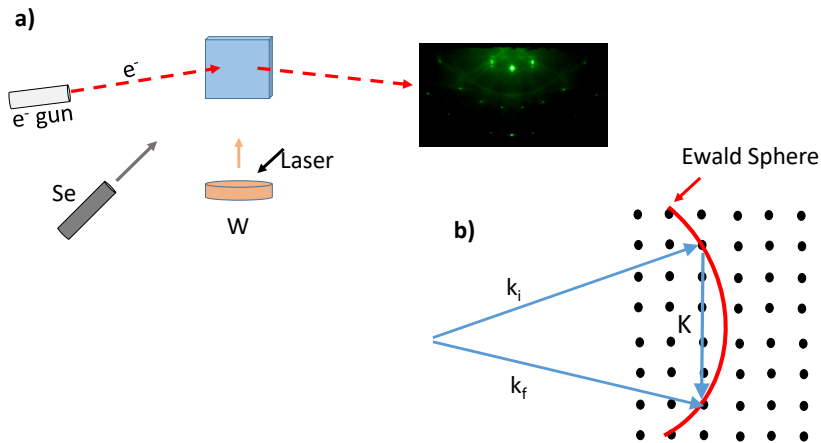
Figure 2.18: a) Illustration of RHEED. b) Illustration of the
Laue's condition.

An electron beam with 10 keV of energy corresponds to wave-
length of 0.123 Å. This is on the scale of interatomic lattice dis-
tance and hence diffract from the atoms. Similar to the diffrac-

tion of the X-rays, the electron diffraction produces a diffraction patter at specific angles.

In addition we have used RHEED for qualitative in-situ characterization of WSe$_2$ thin films. RHEED is an electron diffraction method, in which a beam of electron incident on the sample in shallow angle. This makes this method a highly surface sensitive. There are three main components in a RHEED setup; first the electron source, then electric grid to control the beam of electrons and finally, the fluorescent screen.

The diffraction patterns are different among them. This is due to the geometry of the experiment. In the case of LEED, the diffraction is perpendicular to the sample surface providing two dimensional crystallographic information. RHEED on the other hand, has completely different geometry. The electron beam glances from the sample surface in very low angle. The diffraction pattern is observed when the diffracted electron beam cuts the Ewald sphere. The so called reciprocal lattice rods of the diffracted beam could be smeared out due to spread in the energy of the electron beam.

When the angle of incidence is increased, the diffracted lattice rods due to flat surface gradually change into diffraction spots due to increased depth of penetration of the electron beam into the sample. This particular property can be exploited in monitoring the crystal growth of the material in-situ during the thin film deposition.

2.6.2   Atomic force microscopy

AFM is useful for three-dimensional topographic information surfaces with lateral resolution down to 1.5 nm and vertical resolution down to 0.05 nm. These samples can include clusters of atoms and molecules, individual macromolecules, or biological species. This technique needs minimal sample preparation and can be operated in gas, ambient, and fluid environments and can measure physical properties including elasticity, adhesion, hardness, friction and chemical functionality.
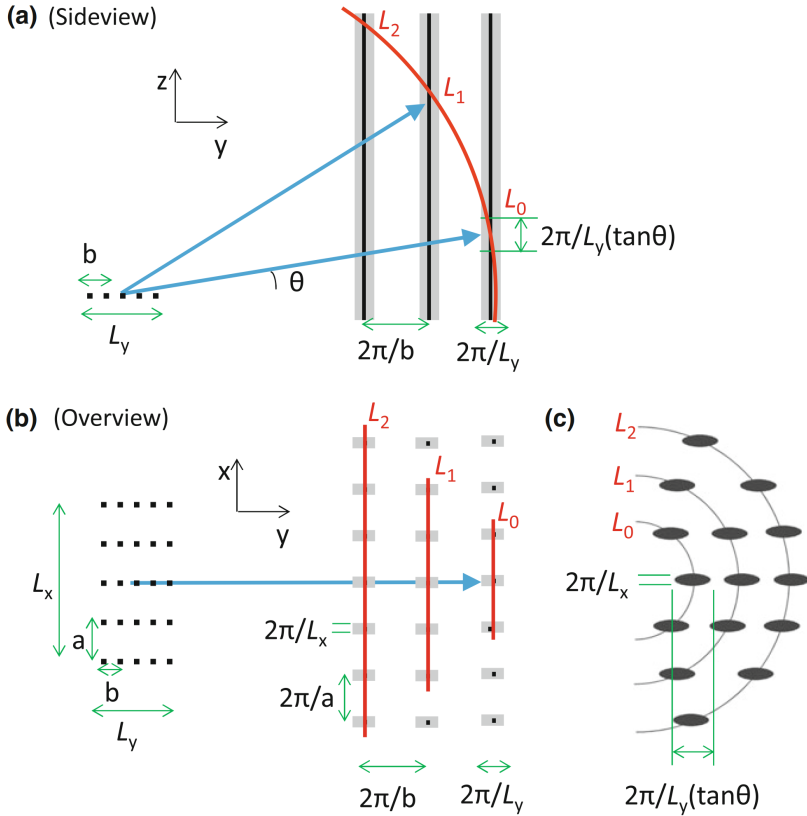
Figure 2.19: a) Illustration of origin of RHEED streaks. b) Illustration of the RHEED spots. [194]

The choice for which AFM mode to use is based on the surface characteristics of interest and on the hardness/stickiness of the sample. Contact mode is most useful for hard surfaces; a tip in contact with a surface, however, is subject to contamination from removable material on the surface. Excessive force in contact mode can also damage the surface or blunt the probe tip. Tapping mode is well-suited for imaging soft biological specimen and for samples with poor surface adhesion. Non-contact mode is

another useful mode for imaging soft surfaces, but its sensitivity to external vibrations and the inherent water layer on samples in ambient conditions often causes problems in the engagement and retraction of the tip.

We have used tapping mode exclusively throughout this work. Unlike the operation of contact mode, where the tip is in constant contact with the surface, in tapping mode the tip makes intermittent contact with the surface. As the tip is scanned over the surface, the cantilever is driven at its resonant frequency. Because the contact time is a small fraction of its oscillation period, the lateral forces are reduced dramatically. Tapping mode is usually preferred to image samples with structures that are weakly bound to the surface or samples that are soft (polymers, thin films). Since we are mostly interested in the structural information rather than know chemical properties, all the AFM analysis is done on the amplitude images.

2.6.3 Raman spectroscopy

Raman spectroscopy is widely used non-destructive method to study layered material such as graphene [195] and TMDCs [15, 196–198]. The change in the vibrational spectra due to layer thickness can be used to count the number of layers [15, 198, 199]. Resonant Raman spectra are composed of both first and second order Raman excitations, has been demonstrated for bulk MoS_2 [15] or WSe_2 [197]. In addition the excitonic behaviour is different in WS_2 and WSe_2, even though they are quite close in molecular structure. Nevertheless, the resonant Raman spectra in atomically thin dichalcogenides are relatively unexplored, and far from being fully understood.

Light scattering techniques are non-destructive tools to investigate the fundamental excitations in material, such as phonons, plasmons, etc. Due to interactions of phonons or other excitations, the incident monochromatic light of energy E_i is scattered with the same, lower (Stokes) or higher (anti-Stokes) energy. For $E_i = E_s$, the scattering is elastic and called *Rayleigh scattering*.

For $E_i \neq E_s$ case, the scattering is inelastic and called *Raman scattering* and the energy difference $\Delta E = E_i \smile E_s$ is referred as the *Raman shift*. In this scattering process, both energy and momentum must be conserved.

$$E_i = E_s \pm E_q, \tag{2.64}$$

$$k_i = k_s \pm k_q, \tag{2.65}$$

where k_i, k_s are the momenta of the incident and scattered photon on the crystal. Since we consider only the lattice excitation (phonons), and E_q and k_q are the energy and momentum of the created and/or annihilated phonons during the inelastic scattering process, which is schematically illustrated in Fig.2.20.
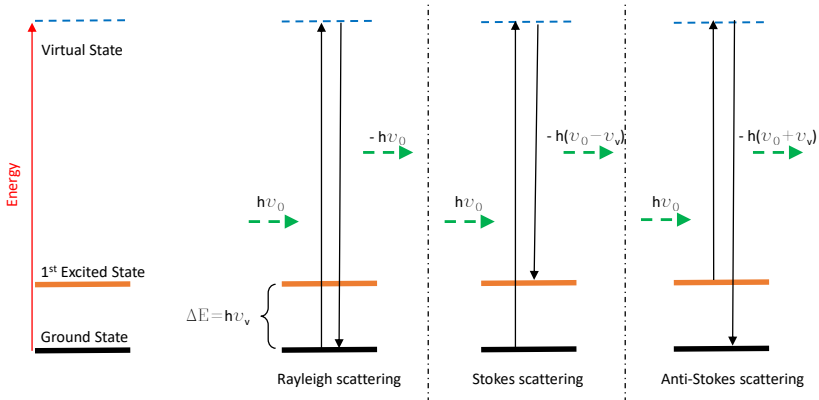
Figure 2.20: Illustration of Raman effect.

When the system is in initial state of '0', then by incident light can excite the system to a higher energy state '1' by absorption of a phonon with an energy E_q and vice versa. In contrast to photoluminescence, the intermediate state in Raman process are *virtual* and need not correspond to any real state.

Classical electromagnetism can be used to describe the light scattering process. A polarization $\mathbf{P}$ is induced in a crystal by

the electric field $\mathbf{E}$ of the incident radiation.

$$\mathbf{P} = \alpha\mathbf{E}, \qquad (2.66)$$

where

$$\mathbf{E} = \mathbf{E}_i\cos\omega_i t. \qquad (2.67)$$

Is the electric field of the incident light and α is the polarizability tensor of the crystal. The difference between static polarization originating from atoms initially in equilibrium position and dynamic polarization resulting from the lattice vibrations is defined using Taylor expansion of α

$$\alpha = \alpha_i + \frac{\partial\alpha}{\partial u_j}u_j + \frac{\partial^2\alpha}{\partial u_i\partial u_j}u_iu_j + ... \simeq \alpha_i + \alpha_1\cos\omega_q t. \qquad (2.68)$$

As a consequence the polarization is

$$\mathbf{P} = \alpha_i\mathbf{E}_i\cos\omega_i t + \alpha_1\mathbf{E}_i\left[\cos(\omega_i + \omega_q)t + \cos(\omega_i - \omega_q)t\right]. \qquad (2.69)$$

The first term corresponds to the elastic scattering of the incident light, i.e. Rayleigh scattering. The second and third terms correspond to inelastic scattering resulting in incident frequencies shifted to higher (anti-Stokes) and lower (Stokes) frequencies. These terms describe the Raman scattering in classical description.

Classically, inelastic Raman scattering is much weaker than elastic Rayleigh scattering. With first approximation, the relative Stokes and anti-Stokes intensities can be determined by the Boltzmann distribution of the phonons. The excited states are thermally populated and hence the Stokes intensity is much stronger than the anti-Stokes.

In Raman measurements, the wave vector of the incident photons is of the order of $10^5 cm^{-1}$ and create phonons with maximum wave vector of the same order of magnitude. Compared to the dimensions of the Brillouin zone, which is of the order of

$10^8 cm^{-1}$; Raman scattering with visible light probes the vicinities of the center of Brillouin zone. Quite recently, it is possible to probe larger area in the Brillouin zone using X-rays. However very intense sources, such as synchrotrons are required to have good resolution.

Summary

hybrid-PLD is the proposed method for the synthesis of ultra-thin films of WSe_2, including ML WSe_2. In-situ RHEED, AFM and Raman spectroscopy are the different experimental techniques planned for the identification of ML WSe_2. Laboratory based as well as synchrotron based XRD will be used for the investigation of the crystal structure. The electronic band structure will be measured by ARPES. Hall Effect and magnetoconductivity measurements would be used to estimate the carrier density and properties.

3. Growth and identification of mono-layer WSe$_2$

3.1 Preparation of the substrates

Oxide substrates were obtained initially from Crystal GmbH and during the later stages of the thesis, from SurfaceNet GmbH. The dimensions of the oxide substrates used are $10 \times 10 \times 0.5$ mm^3. The in-plane orientations of the substrates are marked by the vendor. This information is useful during RHEED and GIXRD measurements. Monolayer graphene (MLG) substrates were provided by Prof. Dr. Ulrich Starke's group at the Max Planck Institute for Solid State Research in Stuttgart, Germany. Epitaxial MLGs are prepared on SiC substrates by annealing at 1560 °C in the presence of H$_2$ and Ar gas. Details of the procedure can be found in Ref. [200]. The dimensions of the MLG substrates are $10 \times 5 \times 0.5$ mm^3.

The substrates have to be atomically smooth for the deposition of WSe$_2$ thin films. This is to avoid impurities and defects that could affect the growth of atomically smooth ML WSe$_2$. In order to create atomically smooth substrates, all the oxide substrates were annealed in air before the deposition.

In the case of Al$_2$O$_3$ (1$\bar{1}$02) (r-cut) substrate, three different annealing temperatures were used to observe the change in the
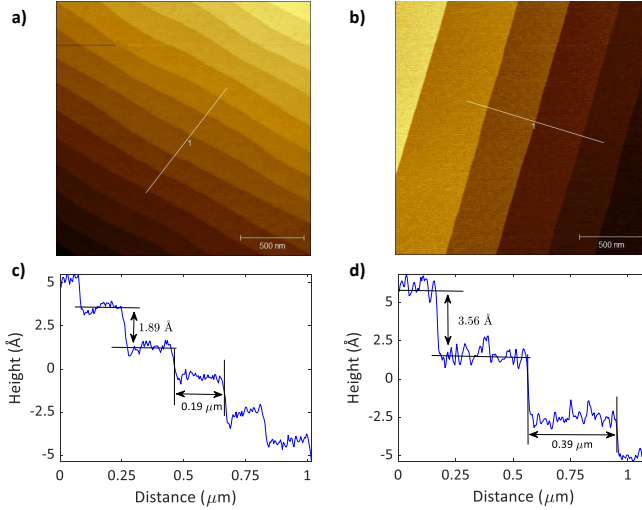
Figure 3.1: Surface of Al_2O_3 (0001) (c-cut) substrates annealed at a) 1000 °C and b) 1400 °C. The line profiles are shown in c) and d) for the line cuts marked with white lines in a) and b) respectively.

surface morphology. Step and terrace structure started evolving at 800 °C. At this temperature the edges of the steps were not straight and meanderings are observed. As the annealing temperature is increased, the meanderings of the steps started to smooth out with small steps bunching together to form wider terraces. At 1000 °C, the average step height is measured to be 3.0 ± 0.19 Å with mean terrace width of 0.4 ± 0.03 μm and the roughness on the terraces is found to be 20.84 pm. At the annealing temperature of 1400 °C, the average step height is measured to be 3.2 $\pm$ 0.27 Å, with average terrace width of 0.23 ± 0.03 μm and the roughness on the individual terrace is found to be 12.55 pm.

With the information already known about the surface behaviour of sapphire r-cut substrates at different temperature, c-cut substrates were annealed at 1000 °C and 1400 °C. At 1000 °C, the average step height is estimated to be 1.89 ± 0.21 Å,

98

mean terrace width to be 0.19 ± 0.02 μm with terrace roughness of 15.5 pm. The c-cut sapphire evolves to have wider step and terraces after annealing at 1400 °C, with mean step height of 3.56 $\pm$ 0.9 Å, mean width of 0.39 ± 0.01 μm and roughness of 32.22 pm.
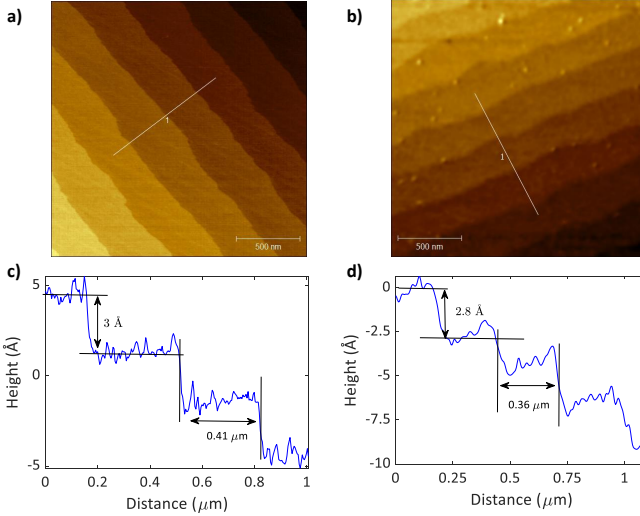
Figure 3.2: a) AFM images of Al_2O_3 ($1\bar{1}02$) substrates before deposition and b) after deposition of ML WSe_2 with their line profiles c) and d) respectively.

Al_2O_3 (012) substrate with mean step heights of 3.0 ± 0.3 Å is used to deposit ML WSe_2. Even after the growth of a ML film, the step and terrace structure were clearly visible. The average height of these steps was approximately 2.8 ± 0.3 Å. We interpret that the step height of ML WSe_2 is identical to those observed on a bare substrate, and the small discrepancy comes from the error in measurement. The AFM images of bare substrate and with ML WSe_2 deposited are shown in the Fig.3.2.

3.2 Optimisation of the growth conditions

In order to grow WSe$_2$ thin films, we need to know the flux of the elements to estimate the growth rate and optimisation of the stoichiometry of the desired compound. With the initial unavailability of flux monitors, we relied on XRD for the qualitative optimisation.
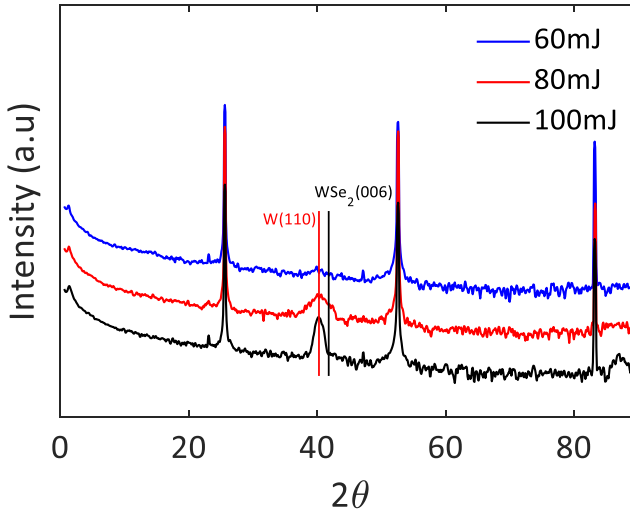
Figure 3.3: XRD is used to measure the amount of W evaporated as a function of the laser energy. Although the intention was to grow WSe$_2$ thin films, due to other optimised parameters, we could grow only pure W. This information is used optimise the magnitude of the laser energy for the ablation of W. The positions of W (110) and WSe$_2$ (006) are indicated. The sharp peaks are from the substrate.

Due to un-optimised parameters, we could only grow pure W in the beginning. This set of samples is used to qualitatively estimate the flux of elemental W with respect to the laser energy. As can be observed in the XRD shown in Fig.3.3, the amount of W decreases with decreasing laser energy. Our aim is to reduce

the W flux to a lowest possible value, which in principle slow down the growth of the WSe$_2$. Because the rate of growth is another important parameter that affects the crystallinity of the thin films. Faster growth rate does not allow for the material to stabilise into a fixed orientation and results in a polycrystalline thin films.
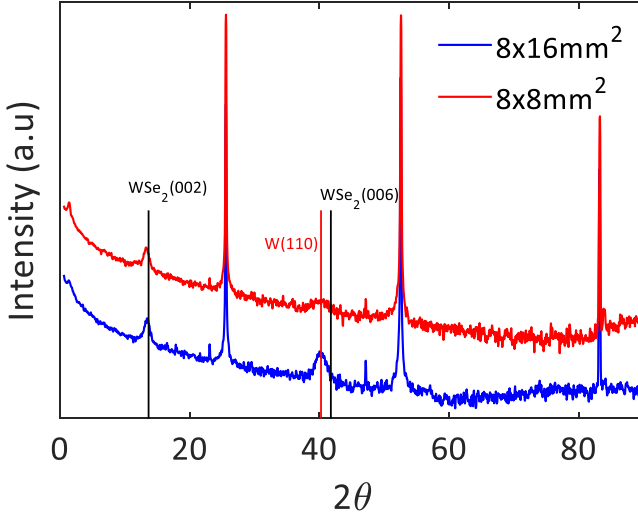
Figure 3.4: XRD of WSe$_2$ thin films deposited with same laser energy of $\sim$1.5 J/cm^2 using two different opening in the laser window. Clearly the window with smaller area reduced the intensity of the W (110) peak without affecting the intensity of the WSe$_2$ (002) peak. The advantage in varying the size of the laser opening compared to changing the laser energy, is that the laser fluence remains constant in both cases.

The rate of W flux can be reduced with lowering the laser energy. But we reach a point where certain energy is required to impart kinetic energy to the evaporated W, which is necessary for its mobility on the substrate in addition to the substrate temperature. To balance the W flux with sufficient kinetic energy but low enough flux for the suppression of the growth of pure

W, we changed the total amount of laser energy by keeping the laser fluence constant. This is achieved by reducing the opening of the laser window. As shown in the Fig.3.4, the amount of W is reduced, as inferred from the intensity of W (110) peak, without affecting the intensity of WSe_2 (002) peak when a smaller laser window is used.
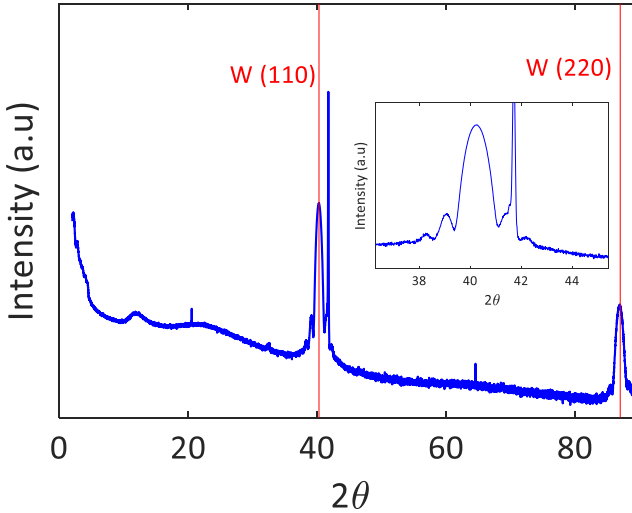
Figure 3.5: XRD of supposed to be WSe_2 thin film deposited at substrate temperature of 750 °C. As can be clearly seen, pure W is grown more than WSe_2 due to high substrate temperature and the high crystallinity that can be inferred from the Laue oscillations. The sharp peak beside W (110) is from the substrate. Insert is the magnified image of W(110) peak with Laue oscillations.

Once the excess W is minimised, the next step is to improve the crystallinity of the grown WSe_2 thin films. There are two ways this can be achieved. First, by increasing the substrate temperature during the deposition. Second is to add an annealing process after the deposition. The problem with the first method is that the high vapour pressure element gets evaporated at higher substrate temperatures. As shown in the Fig.3.5, the thin film

grown on Al_2O_3 (001) substrate at 750 °C using WSe_5 target is predominantly high crystalline W compared to the WSe_2. Most of the Se is evaporated from the substrate leaving behind a lot of low vapour pressure element W. As can be noticed in the XRD pattern, the high temperature of the substrate facilitated high crystallinity that can inferred from the Laue oscillations around the W (110) peak as shown in the insert of the Fig.3.5.
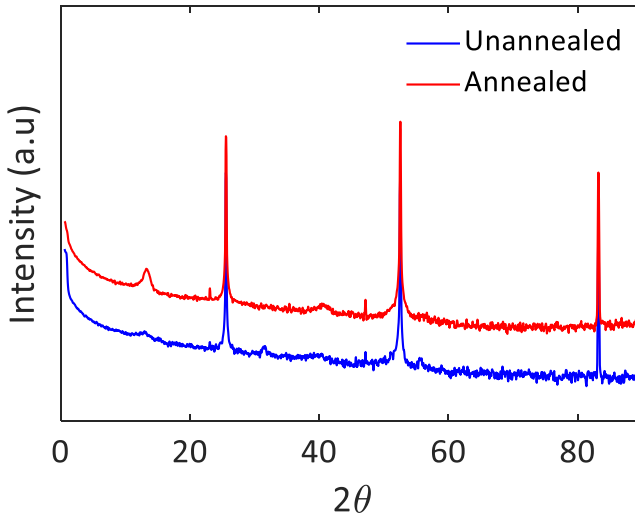
Figure 3.6: XRD of two samples of WSe_2 thin films grown on Al_2O_3 (012) substrate at 400 °C. One sample is annealed at 600 °C, while the other is un-annealed. The sharp peaks are from the substrate. The annealed sample shows sharper WSe_2 (002) peak at 13.31°.

Using the second approach, WSe_2 was grown on two substrates of Al_2O_3 (012) at 400 °C. One sample is annealed at 600 °C for an hour, while the other is kept unannealed as a control. There is significant effect of annealing on the crystallinity of the grown thin film, which can be noticed in the Fig.3.6. The WSe_2 (002) became sharper after annealing, and noticeable improvement in the (006) peak compared to the un-annealed sample.

The presence of WSe$_2$ peaks also suggests that the stoichiometry is maintained unlike in the case of high temperature deposition before. Hence we used the second approach to increase the crystallinity of the grown thin films without losing the stoichiometry of the target material.
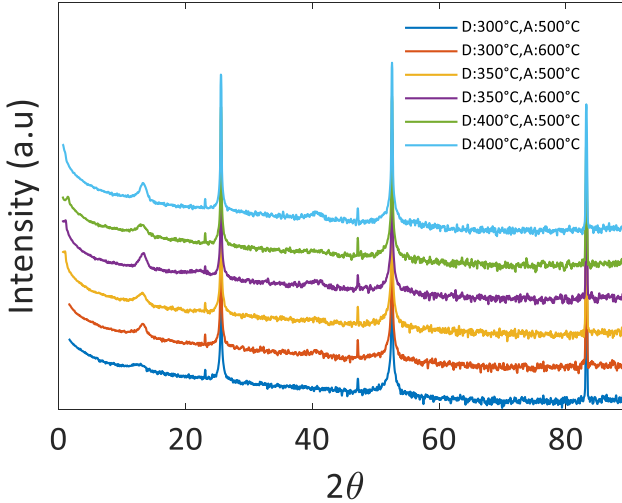
Figure 3.7: XRD of set of samples grown and annealed at different temperatures. Clear evolution of the WSe$_2$ (002) peak can be seen with increasing deposition (D) temperature. Among the samples deposited at 400 °C, the thin film annealed (A) at 600 °C shows sharper peaks compared to the rest.

With the evidence of the improvement in the crystallinity of the grown thin films by annealing, we optimised the deposition and annealing temperatures. The goal was to find optimum balance between the deposition and annealing temperatures to get high crystalline stoichiometric WSe$_2$ thin films. Six samples were grown at three different temperature and annealed at two different temperatures using fixed laser fluence of ∼4 J/cm^2. The XRD of the grown samples are shown in the Fig.3.7. Among the set of these samples, the thin film grown at 400 °C and annealed at

600 °C is found to have relatively intense WSe$_2$ (002) peak and noticeable (006) peak compared to other conditions.
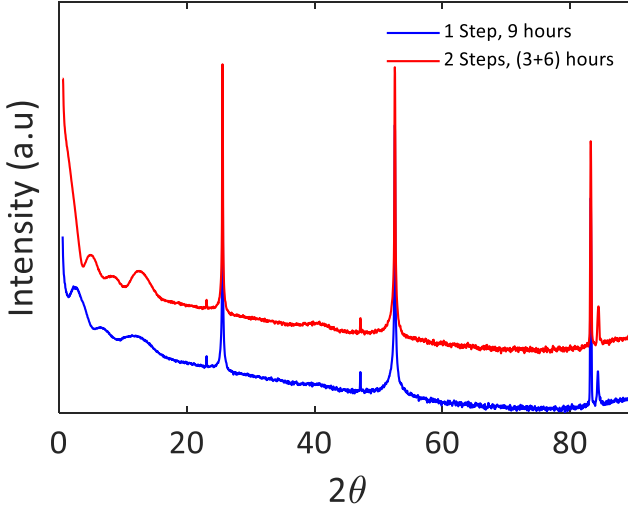
Figure 3.8: XRD of two samples of WSe$_2$ thin films grown for 9 hours in two different steps. Sample shown in blue is grown for 9 hours continuously, while the one in red is grown first at 400 °C for 3 hours and then continued at 600 °C for another 6 hours. Clear change in the crystallinity can be noticed from the sharpness of the WSe$_2$ (002) film peak.

Thereafter, we investigated the influence of deposition sequences on the growth and crystalline quality of the thin films. For this experiment, laser fluence is fixed at $\sim$5 J/cm^2 and pulse frequency of 10 Hz for 9 hours. XRD of two different samples are shown in th Fig.3.8. One sample was deposited at 400 °C for 9 hours and annealed at 600 °C for an hour. Second sample was grown first at 400 °C for 3 hours and then the deposition was continued at 600 °C for 6 more hours followed by annealing at 600 °C for an hour. The WSe$_2$ (002) film peak is relatively sharper in the case of double step process compared to the single

step. In addition, the thin film grown with single step is thicker than the double step process. One possible explanation is that the higher temperature is partially re-evaporating the grown compound which is suppressed at a relatively lower substrate temperature.

With further refinement, we reached the optimum conditions for the growth of WSe_2 thin films. The substrate temperature is maintained at 450 °C during the deposition. The substrate temperature is raised to 600 °C for the second step of deposition for thicker sample and all samples are annealed at 640 °C. We optimised the laser conditions, with pulse frequency at 10 Hz and laser energy of 55 mJ at the laser window. This translates to laser fluence of $\sim$2.5 J cm^{-2}. Throughout the thesis work, the chamber pressure during the deposition was maintained around 5×10^{-7} mbar. Se flux was measured by QCM in the second half of the thesis work and was maintained in between 1-2 Å s^{-1}.

3.3 Confirmation of 2D nature by in-situ RHEED

In-situ RHEED is used as a qualitative characterisation technique for the deposited ML WSe_2. The RHEED pattern of the bare substrates are captured before the deposition of WSe_2. This pattern consists of reflection spots, called Bragg spots due to the 3D nature of the substrate. The intensity of the Bragg spots starts to diminish quickly with the start of the thin film deposition. As the deposition progresses, the intensity of the spots reaches a minimum at the half way through the deposition. It is the effect of maximum roughness of the surface at the half time. Thereafter, reflection pattern consisting of line streaks emerges and reaches the maximum intensity at the completion of the monolayer of the deposited thin film. The reason for the line pattern is that the ML is confined to 2D plane and the third axis is missing. This results in the extension of the Bragg spots into lines. The transition of reflection spots into line streaks can be used as an indicator for

the transition from the bare 3D substrate to 2D monolayer of the deposited thin film.
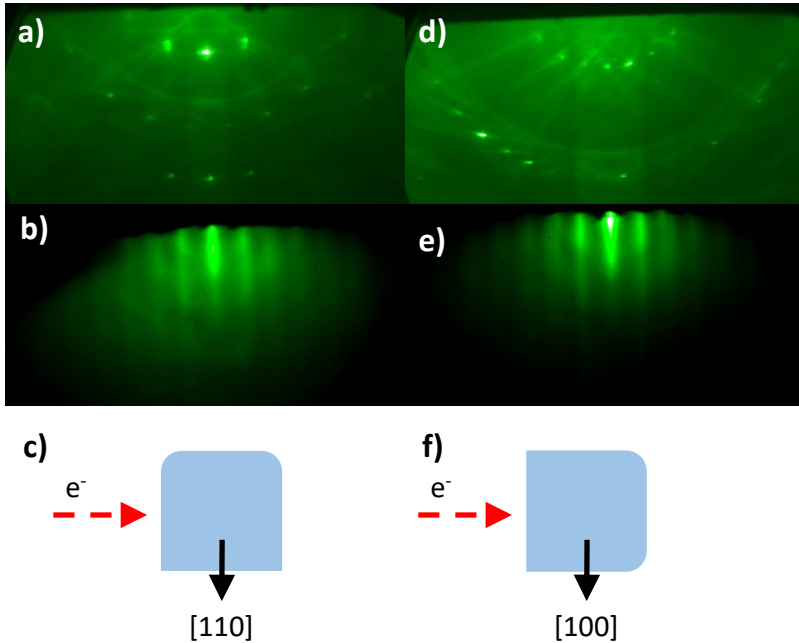
Figure 3.9: a) Bragg reflection spots with the beam direction is along Al_2O_3 [100], and in this condition diffraction from orthogonal (110) plane can be monitored on the screen. b) RHEED streaks of ML WSe_2 deposited on Al_2O_3 (001) in the same direction as (a). c) Illustration of the orientations for the images in (a) and (b). d) Bragg reflection spots with the beam direction is along Al_2O_3 [110], and in this condition diffraction from orthogonal (100) plane can be monitored on the screen. e) RHEED streaks of ML WSe_2. f) Illustration of the orientation for (d) and (e).

With the information of the substrate orientation provided by the supplier, the pixel separation can be calibrated using the in-plane lattice constant of the substrate. The separation between
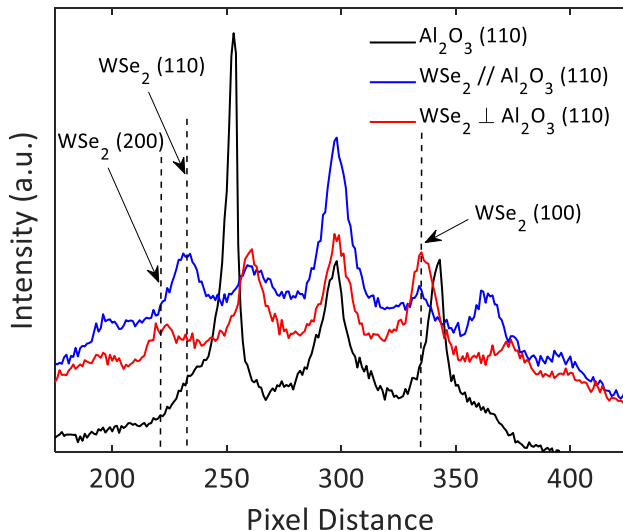
Figure 3.10: The line profiles of images from the previous figure. The line profiles of ML WSe$_2$ in both directions overlapped with substrate line profile. As can be observed, the deposited films have rotational disorder.

the Bragg spots is inversely proportional to the distance between lattice planes. This distance measured in pixels is used to calibrate the pixel distance on the RHEED screen. This is later used to measure the separation between the line streaks from the sample. Using the separation of the Bragg reflections, the orientation of the thin film can be identified with respect to the substrate.

RHEED images of the bare substrate Al$_2$O$_3$ in the direction of [110] and [100] are captured at 450 °C before the deposition of ML WSe$_2$, as shown in Fig.3.9(a,d). In our case, the pixel distance of 45 is inversely proportional to 2.379 Å (for d$_{Al_2O_3(110)}$). From this, the distance between two pixels is calculated to be 0.00934 Å^{-1}. Using the distance between the line streaks from ML WSe$_2$, the lattice parameters can be estimated. This is found to be 2.973 Å for pixel separation of 36. This is closer to the distance between

ML WSe$_2$ (100) planes with error of 4.6 %. Similarly, the distance between the line streaks in the image captured by rotating the sample by 30° with respect to the previous angle is found to be 67 pixels apart. This turns out to be 1.6 Å, which is close to the distance between the WSe$_2$ (110) planes of 1.64 Å.
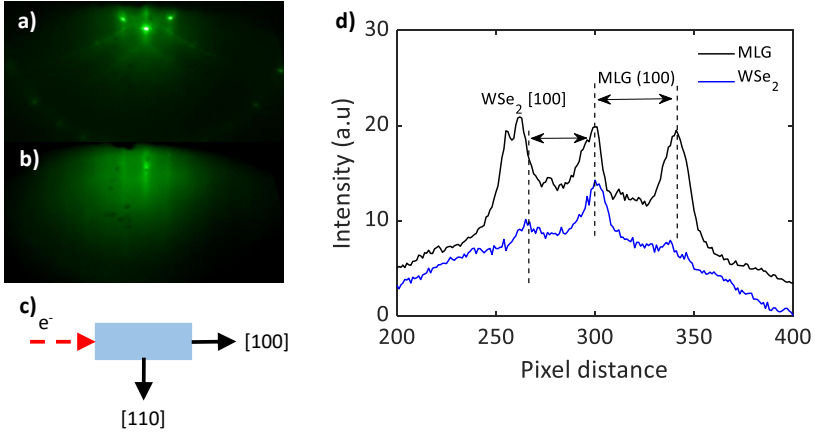
Figure 3.11: a) RHEED streaks of MLG on SiC substrate. b) RHEED streaks of ML WSe$_2$ deposited on MLG. c) Illustration of the orientations in which RHEED images are captured. d) Line profiles of ML WSe$_2$ and MLG.

As can be seen from the line profiles in Fig.3.10, we have WSe$_2$ (100) reflections on both orientations of the Al$_2$O$_3$ (001) substrate, which are along [110] and [100]. It is not clear where this rotational disorder arises. Our initial suspicion is the temperature. However, ML WSe$_2$ get more crystalline at higher temperatures, as inferred from the width of the line streaks which gets narrower with higher temperatures. The next probable cause of the rate of growth of the sample.

RHEED images of the bare MLG substrate in the direction of [100] are captured at 450 °C before the deposition of ML WSe$_2$ as shown in Fig.3.11. In this case, the pixel distance of 41 is inversely proportional to 2.13 Å. From this the distance between two pixels

would correspond to 0.01144 Å^{-1}. The inter-planar distance is estimated to be 2.495 Å for the pixel separation of 35 between the line streaks of ML WSe$_2$. This is closer to the distance between ML WSe$_2$ (100) planes with error of 12.19 %. Although quantitative information can be extracted from the RHEED analysis, the error is high due to low resolution and inaccuracies in the measurement of the pixel distances. Qualitatively, the Bragg spots of the substrate are replaced by the line streaks of the deposited ML WSe$_2$. This is used as an indicator for the deposition of the ML WSe$_2$ and X-ray diffraction is used for the estimation of the precise lattice parameters.

3.4   Estimation of island size by AFM
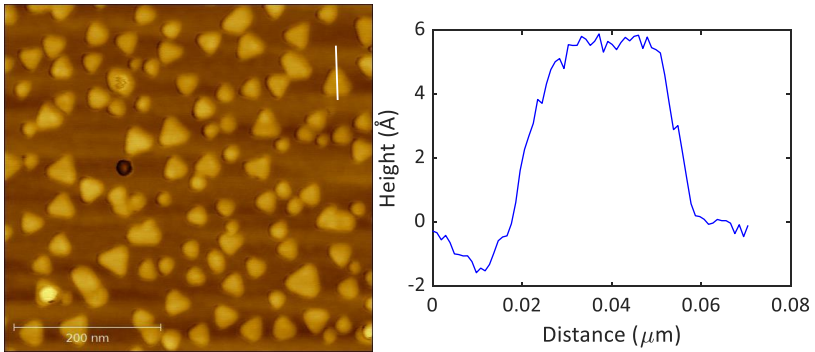
Figure 3.12: AFM image of ML WSe$_2$ deposited on Al$_2$O$_3$ (001) with b) line profile across an island of WSe$_2$.

On Al$_2$O$_3$ (001) substrate, clear triangular islands of ML WSe$_2$ are observed. The mean height of the islands is 6.5 $\pm$ 0.3 Å. This value is the height of half unit cell of bulk WSe$_2$, i.e. a ML of WSe$_2$. With the density of the islands on the substrate, approximate coverage of the ML WSe$_2$ is estimated to be $\sim 50\%$. This allows us to calculate the duration the deposition required to have complete ML WSe$_2$ or its multiples for thicker films. In

later part of this thesis, X-ray reflectivity (XRR) of this set of thin films is presented. This has been consistent with our estimate of about 4 hours duration for deposition of nearly-complete ML WSe$_2$. The island size between 10-60 nm is observed on c-cut sapphire substrate.
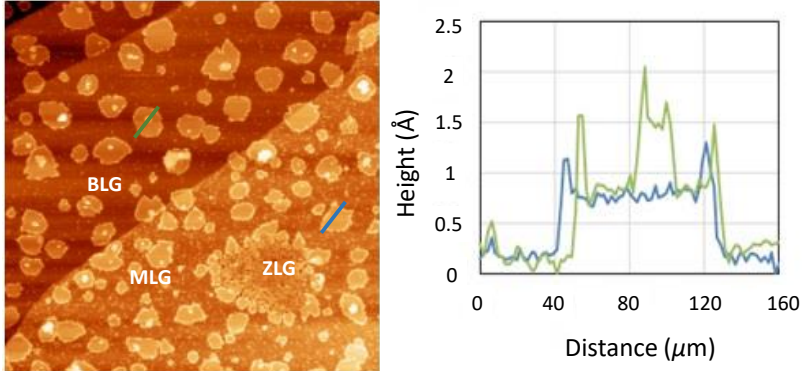
Figure 3.13: AFM image of ML WSe$_2$ deposited on MLG (001) with b) line profiles across an islands of WSe$_2$.

MLG is epitaxially grown on SiC substrate by annealing in H$_2$ gas at 1560 °C. Initially, a zero layer graphene (ZLG) is formed with some of the carbon atoms bounded to silicon in the substrate. As the annealing progress, monolayer graphene (MLG) is formed standing freely on ZLG. And some bilayer graphene (BLG) is also observed in the AFM. Since the graphene is formed with evaporation of Si atoms, the height of BLG is lower than MLG which is lower than the ZLG steps. ML WSe$_2$ is observed to be grown on all three components of graphene. Larger islands of ML WSe$_2$ are observed to be more concentrated on the MLG substrate. On some of the ML WSe$_2$ islands, second layer WSe$_2$ islands were also observed. An average height of 7.5 ± 0.3 Å is estimated for ML WSe$_2$ using AFM and 15 ± 0.3 Å is estimated for bilayer component of WSe$_2$. In the case of ML WSe$_2$ grown on MLG, the island size of 40-100 μm is recorded. The islands of

ML WSe$_2$ are observed to be larger on MLG substrates than on Al$_2$O$_3$ (001) substrate and much smaller islands is suspected on Al$_2$O$_3$ (012) substrate which are unresolved as inferred from the Fig.3.2.

3.5   Proof of monolayer by Raman Effect
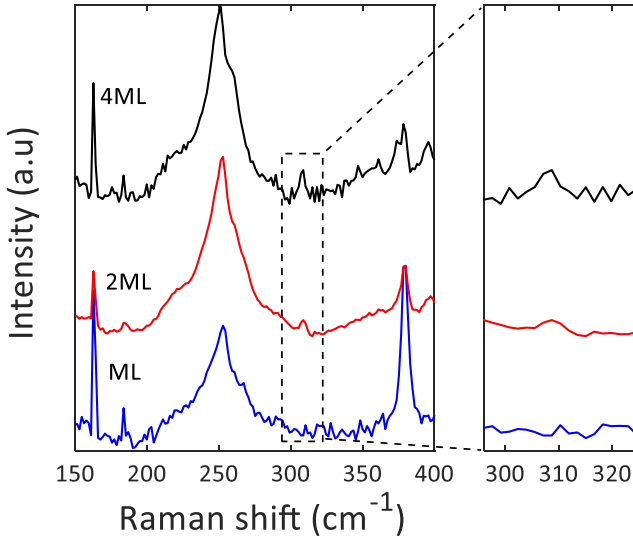
Figure 3.14: Raman spectra of ML, 2ML and 4ML WSe$_2$ using 533 nm laser. The box on the left is the zoomed image of the Raman spectra around 310 cm^{-1}. The missing 310 cm^{-1} in ML WSe$_2$ is used as an indicator for the monolayer limit.

Intense peak at 250 cm^{-1} comes from A$_{1g}$ and E$_{2g}$ (in-plane) lattice modes in WSe$_2$. This peak is identified in all the samples. A shoulder at around 260 cm^{-1} has been assigned to a double resonance transition for a longitudinal acoustic phonon. In addition the absence of 310 cm^{-1} is used as marker for the ML WSe$_2$. Raman spectra of ML, 2ML, and 4MLs is obtained using 532

nm excitation laser and normalised with respect to the 250 cm^{-1} peak. As can be seen in the Fig.3.14, the 310cm^{-1} is missing in the ML and slowly evolves as the layers increase. Another feature that can be observed, is the decrease in the FWHM of the 250 cm^{-1} peak with increasing thickness.
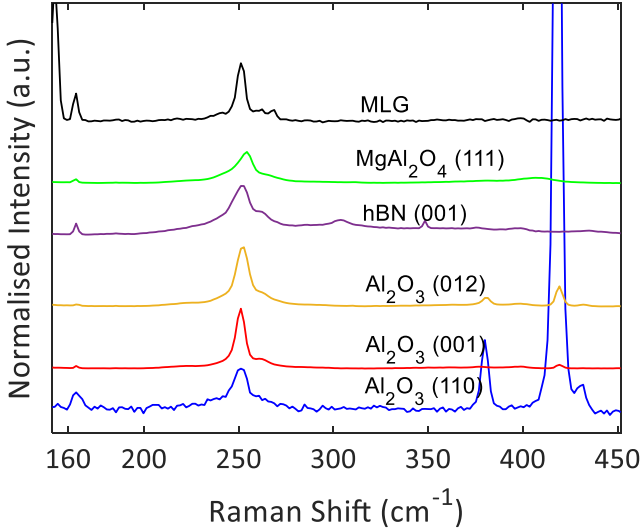
Figure 3.15: Raman spectra of ML WSe$_2$ deposited on different substrates using 533 nm laser. The x-axis is normalised using 162.4 cm^{-1} peak. The intensities are normalised using 250 cm^{-1} peak and shifted along y-axis for clarity.

Raman spectra is obtained for ML WSe$_2$ samples grown on different substrates. The ML limit of the thin films are consistently confirmed by the absence of 310 cm^{-1} peak. The Raman shift is normalised using the 162.4 cm^{-1} peak, which is present in all the spectra. There is no reports of this peak in literature, both in theory and experiments. Further work should resolve the origin of this peak.

The Raman spectra around 250 cm^{-1} is fitted with Lorentzian profiles. The peak position and the FWHM of the corresponding
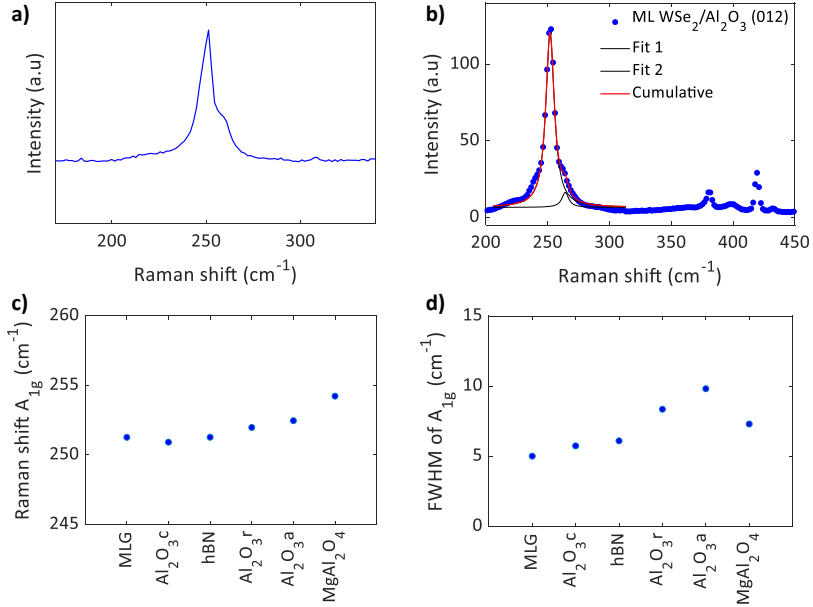
Figure 3.16: a)Representative plot of Raman spectra around 250 cm^{-1} peak deposited on Al_2O_3 (001) substrate. b) The Lorentzian curve fitting is used to fit the Raman spectra. In this case, for ML WSe_2 grown on MLG (001). c) A_{1g} peak of ML WSe_2 on different substrates. d) The FWHM of the A_{1g} peak on different substrates. There seems to be some correlation between peak position and its FWHM. The origin of the trend need further detailed investigations.

peak are extracted to plot them as function of substrate. The mismatch is not a consistent parameter to use, as some substrates are of non-commensurate hetero-epitaxy. This means that the crystal structure of the ML WSe_2 is deposited on substrate with different crystal structure. Hence, the substrate itself is used as a parameter. In addition to the FWHM, the peak position of A_{1g} itself seems to be changing depending on the substrate. Further work is needed to fully understand the mechanism behind the

substrate dependence.

Summary

We have demonstrated a method of h-PLD for the synthesis of high quality WSe$_2$ thin films down to the monolayer limit. Our technique of bottom up approach provides an epitaxial relationship between the ML WSe$_2$ and the substrates. This would allow us to perform high precision diffraction experiments and the ultra high vacuum of the growth chamber keeps the surface pristine required for the surface sensitive experiments. This technique can be extended for the synthesis of other materials requiring very low vapour pressure elements. Synthesis of WSe$_2$ is confirmed with the use of RHEED, AFM and Raman spectroscopy. Raman peak at 250 cm^{-1} is observed to be changing depending on the substrate used. More systematic experiments are required to understand such substrate dependence.

---

4. Structure of monolayer WSe$_2$

4.1 Confirmation of WSe$_2$ phase

We start with the X-ray diffraction (XRD) for the structural charaterisation of the grown WSe$_2$ thin films, including monolayers. First step is to confirm the phase of the grown thin film, which is carried out with $\theta - 2\theta$ scan. For this, we start with mounting the on the Eulerian cradle. After which, we search for a $(00l)$ substrate reflection. The angles are fine tuned to have sharp reflection from the substrate peak and fixed as a reference point. Then we proceed with first experiment of $\theta - 2\theta$ scan. In this scan, the X-rays makes an angle θ with the sample and reflects at an equal angle before registering at the detector. Such a scan would allow us to trace the reflections along the normal of the sample surface. The periodic structure in the deposited film would give rise to the diffraction pattern, i.e., Bragg peak, when the X-rays scatters in phase with each other resulting in constructive interference. Using the Bragg's equation, we can deduce the spacing between the lattice planes. Using which, the out-of-plane lattice constant can be calculated. In addition, we can identify impurities in our thin film.

We used 12 keV X-ray on few layers WSe$_2$ at ANKA. In the $\theta-2\theta$ scan, we can observe as shown the Fig.4.1, all the peak can be
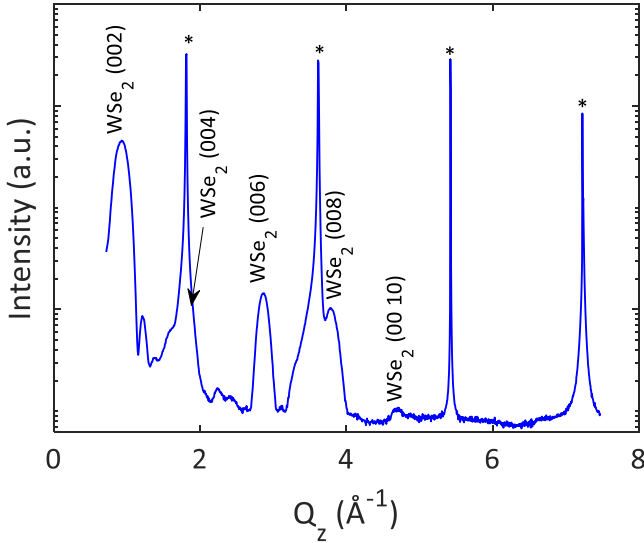
Figure 4.1: Out-of-plane XRD of 4ML WSe$_2$ deposited on Al$_2$O$_3$ (012) substrate. All the (00l) peaks are identified to be of WSe$_2$.

assigned to WSe$_2$ (00l) reflections as compared to reference bulk WSe$_2$ XRD pattern [59]. The substrate peaks are indicated by *. Using the (002) peak position and Eq.2.11 along with Eq.2.13, the c-axis is calculated to be 13.417 Å. We can infer three significant information from this scan. First the broadness of the Bragg peak suggesting very thin sample. The FWHM of the Bragg peak decreases with increasing thickness and absent in the monolayer limit. Second, as inferred from non-smooth Laue oscillations, the surface of the thin film is rough and uneven. And thirdly there are no significant impurity peaks. The impurities that we were trying to find were of pure W and oxides of tungsten.

4.2   Estimation of film thickness

A much more precise way to measure the thickness of the thin films is to use X-ray reflectivity (XRR). We used this surface
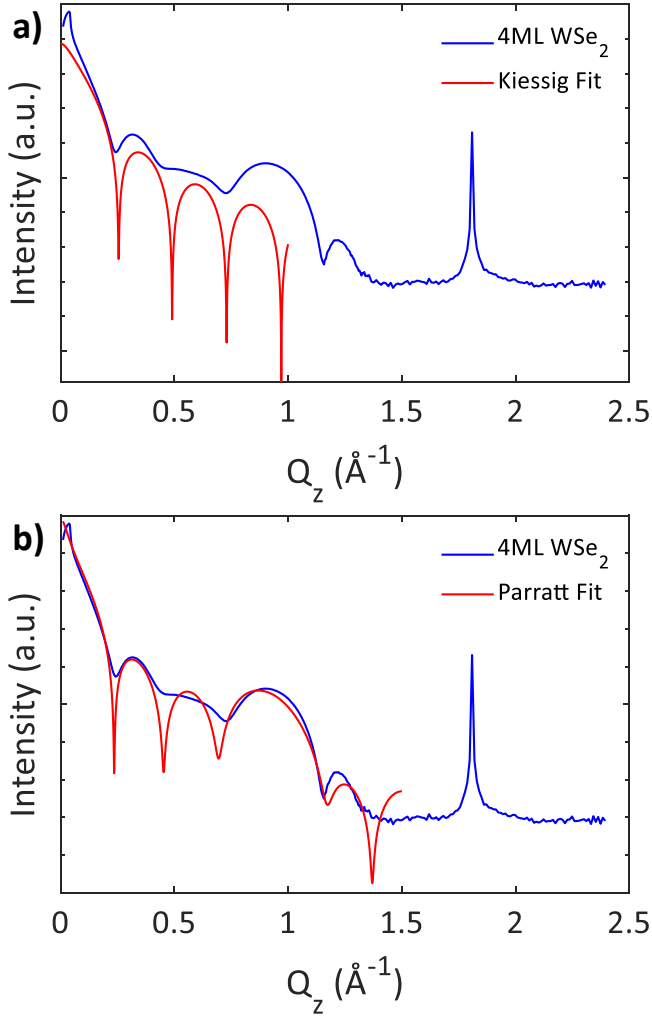
Figure 4.2: a) Kiessig fit of 4ML WSe$_2$ XRR. b) Parratt fit of the same 4ML WSe$_2$. Unlike Kiessig fit, Parratt fitting reproduces the Bragg peak.

sensitive technique to estimate the thickness of the WSe$_2$ films

grown on Al_2O_3 (012) substrates. XRR measures the intensity of the reflected X-ray in a specular condition. Depending on the sharpness of the interface, the intensity of the reflection from the surface can be modelled. The intensity diminishes with increasing roughness at the interfaces, both at the substrate and the surface of the thin film. We simulated both the Kiessig and Parratt formalisms to estimate the thickness and the fit the recorded diffraction pattern.
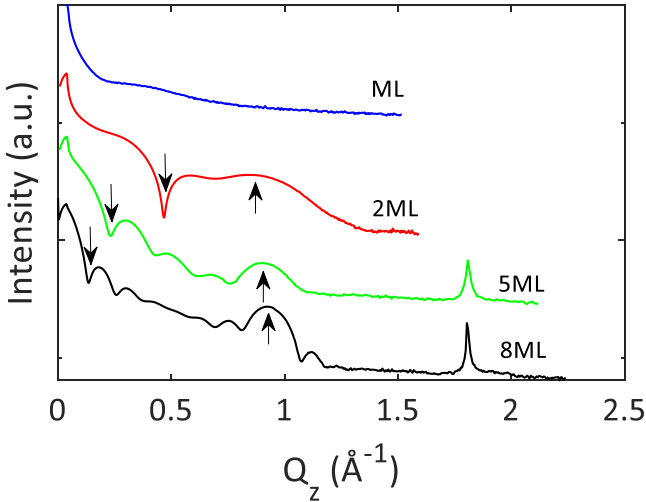
Figure 4.3: XRR of series of ML WSe_2 and the multiples of it. Two features are prominent. First, the first minima tends to go towards lower Q with increasing layer number and second, the Bragg peak moves towards bulk value of Q_z with increasing thickness.

Kiessig formalism is used to simulate the recorded reflectivity pattern of 4ML WSe_2 thin film deposited on Al_2O_3 (012) as shown in the Fig.4.2(a). This works with simple approximation of the complete thin film as a single slab with interfaces between it and the substrate, and the air. Because the material is considered as a single slab, there are no Bragg like features in the Kiessig
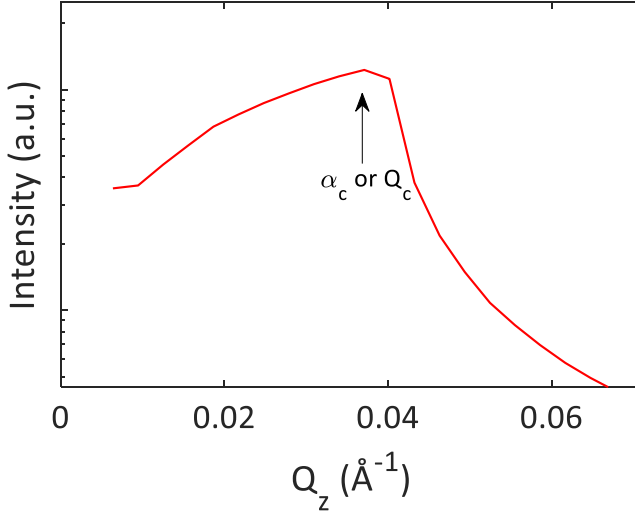
Figure 4.4: Measurement of the critical angle from the XRR of 2ML WSe$_2$ deposited on Al$_2$O$_3$ [012] substrate.

fitting. On the other hand, Parratt formalism approximates the material as collection of individual elemental slabs. Such internal structure reproduces the observed Bragg peak along with the Kiessig oscillations.

XRR of WSe$_2$ grown on Al$_2$O$_3$ (012) with different thicknesses is shown in the Fig.4.3. As mentioned before, Bragg peak will be missing in the ML limit and it is the case in our measurement. With increasing thickness the Bragg peak starts to evolve and the FWHM decreases with increasing thickness. Another interesting feature is the sharp minimum in the case of 2ML WSe$_2$. This marks the transition from ML to 2ML which makes the X-rays interfere destructively between the monolayers. As the thickness increases the first minimum is observed to move towards lower Q_z. The oscillations observed along with the Bragg peak for different samples are simulated with Parratt formula and shown in the Fig.4.5.

121
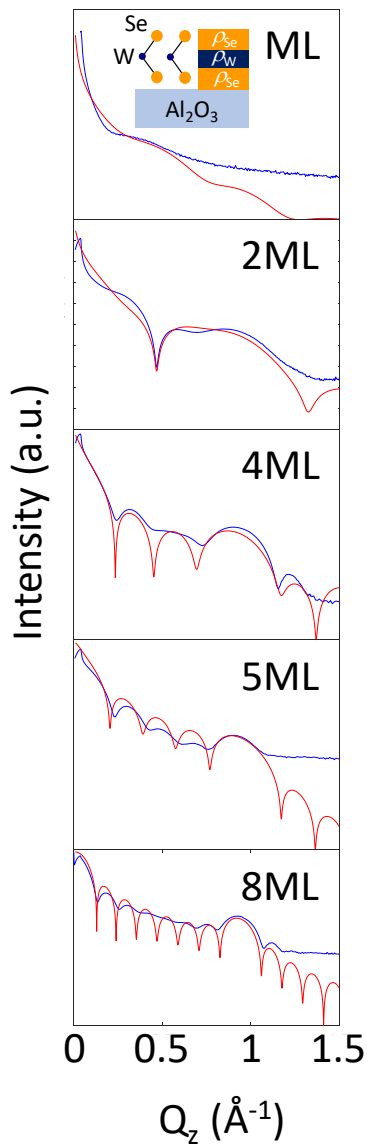
Figure 4.5: Parratt fitting of series of ML WSe$_2$ and the multiples of it. Insert in the top frame shows the elemental slabs used to model.

The second motivation for XRR is to obtain, apart from film thickness, the critical angle (θ_c). It is the angle below which X-rays undergo total external reflection. This is one of the crucial information to have before proceeding to grazing incidence X-ray diffraction (GIXRD). As shown in the Fig.4.4, the critical wave vector is indicated in the XRR of 2ML WSe$_2$ as $Q_c = 0.0371$ Å^{-1} or in other words, $\theta_c = 0.1748°$. The critical angle is given by $\sqrt{2\delta}$, where δ is to be taken from tables of optical constants for given element. The measured critical angle does not match with that of pure W, we experimentally measured the critical angle of WSe$_2$. Critical angle dictates how the incident beam is reflected at different angle. For $\frac{Q}{Q_c} \gg 1$,the reflected wave is in phase with the incident wave. The intensity of the reflectivity falls off as $(2Q/Q_c)^{-4}$ along with almost complete transmission, and the penetration depth is $\alpha\mu^{-1}$. Whereas for $\frac{Q}{Q_c} \ll 1$, reflected wave is out of phase with the incident wave, so the transmission becomes very weak. It propagates along the surface with minimal penetration depth. Due to small penetration depth, it is called the *evanescent* wave. At $\frac{Q}{Q_c} = 1$, the amplitude of the reflectivity is close to $+1$ so the reflected wave is in phase with the incident wave.

4.3 Determination of in-plane lattice constants

Using the information of critical angle, we move on to GIXRD of monolayer WSe$_2$. The properties of thin films depend on the atomic structure and the effects of substrates on them.

GIXRD is widely used to study the in-plane atomic structure. To have sufficient intensity and amplitude, we measure at an incident angle just above critical angle (we used θ=0.2°). This limits the penetration of the X-rays into the thin films and travels along the surface as an evanescent wave. The incident beam is reflected specularly, i.e., with diffracted wave makes equal angle as the incident angle. Once the angle of incidence and exit angles are fixed

with respect to the critical angle, the alignment of the sample is repeated just as normal XRD, except the substrate peak we align is the in-plane peak. We used Al_2O_3 (110) and Al_2O_3 (100) peaks positions as the reference angles for ML WSe_2 films deposited on Al_2O_3 (001) substrates and SiC (110) and SiC (100) positions for ML WSe_2 films deposited on epitaxial MLG.
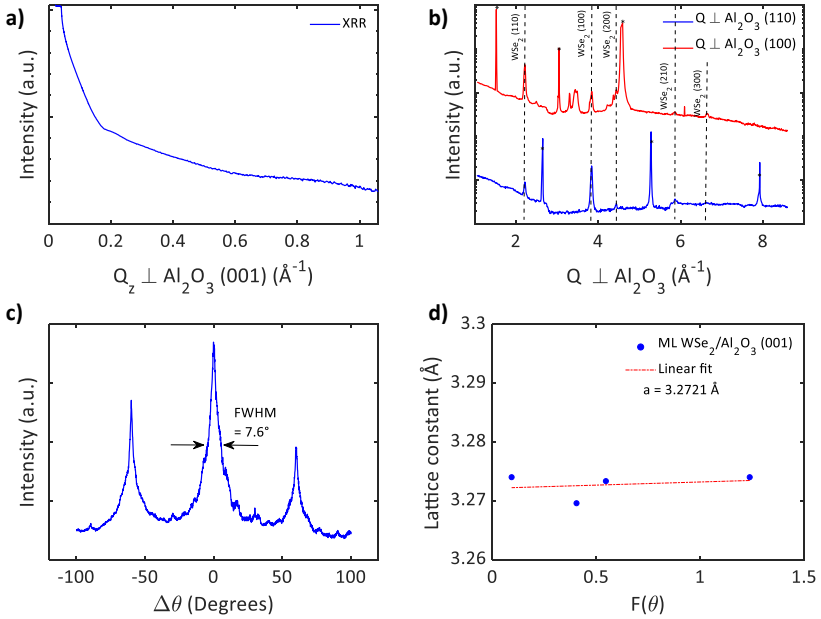
Figure 4.6: a) XRR of ML WSe_2 deposited on Al_2O_3 (001) substrate. b) GIXRD along two perpendicular directions of the substrate. c) Rocking scan of the WSe_2 (110) peak. d) Scatter plot with linear fit to estimate the in-plane lattice constant, where $F(\theta)$ is given by the Eq.4.1.

The in-plane lattice constants are estimated using the relation between the lattice constants and the function of angles given in

the Eq.4.1 to minimise the systematic errors [187].

$$F(\theta) = \frac{1}{2}\left(\frac{\cos^2(\theta)}{\theta} + \frac{\cos^2(\theta)}{\sin(\theta)}\right), \qquad (4.1)$$
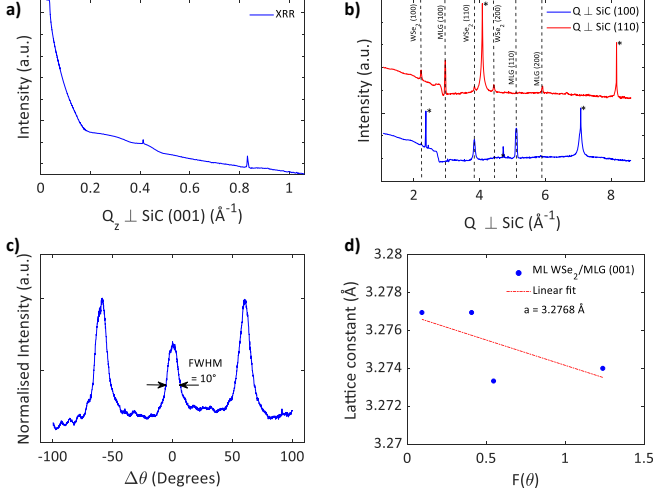
Figure 4.7: a) XRR of ML WSe_2 deposited on MLG (001) of SiC (001) substrate. b) GIXRD along two perpendicular directions of the substrate SiC. c) Rocking scan of the WSe_2 (110) peak. d) Scatter plot with linear fit to estimate the in-plane lattice constant.

ML WSe_2 deposited on Al_2O_3 (001) substrate has an in-plane lattice constant a $= 3.2721$ Å, indicating in-plane compression of 0.59%. In addition, ML WSe_2 (110) is aligned along Al_2O_3 (110) and ML WSe_2 (100) is aligned with Al_2O_3 (100). This leads to a 3×3 lattice grid of WSe_2 commensurate with 2×2 lattice grid of Al_2O_3 with 3.16% mismatch. The crystallographic locking is same as that reported by Ref. [162] but with precise value of the strain. Moreover, the 3-fold symmetry of the ML WSe_2 is evident from the 60° periodicity in the in-plane rocking scan shown in Fig.4.7(c). The FWHM is estimated to be 7.6° from the

125

rocking scan. Although it is a large value, the rotational disorder is qualitatively small as evident from the background magnitude of the intensity in the rocking scan.
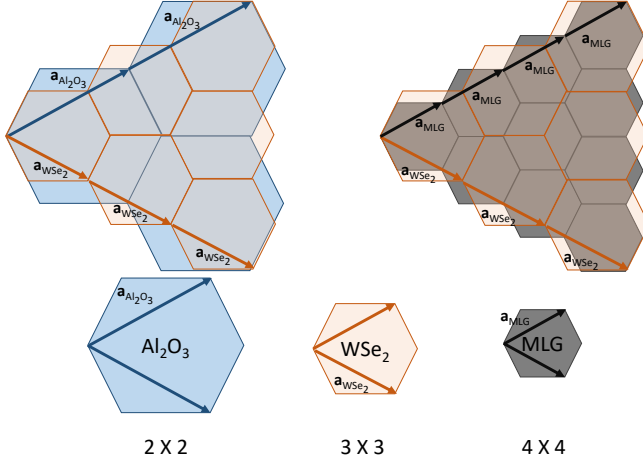
Figure 4.8: Lattice commensuration of ML WSe$_2$ on Al$_2$O$_3$ (001) and MLG.

ML WSe$_2$ deposited on MLG/SiC (001) substrate has an in-plane lattice constant a = 3.2768 Å, indicating in-plane compression of 0.12%. In addition, ML WSe$_2$ (110) is aligned with MLG (110) and ML WSe$_2$ (100) is aligned along MLG (100). This leads to a 3×3 lattice grid of WSe$_2$ commensurate with 4×4 lattice grid of MLG with 0.1% mismatch. 60° periodicity is observed in the in-plane rocking scan with FWHM of 10°.

Using the Eq.4.2,

$$t = \frac{K\lambda}{B\cos\theta_B},\tag{4.2}$$

we estimate the domain size of the deposited ML WSe$_2$ on Al$_2$O$_3$ and MLG to be 16.085 nm and 15.906 nm respectively.

From the X-ray diffraction experiments, we are able to measure the precise lattice constants in the ML WSe$_2$ grown on two

126
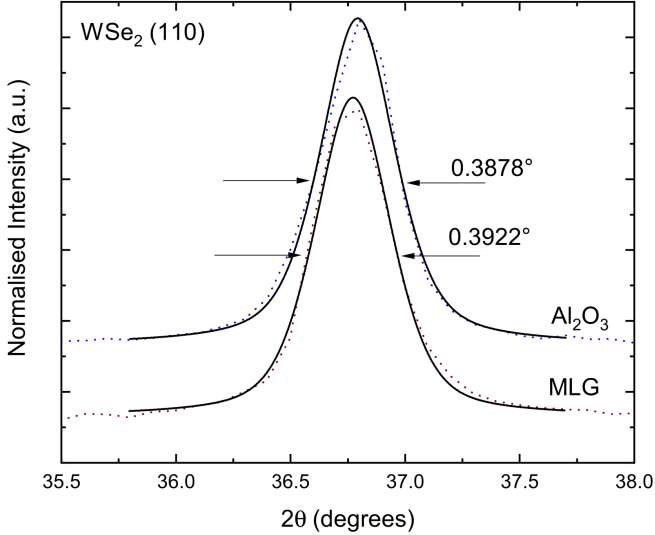
Figure 4.9: Pseudo-Voigt fitting of the WSe_2 (110) peak to estimate the domain size of ML WSe_2 deposited on Al_2O_3 (001) and MLG (001) substrates.

important substrates sapphire and graphene. This allowed us to estimate the strain in the grown monolayers of WSe_2. This is one of the significant information that we are interested to find for this thesis work. The next step is to use angle resolved photoemmission spectroscopy (ARPES) for the investigation of the spin splitting in the valance band.

Summary

Detailed and precise structural characterisation of ML WSe_2 is carried out using synchrotron based XRD, XRR and GIXRD. The in-plane lattice parameters, the epitaxial strain, and the crystal symmetry are estimated and confirmed. We have found an epitaxial relationship between the grown ML WSe_2 and the substrates.

Such an epitaxy facilitates the mapping of electronic band structure using ARPES. Moreover, the epitaxial nature opens up the possibility to change the strain in the ML WSe$_2$ by using different substrates. In doing so, we could in principle change the electronic band structure itself. This could be exploited in the fabrication of opto-electronic devices.

---

5. Electronic bands of monolayer WSe$_2$

5.1 Background

The study of electronic band structure of ML WSe$_2$ poses three considerable challenges. First it is difficult to obtain atomically smooth and oriented samples of ML WSe$_2$. Next is to keep the surface uncontaminated to perform a surface sensitive experiment such as angle resolved photoemmission spectroscopy (ARPES). And finally, to have high intensity and resolution to plot the ARPES signal as a function of parallel momentum.

Finteis et.al. [201] reported synchrotron based ARPES data on bulk WSe$_2$ grown by chemical vapour transport method. In addition, they compare their data to full-potential relativistic density-functional band structure calculations. Bulk WSe$_2$ is expected to be an indirect band gap semiconductor from the band calculation. This is supported by experimental band gap of ∼1.2 eV at 300 K with valance band maximum (VBM) at **K** to conduction band minimum (CBM) between **Γ** and **K**.

Another ARPES data was also taken on a CVD grown WSe$_2$ single crystal by Ref. [202]. But they intercalated the single crystal with alkali atoms which decouples the surface layer from the bulk, making it quasi-monolayer WSe$_2$.

Furthermore, Agnoli and his group used μ-ARPES on CVD

grown ML and BL WSe$_2$ on epitaxial graphene [203]. In the ML WSe$_2$ case, a clear splitting of 0.5 eV in the valance band at the **K** point of the Brillouin zone. Moreover, the effective mass of the electron in the split bands is found to be 0.4 m$_e$ and 0.7 m$_e$. The VBM is reported to be at **K** point which levels equal to **Γ** at 1.3 eV below Fermi level in the BL WSe$_2$ case.

Couple of more groups [7, 177] reported the spin splitting of the valance band in the ML WSe$_2$ to be 0.43 eV and 0.513 eV respectively. 0.513 eV is the largest spin splitting measured in an exfoliated ML WSe$_2$ experimentally. Le et.al. [177] mapped the band structure using ARPES and compared it to the first principle calculations. Two major discrepancies were noticed. First the magnitude of the SO splitting of the valance bands and second the difference between the **Γ** and **K**-point in the Brillouin zone are inconsistent with first principle calculations. The SO splitting of 513 meV exceeds the calculated 450 to 470 meV range obtained in the calculations.

MBE grown ML WSe$_2$ are characterized using ARPES, and the splitting of 0.43, 0.5 eV, and 0.47 eV are reported by [7, 131, 132]. Spin resolved ARPES is reported by Sugawara et. al. [131] for ML WSe$_2$ epitaxially grown on bilayer graphene. APRES revealed the spin splitting of the valance band at the **K**-point to be 0.5 eV. Valance band maximum is located to be at the **K**-point instead of the **Γ**-point. The energy difference between **Γ**−**K** is estimated to be 0.6 eV. Using spin resolved ARPES the in-plane and out-of-plane spin polarization is observed. In-plane spin components show no difference in two spin-split bands, whereas the out-of-plane component revealed clear difference in the two bands. Similar results are reported by Mo et. al. [132], with spin slitting of 470 meV in the valance band at **K**-point.

The variation of the magnitude of the spin splitting in ML WSe$_2$ among different studies is suspected to be coming from the strain in the ML WSe$_2$ [7]. To clarify this point, we provide ARPES data and compare it with first principle calculations. In addition, we have measured the precise lattice constants and

strain in the ML WSe$_2$ using diffraction experiments presented in the previous chapter. This should address the open questions about the influence of strain on the magnitude of giant spin splitting in the valance band.

5.2   Spin splitting of the valance band at K

ARPES is obtained using partially covered WSe$_2$ on epitaxial MLG on SiC substrate. As observed from GIXRD, there is an epitaxial relation between WSe$_2$ and MLG and LEED measurement compliments it. WSe$_2$ (100) is aligned along graphene (100). The epitaxial relationship of the vdW heterostructure results in a reciprocal space alignment as shown in Fig.5.1(a). The raw APRES spectrum taken along the $\mathbf{\Gamma-K}$ direction of WSe$_2$ is shown in the Fig.5.1.
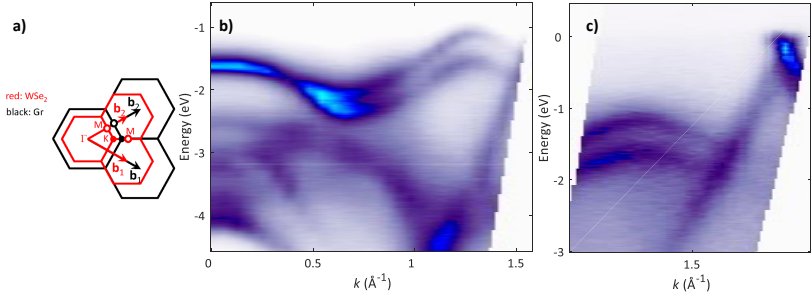
Figure 5.1: a) The reciprocal space of ML WSe$_2$ overlapped with graphene. b) The ARPES data taken along $\mathit{\Gamma-K}$ direction of the ML WSe$_2$ clearly showing the spin splitting on the valance band. c) ARPES data of the Dirac point of the graphene and the part of the valance band of the ML WSe$_2$.

The spectrum resolves the valence bands of monolayer WSe$_2$ with excellent quality, essentially consistent with the result of the first principles calculation as discussed in the Sec.2.3. Large spin splitting (Δ_{so}) due to the breaking of inversion symmetry in ML
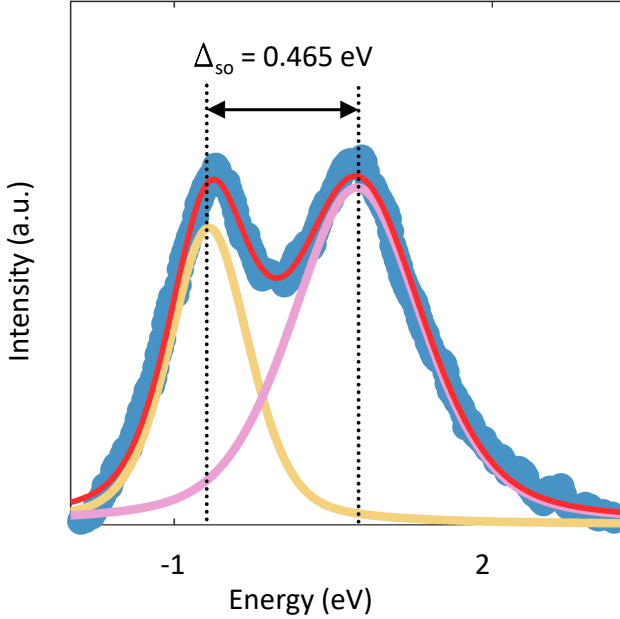
Figure 5.2: EDC extracted at **K** of WSe$_2$ together with the fit that consists of two pseudo-Voigt functions.

WSe$_2$ is clearly resolved in the raw spectrum. As expected from the reciprocal space alignment, graphene Dirac bands also appear in the spectrum at high **K**.

The quantify the spin splitting precisely, an energy distribution curve (EDC) is extracted at the **K**-point. From the separation of the peaks of fitted pseudo-Voigt curves shown in Fig.5.2, we obtain $\Delta_{so} = 0.465$ eV. This value is smaller than Δ_{so} observed in an exfoliated monolayer WSe$_2$ (513 meV) [177], MBE grown ML WSe$_2$ on bilayer graphene (0.475 eV) [7] and CVD grown ML WSe$_2$ (0.5 eV) [203].

5.3 Strain effect on spin splitting examined by first principles calculation

First we discuss the electronic band structure of an unstrained (Δa=0%) ML WSe$_2$. The spin splitting in the valance band is observed to be at **K**-point in the Brillouin zone due to strong spin orbit coupling and broken inversion symmetry. The value of spin splitting in unstrained ML WSe$_2$ is predicted to be 452.4 meV. The energy difference between the upper spin split band at the **K**-point in the Brillouin zone and the Γ point is predicted to be 537 meV.
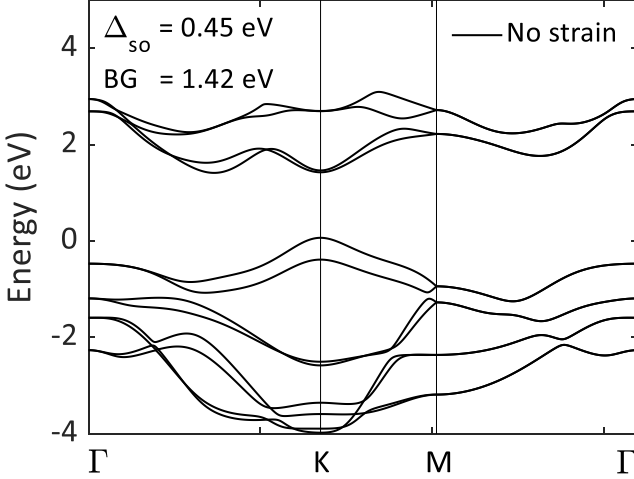
Figure 5.3: Band structure calculated for unstrained (Δa=0%) ML WSe$_2$. The Fermi level seems to cut the valance band, but can be considered within the error-bar of 10%.

Second, we derive the effect of strain on the spin splitting by performing first principle band structure calculations for different values of strain (Δa: -10% to 10%) keeping the cell volume constant. We observed change in three different parameters with change in strain. The magnitude of spin splitting in the valance

band at the **K**-point changes quite drastically and we have used polynomial of 4th order to fit the predicted values. This allows us to estimate the spin splitting for a given strain in the ML WSe$_2$. Second, significant changes are also observed in the bandgap and the energy difference between the top spin split band and the lowest conduction band at the **Γ** point in the Brillouin zone. As well as the semiconducting to metallic transition is predicted with changing strain.
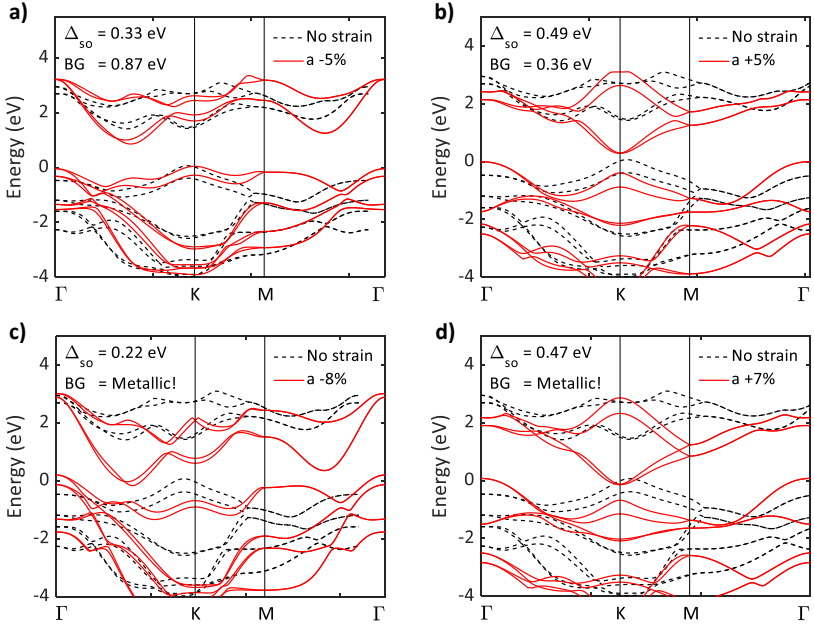
Figure 5.4: Band structure calculated for strained ML WSe$_2$. a) -5% and b) +5% remain semiconducting. Whereas, strain of c) -8% and d) +7% lowers the conduction bands to make it metallic. Additional band structures with strain are added in App.C.

We now compare our theoretical calculations with experiments. The magnitude of spin splitting in our epitaxial monolayer WSe$_2$ is determined to be 465 meV as we showed in Fig.5.2.

The value of Δ_{so} is 48 meV smaller than the spin splitting of 513 meV observed in the exfoliated ML WSe2 [177].
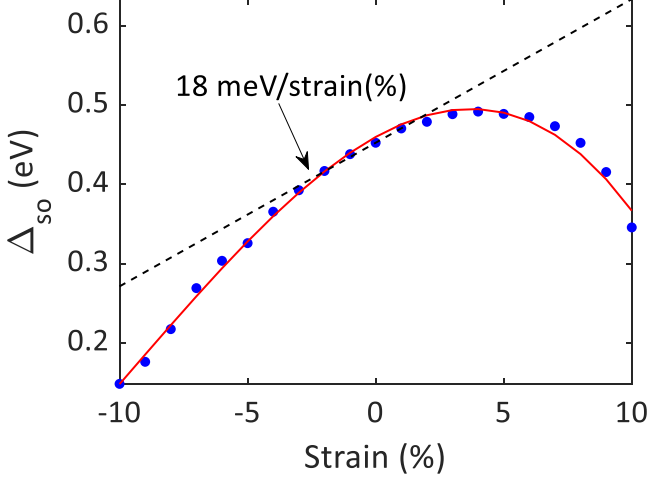
Figure 5.5: Phase space of the strain in the ML WSe$_2$ and the magnitude of the spin splitting of the valance band at the **K** in the Brillouin zone. The middle section is approximated with a straight line and the slope is calculated to be 18 meV/strain(%).

If we assume that exfoliated WSe$_2$ is unstrained, the discrepancy could be due to the strain in our film. To estimate the modification of Δ_{so} coming from strain, we used a linear approximation to fit the theoretical data for Δ_{so} vs. strain. The linear approximation results in slope of $\sim$18 meV / strain (%).

Using this value and the input of measured strain by GIXRD (-0.12%), we estimate the renormalization of Δ_{so} due to strain in our film to be 2.2 meV. This is too small to describe the experimental discrepancy between our epitaxial film and exfoliated monolayer WSe$_2$. Thus, the strain in our film cannot explain the difference in Δ_{so}.

Although it is more natural to assume that the film is strained and exfoliated WSe$_2$ is not, in order to provide alternative sce-
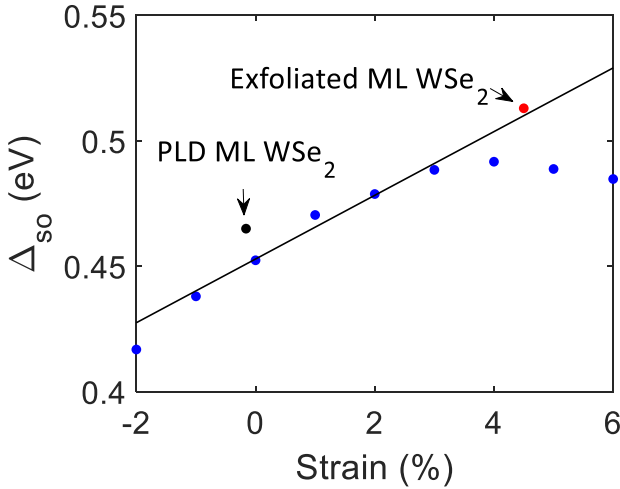
Figure 5.6: The magnitude of spin splitting is plotted against the strain and fitted with linear function. The measured spin splitting of 0.465 eV in our sample with 0.12% strain is shown with black marker. The strain required to achieve the spin splitting of 513 meV in exfoliated sample as reported by [177] is estimated to be 4.5±0.5%.

nario, we invoke the possibility that exfoliated WSe$_2$ is strained after transferred to the substrate. As can be seen from Δ_{so}-strain relationship derived from theory, in this case exfoliated WSe$_2$ should have tensile strain to have larger Δ_{so}. Using the same linear analysis, we can estimate that the tensile strain needed to explain the difference is 4.5±0.5%. However, we do not have direct strain data available from other studies, we could show from our theoretical analysis that only a small amount of strain ($\sim$4-5%) can indeed induce a difference in Δ_{so} as seen among other experiments. Before closing this analysis, we stress that our complete set of structural and spectrum information enabled for the first time to quantitatively discuss such strain effect on electronic
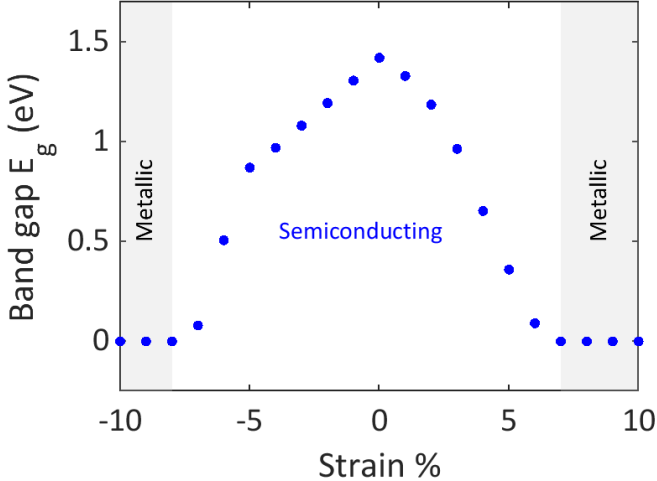
Figure 5.7: Band gap of the ML WSe$_2$ is plotted against the strain induced. It is interesting to note that ML WSe$_2$ undergoes semiconductor to metal transition at higher strains in both directions.

structure in monolayer WSe$_2$.

In addition to the strain effect on spin splitting, we found another interesting strain effects in our first-principles study. The bands are changing as the in-plane lattice constant is compressed or stretched. This pushes ML WSe$_2$ from semiconducting state to metallic state. Especially on the tensile side, the maximum strain that ML WSe$_2$ can endure without fracture and mechanical failure is $\sim 7.3\%$ [204]. This is at the borderline and would in an interesting feature to observe.

5.4   Band alignment and charge transfer

When materials with different electronic band structures are brought in contact with each other, as in the case of our present heterostructure, the shape of the bands changes at the interface de-

pending on the properties of individual material. Every material has three important landmarks in its band structure. They are the maxima of the valance band, minima of the conduction band and the Fermi level, which is the level up to which the electrons are filled at the absolute zero. At an interface between two different materials, the bands bend such that the Fermi level is at equal position in both the materials. The band alignment at the interface is formed by metallic graphene and semiconducting ML WSe$_2$. This allows us to understand how the charge transfer takes place in this basic van der Waals heterostructure. Understanding of the charge transfer is crucial when planning to fabricate other van der Waals heterostructres.

The work function ϕ of graphene is measured using ultraviolet photoemission spectroscopy (UPS), before and after deposition of the ML WSe$_2$. We obtained $\phi = 4.13$ eV, and 4.40 eV, before and after the deposition of WSe$_2$, respectively. From the UPS and ARPES results, we derive the band alignment at the WSe$_2$/epitaxial graphene interface. Bulk polarization of SiC induces upward band bending, which would result in p-doping on the surface when terminated by a clean interface. But in reality is overcompensated by donor states at the graphene/SiC interface, resulting in the n-type character of epitaxial MLG/SiC [205] with its Dirac point residing 0.41 eV below E$_F$. The valence band maximum of WSe$_2$ with respect to E$_F$ (E$_K \sim$ -1.1eV) matched very well with that of epitaxial WSe$_2$ grown by MBE, despite the latter being grown on bilayer graphene instead of a monolayer [7]. By adopting the band gap E$_G$=1.95 eV determined by STM, we estimate that E$_F$ is located 0.85 eV below the conduction band minimum (CBM). This makes E$_F$ in WSe$_2$ closer to the CBM.

ARPES showed that the graphene bands were also shifted before and after the WSe$_2$ growth. To our knowledge, such a band shift of graphene upon TMD growth was not observed previously. There are two possible mechanisms to explain this observation. First, the electron transfer from graphene to WSe$_2$ could shift the graphene bands upward. Second, if the donor states at
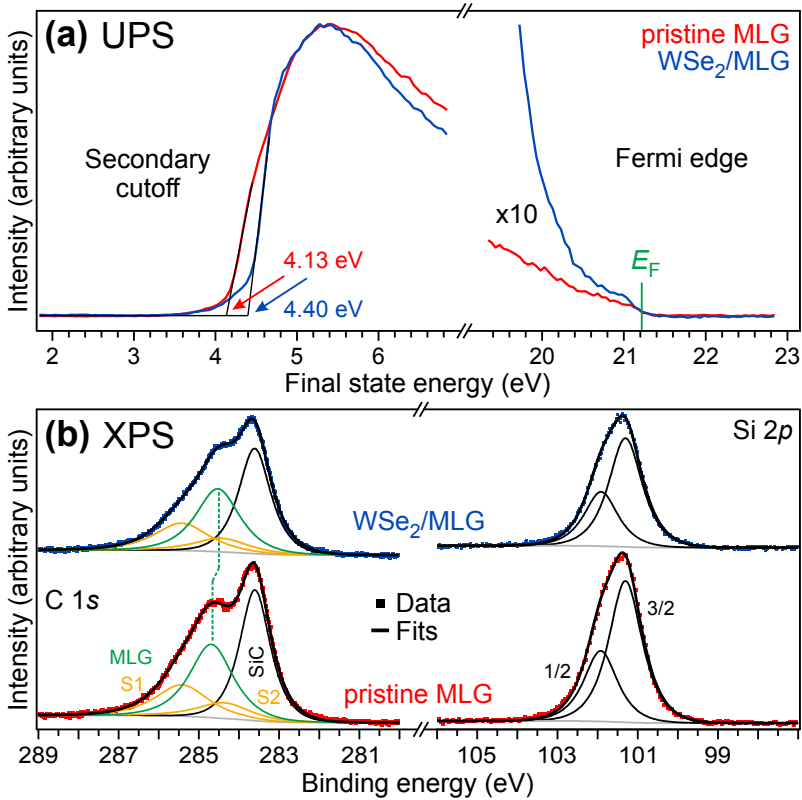
Figure 5.8: UPS and XPS data taken before and after the deposition of WSe2. (a) UPS data used to extract EF as well as the cut-off of secondary electrons from which the work function is evaluated. (b) XPS data showing core levels of C 1s and Si 2p. No shift is observed in the core levels, indicating that the band bending at the graphene/SiC interface is unaltered by WSe$_2$ growth.

the graphene/SiC interface are partially compensated during the TMD growth (e.g. via chemical reaction with Se vapour), the amount of electron doping to graphene could be modified. In the latter case, modified donor states should change the band bending
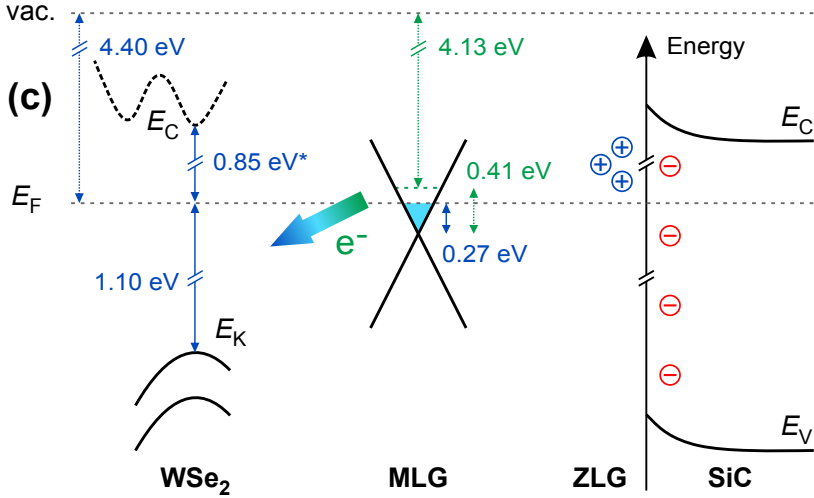
Figure 5.9: Schematics of the band alignment from ARPES and UPS measurements of WSe$_2$/'MLG heterostructure.

at the graphene/SiC interface, which could be detected via the shift of core levels. The core level spectrum for Si and C before and after the WSe$_2$ deposition showed, however, that the positions of the peaks were unaltered. Thus, we conclude that the shift of graphene bands observed in this study originates from the electron transfer from graphene to WSe$_2$. This is consistent with the larger work function observed for WSe$_2$ compared to the original MLG/SiC.

ML WSe$_2$ on MLG is one of the simplest heterostructure to make and it allows us to better prepare for other heterostructures that could be fabricated. One of the future plan is to deposit ML WSe$_2$ on superconducting NbSe$_2$. Being of similar class of electronic materials, we can expect similar charge transfer mechanism between ML WSe$_2$ and NbSe$_2$. Moreover, the magnitude of the charge transfer is an important information for precise doping of ML WSe$_2$ to access interesting areas in the electronic band structure.

Summary

*The expected spin splitting of the valance band at **K**-point due to broken inversion symmetry and strong SOC is observed in the electronic band structure mapped by ARPES. This confirms that our method of h-PLD is capable of growing high quality thin films of WSe$_2$. The estimated spin splitting is compared with first principle calculations that include strain in the ML WSe$_2$. This allowed us to create a phase space of strain and the magnitude of spin splitting using experimental GIXRD and ARPES results and theoretical first principles band structure calculations. Moreover, the feasibility of fabricating van der Waals heterostructure is confirmed.*

In addition, we have uncovered a charge transfer phenomenon between the MLG substrate and the ML WSe$_2$. This has an interesting consequence of n-doping the ML WSe$_2$. In order to access the spin polarised valance bands, ML WSe$_2$ needs to be hole-doped. Hence, the phenomenon of charge transfer between the substrate and ML WSe$_2$ needs to be considered carefully in the heterostructures. This is especially important in the case of heterostructure of ML WSe$_2$ and superconducting NbSe$_2$, in which the objective is to induce superconductivity in the spin split bands. The magnitude of doping has to be fine-tuned in the context of charge transfer phenomena between the van der Waals materials in a heterostructure.

6. Electronic transport properties of hole doped WSe$_2$

6.1 Doping induced conducting state

Ultra-thin films of WSe$_2$ doped with Nb are grown on Al$_2$O$_3$ (001) substrates. The doping is done using an alloy target of 95% W and 5% Nb by weight which corresponds to 90% W and 10% Nb atomic ratio. This makes the WSe$_2$, doped with holes by using Nb as substitution for the W atoms due to the nominal valance of Nb being +5 instead of +4 for W.

The thickness of the thin films is estimated from the duration of the deposition as well as by using the transmission electron microscopy (TEM). The TEM images are shown for 5ML and 6ML Nb$_{0.1}$W$_{0.9}$Se$_2$ samples in the Fig. 6.1. It is clear from the TEM images that there is a pattern of bright lines which corresponds to the transition metal layer. In the case of 5ML, there seems to be a modulation of the layers compared to the 6ML sample. This is an artefact due to the orientation of the sample during the TEM measurement. In the case of 6ML, the orientation is along WSe$_2$ [110]. Such orientation allows us to view the transition metal and the chalcogenide as separate spots in high resolution TEM. The TEM images does not show such spot pattern, but the artefacts of
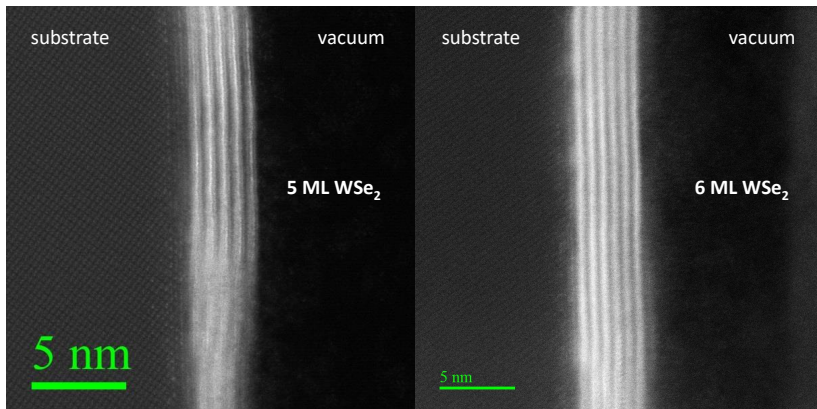
Figure 6.1: The transmission electron microscopy (TEM) images of 5ML and 6ML $Nb_{0.1}W_{0.9}Se_2$ grown on Al_2O_3 (001) substrates.
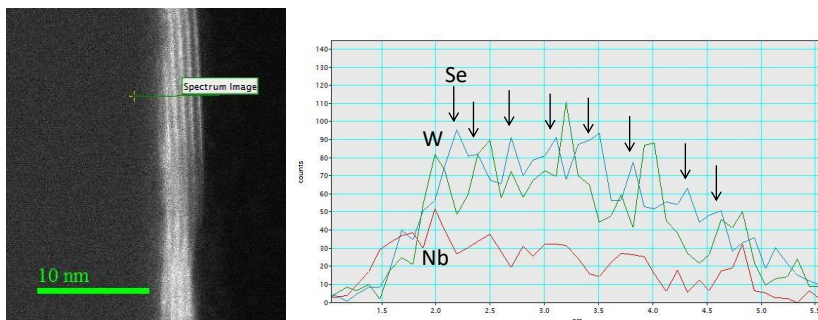
Figure 6.2: The EDX spectra of 5ML $Nb_{0.1}W_{0.9}Se_2$ showing the Nb and W peaks over each other and two Se peaks in between the transition metal peaks. The arrows indicate the position of Se atoms.

clustering seen in 5ML is eliminated. Because of the uniformity, it is inferred that there are no clustering of pure Nb and Nb is replacing the W atoms. This is confirmed by the energy-dispersive X-ray (EDX) spectroscopy, in which the Nb peaks overlap with that of the W peaks and two Se peaks are found to be in between

the transition metal peaks as shown in the Fig.6.2.
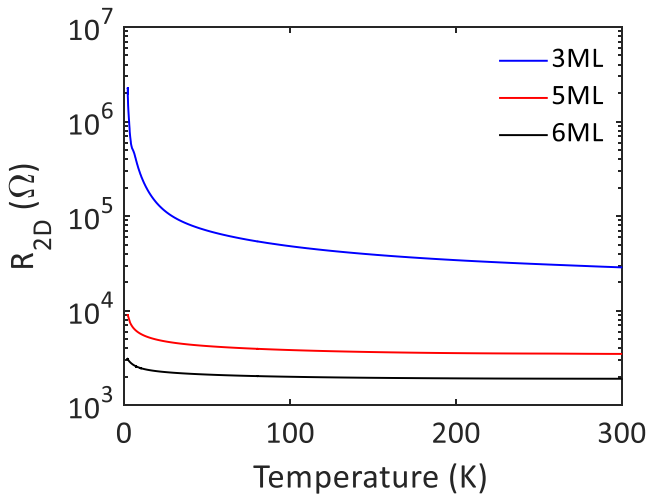
Figure 6.3: The sheet resistance of 3ML, 5ML and 6ML Nb$_{0.1}$W$_{0.9}$Se$_2$ thin films deposited on Al$_2$O$_3$ (001) substrates as a function of temperature in the absence of external magnetic field.

We discuss key observations from the measurement of resistivity versus temperature, shown in the Fig.6.3. First, the Nb doped WSe$_2$ thin films are conducting down to temperature of 2 K. Second, the resistance of the thin films increases with decreasing temperature. Third, the resistance of the thin films increases with decreasing thickness and in the case of 3ML Nb$_{0.1}$W$_{0.9}$Se$_2$, the resistance reaches an order of 10^6 Ω at 2 K. The possible reason for the increase of resistance at very low temperatures and also with decreasing thickness could be a presence of large disorder in the thin films.

In order to understand the nature of transport phenomena in our samples, we first try to find a relationship between the resistance and the temperature. As can be seen in the Fig.6.4, the resistance seems to be an exponential function of $T^{-1/4}$ in all our samples. Such trend has been discussed in [8] and originates
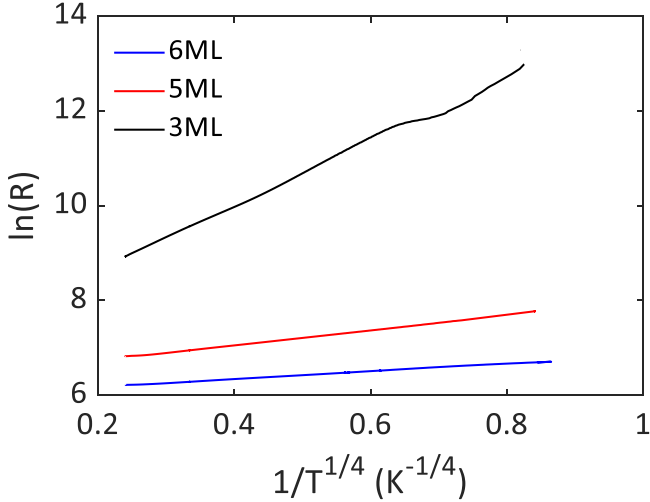
Figure 6.4: The plot of ln(R) as a function of temperature given by the Eq.6.1 for the case of 3ML, 5ML and 6ML Nb$_{0.1}$W$_{0.9}$Se$_2$.

from the following relationship between the resistivity and the temperature.

$$\rho \propto exp\left(\frac{1}{T^{1/4}}\right). \tag{6.1}$$

Such relationship is known to occur when the transport is governed by variable-range hopping process. This variable-range hopping is explained as follows. Impurity or defect sites have different potential than the rest of the material. In a classical picture, the carrier is trapped at the impurity site. Quantum mechanically, the wave function of the carrier is maximum at the impurity site and decays exponentially away from the site. Such exponential nature results in the overlap of the wave functions from different sites. This overlap leads to quantum tunnelling of the carriers between them, the energy for which is usually obtained from the thermally active weak phonons.

We used the Hall Effect to measure different parameters of
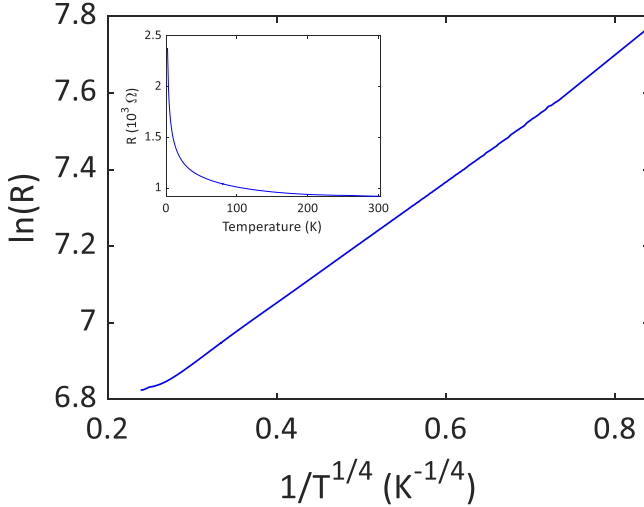
Figure 6.5: The plot of ln(R) as a function of temperature for the case of 5ML Nb$_{0.1}$W$_{0.9}$Se$_2$. The linearity suggests that the conduction process is due to *variable-range hopping*. Insert is the plot of RvT for the same sample.
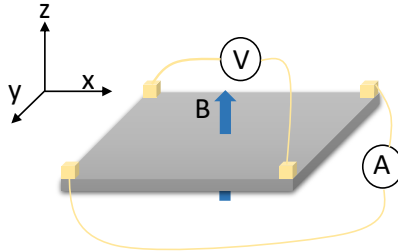
Figure 6.6: van der Pauw geometry for the measurement of Hall resistance as a function of perpendicular magnetic field at different temperatures. Four Au contacts are deposited using thermal evaporation method.

our thin films that are necessary for the estimation of relevant

length and time scales. The Hall Effect was measured using van der Pauw geometry (Fig.6.6). The measured Hall resistance is anti-symmetrised to remove any contribution of R$_{xx}$ using the following relation.

$$R_{xy} = \frac{R_{xy}(+B) - R_{xy}(-B)}{2}. \tag{6.2}$$
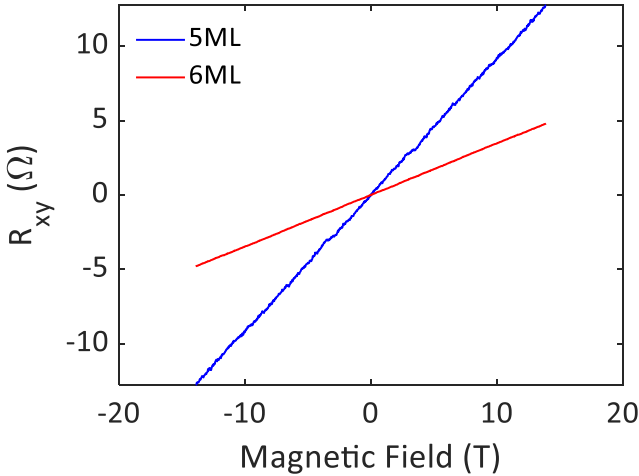
Figure 6.7: The anti-symmetrised data of 5ML and 6ML Nb doped Nb$_{0.1}$W$_{0.9}$Se$_2$ samples at 150 K. From the slope, we can see that the carrier concentration in 6ML is larger than in 5ML.

The slope of the Hall Effect was positive in all of our measured samples, indicating hole as carriers. The carrier concentration n can be calculated using the relation, $n = 1/e(\Delta R_{xy}/\Delta B)t$, where e is the charge of the electron and t is the thickness of the thin film. Our samples are found to have a carrier concentration of 2.1 $\times 10^{21}$ cm^{-3} in 5ML and 4.6 $\times 10^{21}$ cm^{-3} for 6ML Nb$_{0.1}$W$_{0.9}$Se$_2$ at 150 K.
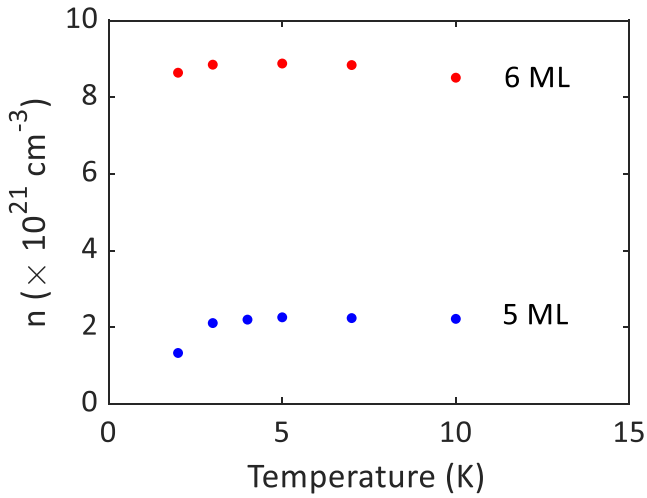
Figure 6.8: The carrier density n of $Nb_{0.1}W_{0.9}Se_2$ as a function of temperature, estimated from the Hall Effect.

Temperature (K)	5ML			6ML		
	$v_F(\times 10^8 cm/s)$	$\tau_m(fs)$	$D(cm^2/s)$	$v_F(\times 10^8 cm/s)$	$\tau_m(fs)$	$D(cm^2/s)$
2	0.878	0.408	1.57	1.64	0.156	2.08
3	1.02	0.293	1.53	1.65	0.159	2.16
4	1.04	0.312	1.68	-	-	-
5	1.05	0.324	1.78	1.65	0.170	2.32
7	1.04	0.356	1.94	1.65	0.179	2.44
10	1.04	0.391	2.12	1.63	0.195	2.59
20	1.04	0.445	2.42	1.54	0.248	2.94

Table 6.1: The numerical values of Fermi velocity (v_F), momentum relaxation time (τ_m) and the diffusion constant (D) for 5ML and 6ML Nb$_{0.1}$W$_{0.9}$Se$_2$.

With the information of the carrier concentration, the mobility of the carriers is calculated using the relation, $\mu = 1/ne\rho_{xx}(0)$, where $\rho_{xx}(0)$ is the zero field resistivity of the sample at the measured temperature. Our samples are found to have very low mobility ($\mu < 5\ cm^2v^{-1}s^{-1}$) in both 5ML and 6ML Nb$_{0.1}W_{0.9}Se_2$ thin films. The low values suggests high concentration of disorder and defects.

The estimated carrier concentration and the mobilities are used along with assumption that the effective mass of the holes is $0.45m_0$ (Ref. [142]), where m_0 is the rest mass of the electron, to calculate the Fermi momentum ($k_F = \sqrt{2\pi n}$), velocity ($v_F = \hbar k_F/m^*$) and energy ($E_F = (\hbar k_F)^2/2m^*$). The equation for E_F assumes parabolic band located at the $\boldsymbol{K}$-point in the Brillouin zone.

The momentum relaxation time τ_m is calculated using the equation $\tau_m = \mu m^*/e$. This is the time the carrier moves before losing the initial momentum due to scattering and allows us to estimate the distance the carrier moves on an average in between the scattering events, called the *mean free path* ($l = \sqrt{D\tau}$). Here, D is the diffusion constant of the charge carriers calculated using the relation, $D = v_F^2\tau_m/2$. In our case, τ_m is in the range of femtoseconds. Few important parameters in 5ML and 6ML samples at different temperatures are summarised in the Tab.6.1.

6.2   Quantum interference effects

The wave nature of the electron comes with interesting phenomena. The classical picture of transport, Drude model is described previously in Sec.2.5.1 does not involve quantum corrections. In the quantum mechanical model, the interference effects becomes important to describe the transport phenomena. Two identical paths created by scattering via impurities and are related by time-reversal symmetry (e.g., clockwise and counter clockwise) interfere constructively, leading to *weak localisation* (WL). This is because the presence of time reversal path increases the probability

for the carrier to be at the point of intersection of the clock-wise and counter clockwise paths, consequently decreasing the conductivity (increase in resistivity). This constructive interference is destroyed in the presence of strong spin-orbit interaction. In this case, the waves interfere destructively, leading to *weak anti-localisation* (WAL). This results in the increase in the conductivity (decrease in the resistance). The effects of localisation and anti-localisation are prominent in low dimensional systems compared to 3D due to increased probability for the electron to self-intersect. The key quantity which governs the quantum
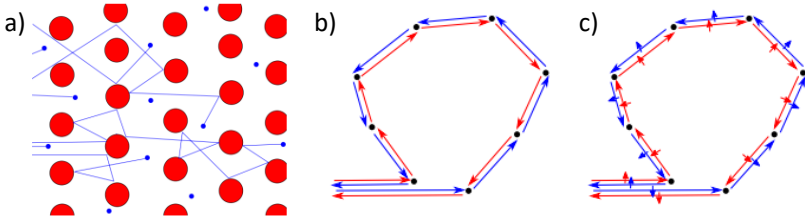
Figure 6.9: a) Classical picture of electron transport as described by the Drude model. Illustration of the quantum interference phenomena of b) weak localisation, without SOC and c) weak anti-localisation in the presence of SOC. Reproduced from Ref. [206].

interference effect is the phase coherence length l_ϕ, the distance over which the phase coherence of electron is lost. The dephasing length l_ϕ depends on many factors of the system and decreases with increasing temperature as the interaction between the electrons and phonon, for example, increases. At low temperatures, phase coherence length can be as large as a few microns, much larger than the typical mean free path of electrons.

Magnetoconductance is measured with magnetic field applied perpendicular and parallel to the current at different temperatures. We have used the expression for conductivity derived by Hikami, Larkin, and Nagaoka (HLN) [9, 10] to fit our magnetoconductance data, using *phase* relaxation length (L_ϕ) and *spin*
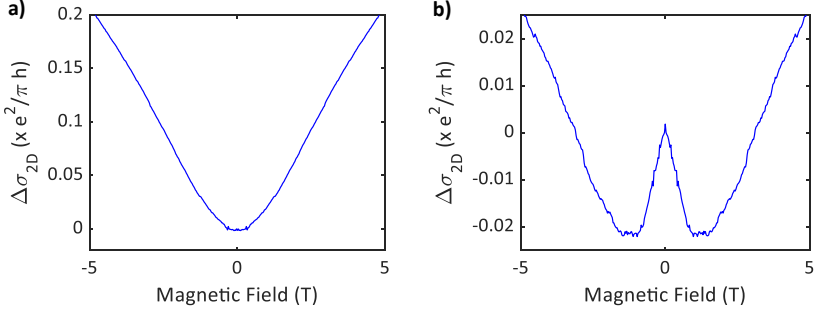
Figure 6.10: Representative plots of a) weak localisation and b) weak anti-localisation.

relaxation length (L_{so}) in the form of related magnetic field scales (B_ϕ and B_{so}) as the fitting parameters. HLN expression used to estimate the relaxation lengths is as follows,

$$\Delta\sigma(B) - \Delta\sigma(0) = \frac{1}{2}\Psi\left(\frac{1}{2} + \frac{B_\phi}{B}\right) - \frac{1}{2}log\left(\frac{B_\phi}{B}\right) - \Psi\left(\frac{1}{2} + \frac{B_\phi + B_{so}}{B}\right)$$
$$+ log\left(\frac{B_\phi + B_{so}}{B}\right) - \frac{1}{2}\Psi\left(\frac{1}{2} + \frac{B_\phi + 2B_{so}}{B}\right)$$
$$+ \frac{1}{2}log\left(\frac{B_\phi + 2B_{so}}{B}\right),$$

$$(6.3)$$

where Ψ is Digamma function. The relationship between the relaxation lengths and the characteristic magnetic fields are given by,

$$B = \frac{\hbar}{4eL^2}, \qquad (6.4)$$

where L is the L_ϕ or L_{so} and the relaxation time τ (τ_ϕ or τ_{so}) can be derived from the relation, $L = \sqrt{D\tau}$.

6.2.1 Measurement orientation: B $\perp$ I
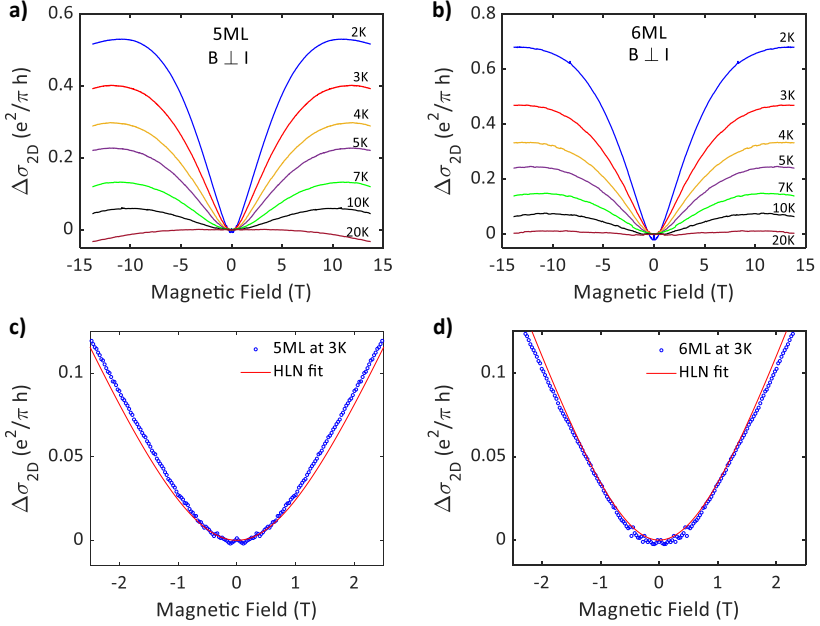
Figure 6.11: a) The conductivity of 5ML Nb$_{0.1}$W$_{0.9}$Se$_2$ grown on Al$_2$O$_3$ (001) substrate with magnetic field perpendicular to the current is plotted in the units of $(e^2/\pi h)$. b) The conductivity of 6ML Nb$_{0.1}$W$_{0.9}$Se$_2$ in the same orientation. c) Magentoconductivity at 3 K in 5ML Nb$_{0.1}$W$_{0.9}$Se$_2$, showing the *weak localisation* fitted with HLN equation. d) HLN fit for the magnetoconductivity in 6ML Nb$_{0.1}$W$_{0.9}$Se$_2$ at 3K.

In the first orientation, the magnetic field is applied perpendicular to the current and normal to the Nb$_{0.1}$W$_{0.9}$Se$_2$ [001] plane. In both 5ML and 6ML thin films, the magnitude of positive magnetoconductance is found to be maximum at the lowest temperature of 2 K and decreases with increasing temperature, with no change observed beyond 20 K. WL can be clearly seen on both the samples at different temperatures. As can be observed in the

Fig.6.12, the HLN fit gets better with increasing τ_{so} compared to τ_ϕ. For this reason we choose $\tau_{so} \to \infty$, which implies $B_{so} \to 0$ in the HLN formula given by the Eq.6.3. Using the HLN equation, relaxation length and time scales were estimated and summarised in the Tab.6.2. This means that the spin of the carrier is not dephasing in this geometry of the measurement.
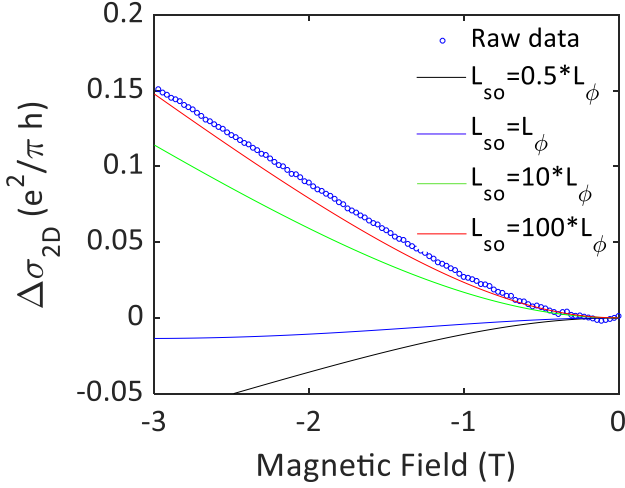
Figure 6.12: Magnetoconductance of 5ML Nb$_{0.1}$W$_{0.9}$Se$_2$ measured at 3 K with magnetic field perpendicular to the current, fitted with conductance formula of HLN theory with different ratios of relaxation lengths. The fitting gets better with increasing L_{so}. Present analysis is carried out with $L_{so} \sim 100 L_\phi$.

As explained at the start of this section, the WL arises due to the self-intersecting paths related by the time reversal symmetry in a constructive fashion. There are two ways the weak localisation feature can be destroyed. Either due to strong SOC or with an external applied magnetic field. Qualitatively, with an exception to 2 K, none of the other temperatures show any deviation from the weak localisation. A small feature near zero magnetic field in both the thin films is seen. HLN equation could

not fit properly to include this feature and ignored in our prelim-
inary analysis. The weak localisation feature is destroyed only
with magnetic field, as the phase of the wave function changes.
This suggests that there is no influence of SOC in this orientation
of the experiment. This is counter-intuitive to see no difference
between 5ML and 6ML thin films.

	5ML		6ML	
Temperature (K)	$\tau_\phi(fs)$	$\tau_{so}(fs)$	$\tau_\phi(fs)$	$\tau_{so}(fs)$
2	0.112	∞	0.109	∞
3	0.086	$''$	0.007	$''$
4	0.06	$''$		
5	0.046	$''$	0.004	$''$
7	0.029	$''$	0.003	$''$
10	0.016	$''$	0.001	$''$

Table 6.2: The numerical values of phase relaxation time (τ_ϕ) and
spin relaxation time (τ_{so}) in 5ML and 6ML Nb$_{0.1}$W$_{0.9}$Se$_2$ thin
films at different temperatures obtained from the HLN fitting of
the magnetoconductivity with magnetic field applied ***perpendic-
ular*** to the current.

6.2.2 Measurement orientation: B ∥ I

In contrast, the magnetoconductance shows WAL features when
magnetic field is applied along the direction of the current. The
calculated L_ϕ and L_{so} are found to be decreasing with increasing
temperature. The relaxation length and time scales were esti-
mated and summarised in the Tab.6.3. The fittings were not per-
fect for the case of 6ML Nb$_{0.1}$W$_{0.9}$Se$_2$ thin film compared to the
5ML. Qualitatively both the samples are observed to have similar
behaviour. Such WAL feature suggests a presence of some spin
relaxation source which acts efficiently in this magnetic field con-
figuration. This set of data is unique and has not been reported
in the literature. More detailed experiments and theoretical work
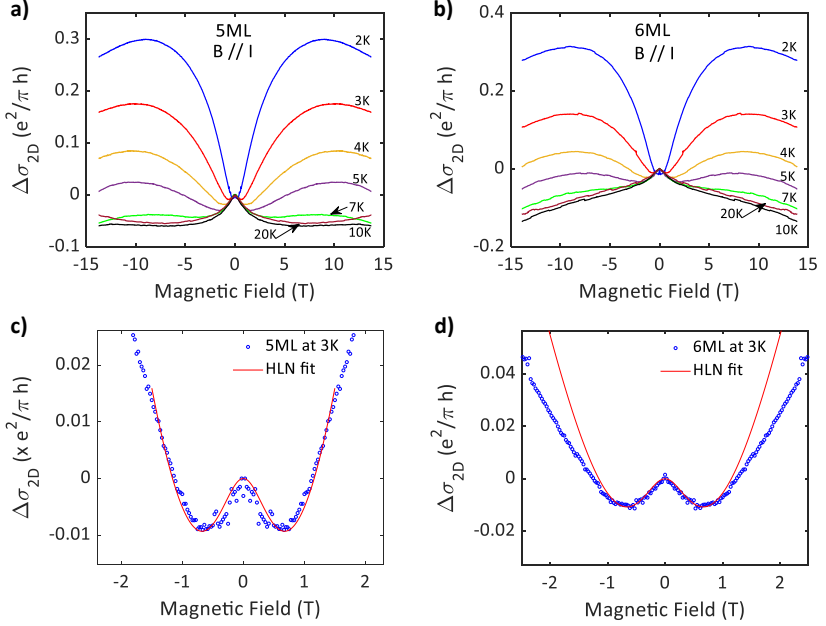
Figure 6.13: a) The conductivity in 5ML Nb$_{0.1}$W$_{0.9}$Se$_2$ grown on Al$_2$O$_3$ (001) substrate with magnetic field parallel to the current. b) The conductivity 6ML Nb$_{0.1}$W$_{0.9}$Se$_2$. c) Magentoconductivity at 3 K in 5ML Nb$_{0.1}$W$_{0.9}$Se$_2$ with HLN fitting. d) The Magento-conductivity and HLN fit at 3K in 6ML Nb$_{0.1}$W$_{0.9}$Se$_2$.

is needed to understand the present observations.

It is clear from the above results that there is a clear anisotropy in the magnetoresistance with respect to the direction of the applied magnetic field. Relevant relaxation lengths are estimated and plotted in the Figs.6.14 and 6.15.

6.3 Mechanism of spin relaxation

With the known parameters, we try to find relaxation mechanism for the spin of the carrier. There are four different mechanisms

	5ML		6ML	
Temperature (K)	$\tau_\phi(fs)$	$\tau_{so}(fs)$	$\tau_\phi(fs)$	$\tau_{so}(fs)$
2	0.523	$> \tau_\phi$	0.527	$> \tau_\phi$
3	0.33	$''$	0.254	$''$
4	0.23	0.206		
5	0.177	0.143	0.142	0.109
7	0.117	0.085	0.09	0.064

Table 6.3: The numerical values of phase relaxation time (τ_ϕ) and spin relaxation time (τ_{so}) in 5ML and 6ML Nb$_{0.1}$W$_{0.9}$Se$_2$ thin films at different temperatures obtained from the HLN fitting of the magnetoconductivity with magnetic field applied **parallel** to the current.
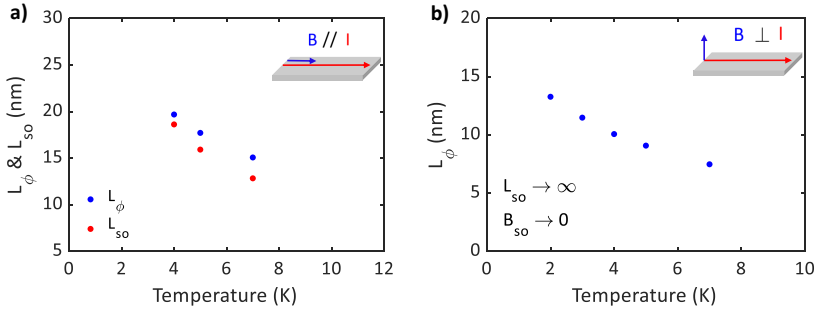
Figure 6.14: Phase and spin relaxation lengths are estimated from the HLN theory for 5ML Nb$_{0.1}$W$_{0.9}$Se$_2$. a) Relaxation lengths for magnetic field applied parallel to the current. b) The phase and spin relaxation lengths with magnetic field applied perpendicular to the current. $\tau_{so} > \tau_\phi$, in which case, τ_{so} cannot be precisely estimated. Hence a large error bar is included when $\tau_{so} > \tau_\phi$.

for the spin relaxation of the electrons in metals and semiconductors [207]. The dephasing of the spin could be a result of many different factors. They include, admixture of spin components in the electron wave function associated with scattering events,

dephasing due to the effective magnetic fields arising from broken inversion symmetry, fluctuating local magnetic fields due to electron-hole exchange and hyperfine interaction of electron spin with the nuclear moments. Among them, the first two mechanisms are described in the following.
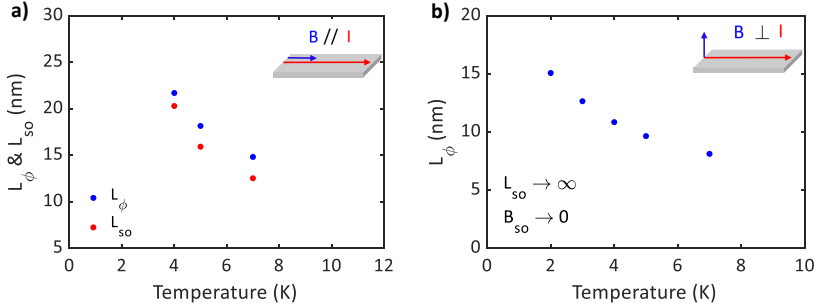
Figure 6.15: The phase and spin relaxation lengths in 6ML Nb$_{0.1}$W$_{0.9}$Se$_2$ estimated from the HLN theory. a) Relaxation lengths with magnetic field applied parallel to the current. b) The phase and spin relaxation lengths with magnetic field applied perpendicular to the current. This is almost equal to the values obtained for 5 ML sample and shown in the Fig.6.14.

6.3.1 Elliott-Yafet mechanism

The spin relaxation length is defined previously as L_{so}, which is the distance the electron travels before losing the initial spin direction. In materials with strong SOC, the electron wave function can be a mixture of both spin up and down states. However, these modified wave functions would be degenerate when both space and time reversal symmetries are present. Hence the mere presence of SOC coupling doesn't lead to spin relaxation of the electrons.

Momentum scattering arises due the collision of electrons with impurities or phonons. This idea of spin relaxation due to momentum scattering was first postulated by Elliott [208] and subse-

quent theory was extended by Yafet [209]. Qualitatively, the spin and momentum relaxations are related by the *Elliott relation* as

$$\frac{1}{\tau_{so}} \propto \frac{(\Delta g)^2}{\tau_m}, \tag{6.5}$$

where Δg is the shift in the g-factor from the free electron value of $g_0 = 2.0023$. The experimental ratio between the spin and momentum relaxations depend on finer details of the band structure, kind of impurities and the nature of symmetries present in the system.

The dependence of the spin relaxation on the temperature is given by the *Yafet relation* as

$$\frac{1}{\tau_{so}} \propto \rho(T). \tag{6.6}$$

Here $\rho(T)$ is the temperature dependent resistivity of the system under study. Quantitative relation between the relaxation lengths can be calculated using the two named relation. In addition, several approximations for the electronic and phonon band structure, the strength of the SOC, etc. are needed.

6.3.2 Dyakonov-Perel mechanism

In systems with SOC and broken inversion symmetry, the electronic wave functions are no longer degenerate. The splitting that happens in broken inversion systems are termed the Rashba effect [210] or Dresselhaus Effect in the 3D systems [211].

In the case of 2D materials and heterostructures, the space inversion symmetry is explicitly broken and leads to the Rashba Effect. With the Rashba Effect, the spin splitting of the electronic states induces an intrinsic momentum dependent magnetic field. The electron is such systems starts to precess around the magnetic field with momentum dependent Larmor frequency. The momentum dependent precession, along with momentum scattering leads to dephasing of the electron spin.

Here two different cases can be introduced to describe the nature of spin dephasing. The first case, is when the spin completes full precession before the next momentum scattering. The second case is when the spin only precesses small amount between the scattering events, which leads to random walk of the spin precession. This case is usually referred to as the Dyakonov-Perel spin relaxation mechanism [27]. The qualitative relation between the spin and momentum relaxation is as follows:

$$\frac{1}{\tau_{so}} \propto \tau_m. \tag{6.7}$$

The relationships of the spin and momentum scattering parameters is the essential difference between the Dyakonov-Perel and the Elliott-Yafet mechanisms. In the former case, the relationship is inversely proportional, while it is directly proportional in the latter case.

6.3.3   Possible mechanism of spin relaxation

In order to identify the spin relaxation mechanism, the spin relaxation time τ_{so} can be plotted with respect to the momentum relaxation time τ_m. As we can observe from the Figs.6.14 and 6.15, τ_{so} is larger than τ_ϕ when the applied magnetic field is perpendicular to the current. Since the phase of the wave function is dephasing faster than the spin direction, we can consider that the spin of carriers does not relax in this orientation. However, when the magnetic field applied parallel to the current, $\tau_\phi > \tau_{so}$, at temperatures >4 K. This set of data also shows inverse relation between τ_{so} and τ_m (Fig. 6.16). This inverse relation rules out the Elliott-Yafet mechanism and points to Dyakonov-Perel mechanism.

The gist of the transport measurements is as follows. The conductivity of the WSe$_2$ can be manipulated with Nb doping to make the thin films hole doped. The Hall Effect confirms high concentration of carriers as expected from the dopant concentration, which brings the system to degenerate semiconductor
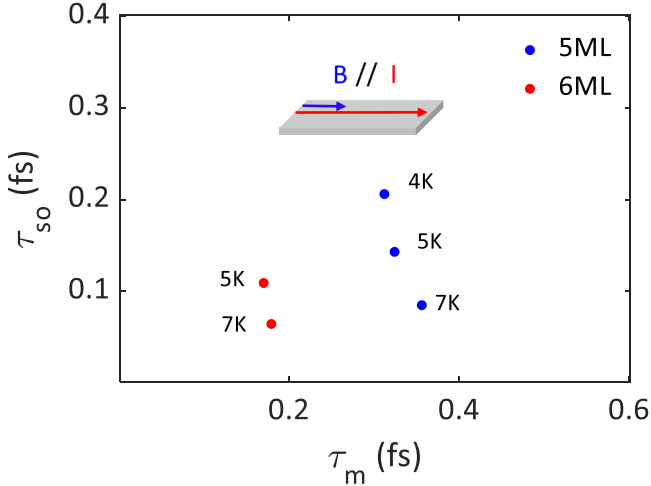
Figure 6.16: The plot between τ_{so} and τ_m in samples with nearly identical carrier densities when magnetic field is applied **parallel** to the current.

regime. The main transport mechanism of the carriers can be explained as a variable-range hopping. Magnetoresistance measurements indicate an anisotropic behaviour with respect to field direction. HLN theory is used to estimate the phase and spin relaxation lengths. Preliminary analysis hints towards Dyakonov-Perel mechanism for the spin relaxation of the carriers in our thin films. Further detailed work, both theoretical and experimental, is needed to understand the nature of spin dynamics in p-doped WSe$_2$.

Summary

We have successfully demonstrated the manipulation of Fermi level in WSe$_2$ thin films using Nb. The usual insulating state of WSe$_2$ thin films was changed to conducting down to the temperature of

2 K suggesting a metal-insulator transition. The carrier concentration is consistent with the percentage of the Nb present in the target. This suggests that the doping of the WSe$_2$ can be fine-tuned using different targets with different amounts of Nb. This is a significant step in the growth of TMDCs with feasibility of efficient doping with ease. Unlike other techniques such as gating used to manipulate the Fermi level, doping allowed us to investigate the carrier properties in pristine WSe$_2$ thin films without spatial symmetry breaking electric fields from the gate.

Moreover, clear anisotropy in the magnetoconductance has been observed. The spin dephasing time was found to be long compared to phase coherence time when the magnetic field is applied perpendicular to the current. This feature could be exploited in the field of spintronics. However, conventional localization analysis gave much shorter spin dephasing length when the magnetic field is applied parallel to the current. Such field-orientation dependent magnetotransport has been observed for the first time in doped WSe$_2$. The origin of this behaviour needs to be clarified in the future.

7. Conclusion and Afterword

Potential saturation of the silicon technology and problems aris-
ing due to miniaturisation that our society could face in the near
future encourages us to explore new type of nano-electronic mate-
rials. Although graphene is known to show interesting electronic
and mechanical properties, its use in next generation electronics
is limited due to the absence of a band gap. TMDCs are stepping
up to fill the gap left by graphene. Not only does TMDCs have
a band gap, but the lack of inversion symmetry in the monolayer
and strong SOC opens up new possibilities in low dimensional
physics and device applications. Among them, of ML WSe_2 is
particularly fascinating due to the largest spin splitting in the
valance band that could be utilised in the field of spintronics.
Moreover, the large spin splitting allows to access the spin po-
larised bands to induce exotic electronic properties by coupling
with other electronic phases such as proximity induced supercon-
ductivity.

Let me remind our motivation for this thesis work here. Al-
though a lot of work is ongoing in the field of low dimensional
TMDCs, a few important details are missing. There was a spec-
ulation about the strain in the ML WSe_2 as a reason for large
variation in the spin splitting of the valance band among ARPES
studies. However, the precise values for the strain is missing
to compliment the ARPES data. Moreover, much of electronic

transport properties were limited to the behaviour of the resistivity as a function of temperature and gate voltages. Optical experiments provided the information about the spin and valley lifetime, but systematic study via transport regarding relaxation times was needed to understand the spin properties in the low dimensional TMDCs, especially in the case of hole doped WSe_2. Utilising our new method to synthesise high quality WSe_2 thin films including monolayers, which also provides an efficient doping mechanism, we aimed at addressing these open questions.

In this thesis, we demonstrated a method of h-PLD for the synthesis of high quality WSe_2 thin films down to the monolayer limit. The limitations of the other methods were overcome with our h-PLD method to synthesise ML WSe_2 and can be extended for the growth of other TMDCs. The advantages of our method are the bottom up approach in an ultra-high vacuum and the ease of doping with different elements. The bottom up approach resulted in the locking of the crystallographic axes over macroscopic (10×10 mm^2) dimensions. Such a feature facilitates the use of high precision diffraction experiments, which is absent in mechanically exfoliated samples. Moreover, the ultra-high vacuum of the growth chamber keeps the surface pristine. This is a significant advantage for surface sensitive experiments such as ARPES. The Fermi level could be manipulated efficiently by doping with a different element without complications. Moreover, we provided evidence of fabricating a van der Waals heterostructure of ML WSe_2 on graphene.

Grown thin films allowed us to measure the precise structural properties down to the monolayer. Importantly, the locked crystallographic axes allowed us to perform high precision synchrotron based diffraction experiments for the structural characterisation. An epitaxial relationship between the ML WSe_2 and the substrates is uncovered. Furthermore, quantitative value of compressive strain is found in the grown ML WSe_2 on two important substrates, graphene and sapphire.

Exploiting the locked crystallographic axes, spin splitting of

the valance band at the **K**-point has been clearly observed in the ARPES as predicted by the theory. The spin splitting in the ML WSe_2 suggests the absence of inversion symmetry, thereby the confirming the crystal structure found in the diffraction experiments. The combination of the results from XRD and ARPES along with the first principles calculations allowed us to create a phase space of strain and spin splitting. This phase space will be useful in the future to tailor the opto-electronic properties. In addition, we uncovered charge transfer between the MLG and ML WSe_2. This resulted in n-doping of the ML WSe_2. This is a crucial information necessary to manipulate the Fermi level in van der Waals heterostructures. This is especially important in the case of heterostructure of ML WSe_2 and superconducting $NbSe_2$ to realise exotic pairing using the proximity effect, because the hole doping needs to be fine-tuned in the presence of charge transfer in between the van der Waals materials.

We have demonstrated the manipulation of the Fermi level using chemical (Nb) doping. The usual insulating state of WSe_2 thin films was changed to conducting down to the temperature of 2 K suggesting an insulator to metal transition. This is a significant step in the growth of TMDCs with a feasibility of efficient doping. Unlike other techniques such as gating used to manipulate the Fermi level, doping allowed us to investigate the spin properties in WSe_2 environment without additional symmetry-breaking component arising from electric fields. Clear anisotropy in the magnetoconductance with respect to magnetic field orientation has been observed. The spin dephasing time was found to be long compared to phase coherence time when the magnetic field is applied perpendicular to the current. This feature could be exploited in the field of spintronics, where the spin currents are required to be robust against scattering at least on the length scales of the distance between the electrodes. However, conventional localization analysis gave much shorter spin dephasing length when the magnetic field is applied parallel to the current. Such field-orientation dependent magnetotransport has been observed for

the first time in doped WSe_2. The origin of this behaviour needs to be clarified in the future.

Immediate future step should be complete understanding of the spin dynamics of the charge carrier in the doped thin films. The amount of doping needs to be fine-tuned to adjust the Fermi level. As we have observed in our transport experiments, there is a huge anisotropy in the magnetoconductivity depending on the direction of the applied magnetic field. It is highly desirable to repeat magnetoconductivity experiments in gated samples. Such study of the carrier dynamics in a gated WSe_2 thin film would allow us to understand the effects of gating on the physics of the carriers compared to the doped WSe_2 thin films.

This present work is part of a bigger agenda to realise the topological superconductivity. We have already demonstrated the fabrication of prototypical heterostructure of ML WSe_2 on MLG. The next step is to make a heterostructure of ML WSe_2 on $NbSe_2$. This system combines a non-centrosymmetric material to a conventional BCS superconductor. With the manipulation of the Fermi level to access the spin split valance bands, superconductivity due to proximity effect is expected to be observed. Moreover, due to the spin polarisation of the bands, two types of Cooper pairing are expected to arise: inter-valley zero center of mass Cooper pairs and intra-valley non-zero center of mass Cooper pairs, which are known to be exotic FFLO pairing [72].

The nature and physics of emergent fields is also quite an interesting field to explore using WSe_2. If we are successful in the fabrication of ML WSe_2 on different substrates with proper experimental geometry and measuring electrodes, we might be able to venture into realm of new physics of emergent gauge fields. These gauge fields are proposed be originating in the breaking of mirror symmetry due to ripples and corrugations of the monolayer. Such studies have been undertaken in the case of graphene [110, 111], but not yet reported concretely in TMDCs [78].

To conclude, we believe that our new approach of synthesis would extend the scope of physics and applications of TMDCs.

There are three significant achievements in this thesis work. (1) We demonstrated a new method to synthesise WSe$_2$ thin films down to monolayers with a bottom up approach. The detailed structural (XRD/GIXRD) and electronic (ARPES) characterisation of the ML WSe$_2$ would not have been possible with exfoliated samples for following reasons. In an exfoliated thin film, the lattice orientation is arbitrary compared to that of epitaxial thin films and the limited size of the crystal will make it very difficult to apply GIXRD, where the beam size typically spreads > 10 mm in the grazing incidence geometry. The epitaxial nature also creates a reference frame to align the sample in high precision synchrotron based experiments. (2) Using GIXRD and ARPES, precise structural and electronic properties are measured. This experimental data is compared with our thorough first-principles band calculations incorporating a strain effect. This enabled us to clarify that the strain effect on the spin splitting in our epitaxial WSe$_2$ is negligibly small. Our results comprise the first experimental reference in which both spin splitting value and strain was clarified with high accuracy. (3) The Fermi level in a few atomic layer WSe$_2$ was controlled by doping to induce an insulator to metal transition. Our h-PLD simplified the doping to vary the Fermi level to a desired position. We believe that the chemical doping could be advantageous compared to gating for our purpose because of two reasons. First, the electric field from the gate breaks the spatial symmetry in a different way compared to that coming from monolayer structure. Second, the gating electrode blocks the access to the ML WSe$_2$ in future STM/STS experiments which will be the most promising technique to probe the novel superconducting pairing. Therefore we believe that the synthesis and doping of van der Waals material demonstrated in this thesis could open a door to create artificial heterostructures,in a way most suitable for the future study of the physics that may appear at vdW interfaces.

Appendices

A. Experimental procedure for using h-PLD

A step by step procedure for the deposition of thin films using h-PLD

1. Close the shutter of the Se effusion cell.

2. Ramp up the temperature of the effusion cell to the required value.

3. Bring in the QCM to the measuring position.

4. After reaching the temperature in the step 2, wait for 15 minutes.

5. Open the effusion cell shutter and measure the Se flux in steps of 5 minutes and calculate the average flux over next 15 minutes.

6. Close the effusion cell shutter and take out the QCM.

7. Load the substrate in the substrate heater.

8. Program the substrate temperature controller.

9. Ramp up the temperature of the substrate to the deposition temperature.

10. Capture the RHEED images of the bare substrate at the deposition temperature.

11. Close the laser window and adjust the laser parameters.

12. Check the target and start the laser with opened laser window.

13. Open the effusion cell shutter.

14. Wait for the deposition to finish.

15. Capture the RHEED images at the end of deposition.

16. Depending on the experiments planned with the sample, cap the thin film with Se.

17. Wait for the temperature controllers to end the program.

18. Wait for the sample to cool down to the room temperature.

This requires us to have the substrate at optimal temperature during deposition and anneal at higher temperatures to improve the crystallinity under chemical pressure. In order to maintain the required temperature of the substrate, the substrate heater is calibrated using a pyrometer. The temperature of the substrate heater is controlled by a k-type thermocouple. To calibrate the substrate heater, the emissivity of the substrate are needed. For this reason, we first measured the emissivity of the substrates using a blackbody calibrated pyrometer. The substrates are heated to certain temperature and the emissivity is adjusted to read the temperature value using pyrometer same as that of thermocouple placed just under the substrate in the heating chamber.

B. Calibration of substrate heater

To calibrate the substrate heater, the emissivity of the substrate are needed. For this reason, we first measured the emissivity of the substrates using a blackbody calibrated pyrometer. The substrates are heated to certain temperature and the emissivity is adjusted to read the temperature value using pyrometer same as that of thermocouple placed just under the substrate in the heating chamber.
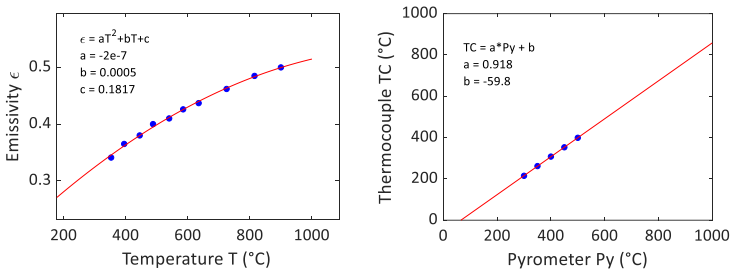
Figure B.1: Measurement of the emissivity of SiC substrates on which MLG is epitaxially grown using pyrometer.

Once the emissivity is measured at different temperatures, the data is fitted with polynomial curve fitting to extract the emissivity of the substrates at the required temperatures. Using this information, the substrate heater of the PLD chamber is calibrated using a pyrometer to known emissivities of the substrates. The temperature of the substrate heater is controlled by a Type-R
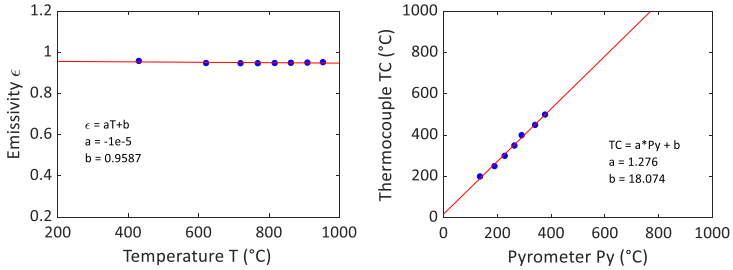
Figure B.2: Measurement of the emissivity of Al_2O_3 substrates before calibrating the heater using pyrometer.

thermocouple.
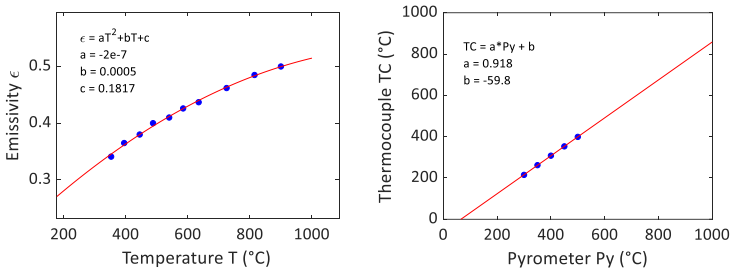
Figure B.3: Measurement of the emissivity of SiC substrates on which MLG is epitaxially grown using pyrometer.

Once the emissivity is measured at different temperatures, the data is fitted with polynomial curve fitting to extract the emissivity of the substrates at the required temperatures. Using this information, the substrate heater of the PLD chamber is calibrated using a pyrometer to known emissivities of the substrates.

Once the substrate heater is calibrated, we need to optimise other parameters that influence the growth of the WSe_2 thin films. During the early period of this thesis work, many components were missing and the optimisation has to be done in an improvised way. In the absence of direct measurement of the required parameters, we relied on indirect inferences from other experi-
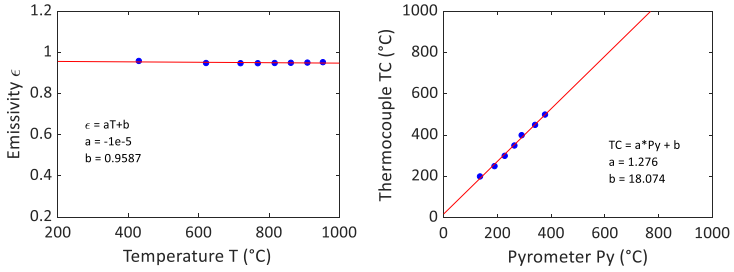
Figure B.4: Measurement of the emissivity of Al_2O_3 substrates before calibrating the heater using pyrometer.

ments.

C. Band structure of strained mono-layer WSe$_2$
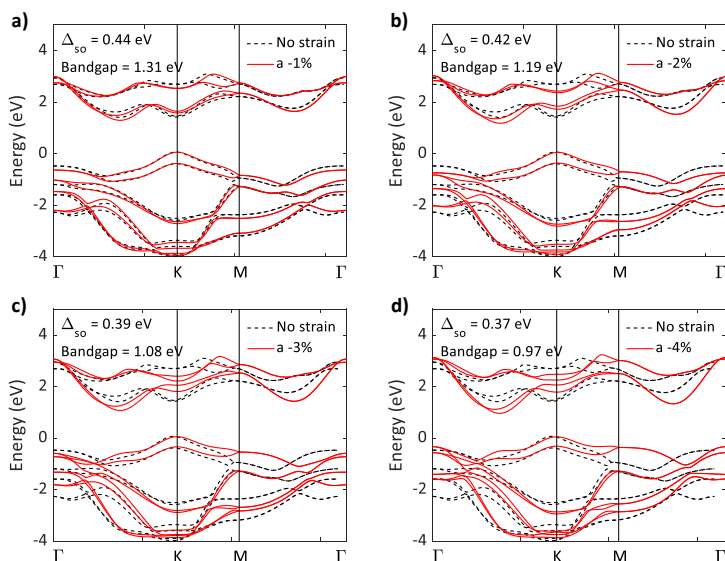
Figure C.1: Band structure calculated for strained ML WSe$_2$. a) -1%, b) -2%, c) -3% and d) -4%.
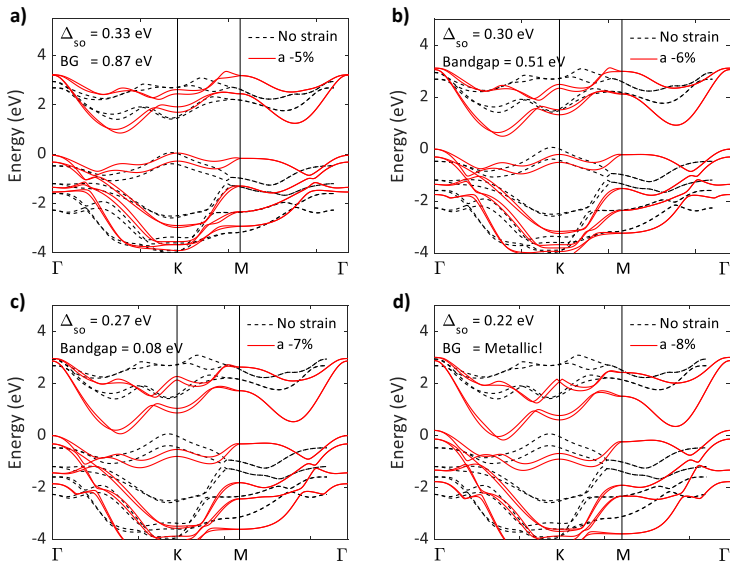
Figure C.2: Band structure calculated for strained ML WSe$_2$. a) -5%, b) -6%, c) -7% and d) -8%.
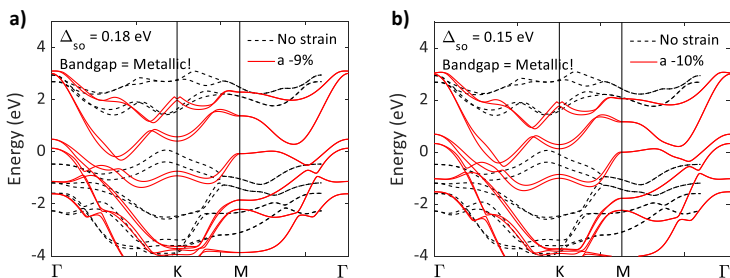
Figure C.3: Band structure calculated for strained ML WSe$_2$. a) -9% and b) -10%.
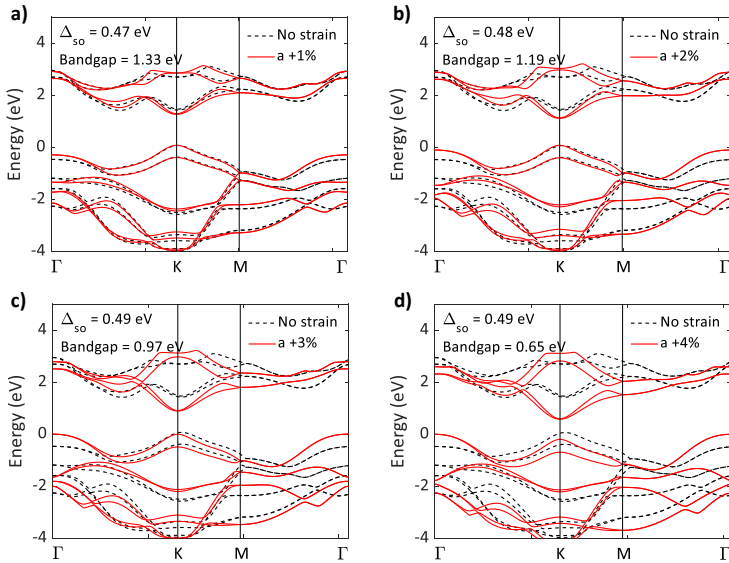
Figure C.4: Band structure calculated for strained ML WSe$_2$. a) +1%, b) +2%, c) +3% and d) +4%.
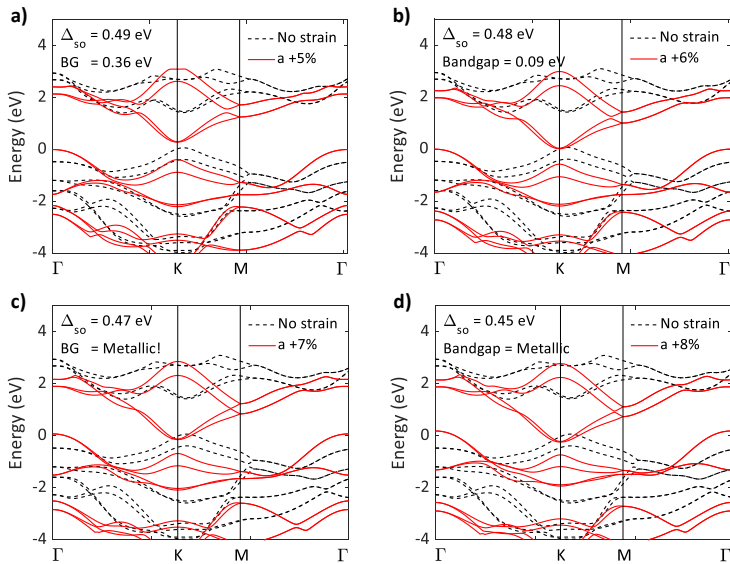
Figure C.5: Band structure calculated for strained ML WSe$_2$. a) +5%, b) +6%, c) +7% and d) +8%.
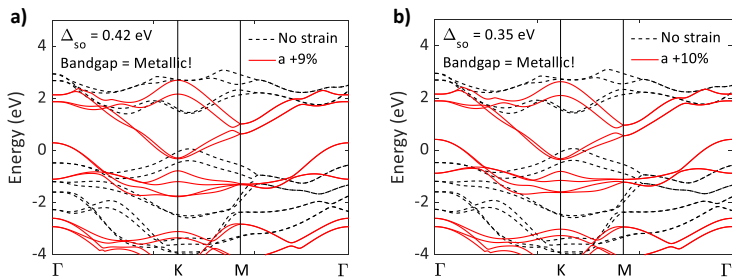
Figure C.6: Band structure calculated for strained ML WSe$_2$. a) +9% and b) +10%.

Bibliography

[1] Andre Konstantin Geim. Graphene: status and prospects. *science*, 324(5934):1530–1534, 2009.

[2] AH Castro Neto, Francisco Guinea, Nuno MR Peres, Kostya S Novoselov, and Andre K Geim. The electronic properties of graphene. *Reviews of modern physics*, 81(1):109, 2009.

[3] AK Geim and IV Grigorieva. Van der Waals heterostructures. *Nature*, 499(7459):419, 2013.

[4] KS Novoselov, A Mishchenko, A Carvalho, and AH Castro Neto. 2D materials and van der Waals heterostructures. *Science*, 353(6298):aac9439, 2016.

[5] Ruitao Lv, Joshua A Robinson, Raymond E Schaak, Du Sun, Yifan Sun, Thomas E Mallouk, and Mauricio Terrones. Transition metal dichalcogenides and beyond: synthesis, properties, and applications of single-and few-layer nanosheets. *Accounts of chemical research*, 48(1):56–64, 2014.

[6] Kin Fai Mak and Jie Shan. Photonics and optoelectronics of 2D semiconductor transition metal dichalcogenides. *Nature Photonics*, 10(4):216, 2016.

[7] Yi Zhang, Miguel M Ugeda, Chenhao Jin, Su-Fei Shi, Aaron J Bradley, Ana Martín-Recio, Hyejin Ryu, Jonghwan Kim, Shujie Tang, Yeongkwan Kim, et al. Electronic structure, surface doping, and optical response in epitaxial WSe$_2$ thin films. *Nano letters*, 16(4):2485–2491, 2016.

[8] Nevill Francis Mott. Conduction in non-crystalline materials: III. Localized states in a pseudogap and near extremities of conduction and valence bands. *Philosophical Magazine*, 19(160):835–852, 1969.

[9] Shinobu Hikami, Anatoly I Larkin, and Yosuke Nagaoka. Spin-orbit interaction and magnetoresistance in the two dimensional random system. *Progress of Theoretical Physics*, 63(2):707–710, 1980.

[10] W Knap, C Skierbiszewski, A Zduniak, E Litwin-Staszewska, D Bertho, F Kobbi, JL Robert, GE Pikus, FG Pikus, SV Iordanskii, et al. Weak antilocalization and spin precession in quantum wells. *Physical Review B*, 53(7):3912, 1996.

[11] Bill Holt. The dawn of the silicon age. *Physics World*, 1(12):39, 1988.

[12] Ian M Ross. The foundation of the silicon age. *Bell Labs Technical Journal*, 2(4):3–14, 1997.

[13] Gordon E Moore et al. Cramming more components onto integrated circuits, 1965.

[14] Robert R Schaller. Moore's law: past, present and future. *IEEE spectrum*, 34(6):52–59, 1997.

[15] Qing Hua Wang, Kourosh Kalantar-Zadeh, Andras Kis, Jonathan N Coleman, and Michael S Strano. Electronics and optoelectronics of two-dimensional transition metal dichalcogenides. *Nature nanotechnology*, 7(11):699, 2012.

[16] SA Wolf, DD Awschalom, RA Buhrman, JM Daughton, S Von Molnar, ML Roukes, A Yu Chtchelkanova, and DM Treger. Spintronics: a spin-based electronics vision for the future. *science*, 294(5546):1488–1495, 2001.

[17] Stuart A Wolf, Almadena Yu Chtchelkanova, and Daryl M Treger. Spintronics—A retrospective and perspective. *IBM Journal of Research and Development*, 50(1):101–110, 2006.

[18] Behtash Behin-Aein, Deepanjan Datta, Sayeef Salahuddin, and Supriyo Datta. Proposal for an all-spin logic device with built-in memory. *Nature nanotechnology*, 5(4):266, 2010.

[19] Li Su, Youguang Zhang, Jacques-Olivier Klein, Yue Zhang, Arnaud Bournel, Albert Fert, and Weisheng Zhao. Current-limiting challenges for all-spin logic devices. *Scientific reports*, 5:14905, 2015.

[20] JW Lu, E Chen, M Kabir, MR Stan, and SA Wolf. Spintronics technology: past, present and future. *International Materials Reviews*, 61(7):456–472, 2016.

[21] Sabpreet Bhatti, Rachid Sbiaa, Atsufumi Hirohata, Hideo Ohno, Shunsuke Fukami, and SN Piramanayagam. Spintronics based random access memory: a review. *Materials Today*, 20(9):530–548, 2017.

[22] Supriyo Datta and Biswajit Das. Electronic analog of the electro-optic modulator. *Applied Physics Letters*, 56(7):665–667, 1990.

[23] Hongtao Yuan, Mohammad Saeed Bahramy, Kazuhiro Morimoto, Sanfeng Wu, Kentaro Nomura, Bohm-Jung Yang, Hidekazu Shimotani, Ryuji Suzuki, Minglin Toh, Christian Kloc, et al. Zeeman-type spin splitting controlled by an electric field. *Nature Physics*, 9(9):563, 2013.

[24] JM Lu, O Zheliuk, Inge Leermakers, Noah FQ Yuan, Uli Zeitler, Kam Tuen Law, and JT Ye. Evidence for two-dimensional ising superconductivity in gated MoS_2. *Science*, 350(6266):1353–1357, 2015.

[25] Benjamin T Zhou, Noah FQ Yuan, Hong-Liang Jiang, and Kam Tuen Law. Ising superconductivity and Majorana fermions in transition-metal dichalcogenides. *Physical Review B*, 93(18):180501, 2016.

[26] ZY Zhu, YC Cheng, and Udo Schwingenschlögl. Giant spin-orbit-induced spin splitting in two-dimensional transition-metal dichalcogenide semiconductors. *Physical Review B*, 84(15):153402, 2011.

[27] MI Dyakonov and VI Perel. Spin relaxation of conduction electrons in noncentrosymmetric semiconductors. *Soviet Physics Solid State, Ussr*, 13(12):3023–3026, 1972.

[28] H Schmidt, I Yudhistira, L Chu, AH Castro Neto, B Özyilmaz, S Adam, and G Eda. Quantum transport and observation of D′yakonov-Perel spin-orbit scattering in monolayer MoS_2. *Physical review letters*, 116(4):046803, 2016.

[29] Michael A Morse. Craniology and the adoption of the Three-Age System in Britain. In *Proceedings of the Prehistoric Society*, volume 65, pages 1–16. Cambridge University Press, 1999.

[30] Robert F Heizer. The background of Thomsen's three-age system. *Technology and Culture*, 3(3):259–266, 1962.

[31] Philip Ball. *The Elements: a very short introduction*. Oxford University Press, 2004.

[32] D Frank-Kamenetskii. *Plasma: the fourth state of matter*. Springer Science & Business Media, 2012.

[33] Werner Buckel and Reinhold Kleiner. *Superconductivity: fundamentals and applications*. John Wiley & Sons, 2008.

[34] Michael Tinkham. *Introduction to superconductivity*. Courier Corporation, 2004.

[35] J Robert Schrieffer. *Theory of superconductivity*. CRC Press, 2018.

[36] Boris V Svistunov, Egor S Babaev, and Nikolay V Prokof'ev. *Superfluid states of matter*. Crc Press, 2015.

[37] John Whitfield. Molecules form new state of matter. Nov 2003.

[38] Gayle Swenson. Bose-einstein condensate: A new form of matter. https://www.nist.gov/news-events/news/2001/10/bose-einstein-condensate-new-form-matter, Nov 2017.

[39] Joel E Moore. The birth of topological insulators. *Nature*, 464(7286):194, 2010.

[40] TO Wehling, Annica M Black-Schaffer, and Alexander V Balatsky. Dirac materials. *Advances in Physics*, 63(1):1–76, 2014.

[41] Binghai Yan and Claudia Felser. Topological materials: Weyl semimetals. *Annual Review of Condensed Matter Physics*, 8:337–354, 2017.

[42] Shengyuan A Yang. Dirac and Weyl Materials: Fundamental Aspects and Some Spintronics Applications. In *Spin*, volume 6, page 1640003. World Scientific, 2016.

[43] MG Vergniory, L Elcoro, Claudia Felser, Nicolas Regnault, B Andrei Bernevig, and Zhijun Wang. A complete catalogue of high-quality topological materials. *Nature*, 566(7745):480, 2019.

[44] Tiantian Zhang, Yi Jiang, Zhida Song, He Huang, Yuqing He, Zhong Fang, Hongming Weng, and Chen Fang. Catalogue of topological electronic materials. *Nature*, 566(7745):475, 2019.

[45] Michel Julliere. Tunneling between ferromagnetic films. *Physics letters A*, 54(3):225–226, 1975.

[46] Mario Norberto Baibich, Jean Marc Broto, Albert Fert, F Nguyen Van Dau, Frédéric Petroff, P Etienne, G Creuzet, A Friederich, and J Chazelas. Giant magnetoresistance of (001) Fe/(001) Cr magnetic superlattices. *Physical review letters*, 61(21):2472, 1988.

[47] Grünberg Binasch, Peter Grünberg, F Saurenbach, and W Zinn. Enhanced magnetoresistance in layered magnetic structures with antiferromagnetic interlayer exchange. *Physical review B*, 39(7):4828, 1989.

[48] MA Cazalilla, H Ochoa, and F Guinea. Quantum spin Hall effect in two-dimensional crystals of transition-metal dichalcogenides. *Physical review letters*, 113(7):077201, 2014.

[49] Per Joensen, RF Frindt, and S Roy Morrison. Single-layer MoS_2. *Materials research bulletin*, 21(4):457–461, 1986.

[50] Kostya S Novoselov, Andre K Geim, Sergei V Morozov, DA Jiang, Y_ Zhang, Sergey V Dubonos, Irina V Grigorieva, and Alexandr A Firsov. Electric field effect in atomically thin carbon films. *science*, 306(5696):666–669, 2004.

[51] KS Novoselov, D Jiang, F Schedin, TJ Booth, VV Khotkevich, SV Morozov, and AK Geim. Two-dimensional atomic crystals. *Proceedings of the National Academy of Sciences*, 102(30):10451–10453, 2005.

[52] Deep Jariwala, Vinod K Sangwan, Lincoln J Lauhon, Tobin J Marks, and Mark C Hersam. Emerging device applications for semiconducting two-dimensional transition metal dichalcogenides. *ACS nano*, 8(2):1102–1120, 2014.

[53] Andrew J Mannix, Brian Kiraly, Mark C Hersam, and Nathan P Guisinger. Synthesis and chemistry of elemental 2D materials. *Nature Reviews Chemistry*, 1(2):0014, 2017.

[54] Yuan Liu, Nathan O Weiss, Xidong Duan, Hung-Chieh Cheng, Yu Huang, and Xiangfeng Duan. Van der Waals heterostructures and devices. *Nature Reviews Materials*, 1(9):16042, 2016.

[55] Manish Chhowalla, Hyeon Suk Shin, Goki Eda, Lain-Jong Li, Kian Ping Loh, and Hua Zhang. The chemistry of two-dimensional layered transition metal dichalcogenide nanosheets. *Nature chemistry*, 5(4):263, 2013.

[56] Alexander V Kolobov and Junji Tominaga. *Two-Dimensional Transition-Metal Dichalcogenides*, volume 239. Springer, 2016.

[57] Joshua Golden, Melissa McMillan, Robert T Downs, Grethe Hystad, Ian Goldstein, Holly J Stein, Aaron Zimmerman, Dimitri A Sverjensky, John T Armstrong, and Robert M Hazen. Rhenium variations in molybdenite (MoS_2): Evidence for progressive subsurface oxidation. *Earth and Planetary Science Letters*, 366:1–5, 2013.

[58] Jl A Wilson and AD Yoffe. The transition metal dichalcogenides discussion and interpretation of the observed optical, electrical and structural properties. *Advances in Physics*, 18(73):193–335, 1969.

[59] WJ Schutte, JL De Boer, and F Jellinek. Crystal structures of tungsten disulfide and diselenide. *Journal of Solid State Chemistry*, 70(2):207–209, 1987.

[60] V Yu Fominski, VN Nevolin, RI Romanov, VI Titov, and W Scharff. Tribological properties of pulsed laser deposited WSe_x (Ni)/DLC coatings. *Tribology Letters*, 17(2):289–294, 2004.

[61] JJ Hu, JS Zabinski, JE Bultman, JH Sanders, and AA Voevodin. Structure characterization of pulsed laser deposited MoS_x–WSe_y composite films of tribological interests. *Tribology Letters*, 24(2):127–135, 2006.

[62] AA Voevodin, JP O'neill, and JS Zabinski. Nanocomposite tribological coatings for aerospace applications. *Surface and Coatings Technology*, 116:36–45, 1999.

[63] SN Grigoriev, V Yu Fominski, RI Romanov, and MA Volosova. Structural modification and tribological behavior improvement of solid lubricating WSe_x coatings during pulsed laser deposition in buffer He-gas. *Journal of Friction and Wear*, 34(4):262–269, 2013.

[64] Sivacarendran Balendhran, Sumeet Walia, Hussein Nili, Jian Zhen Ou, Serge Zhuiykov, Richard B Kaner, Sharath Sriram, Madhu Bhaskaran, and Kourosh Kalantar-zadeh. Two-dimensional molybdenum trioxide and dichalcogenides. *Advanced Functional Materials*, 23(32):3952–3970, 2013.

[65] Sheneve Z Butler, Shawna M Hollen, Linyou Cao, Yi Cui, Jay A Gupta, Humberto R Gutiérrez, Tony F Heinz, Seung Sae Hong, Jiaxing Huang, Ariel F Ismach, et al. Progress, challenges, and opportunities in two-dimensional materials beyond graphene. *ACS nano*, 7(4):2898–2926, 2013.

[66] P Chen, Woei Wu Pai, Y-H Chan, W-L Sun, C-Z Xu, D-S Lin, MY Chou, A-V Fedorov, and T-C Chiang. Large quantum-spin-Hall gap in single-layer $1T'$ WSe_2. *Nature communications*, 9, 2018.

[67] Soohyun Cho, Jin-Hong Park, Jisook Hong, Jongkeun Jung, Beom Seo Kim, Garam Han, Wonshik Kyung, Yeongkwan Kim, S-K Mo, JD Denlinger, et al. Experimental Observation of Hidden Berry Curvature in Inversion-Symmetric Bulk 2H-WSe$_2$. *Physical review letters*, 121(18):186401, 2018.

[68] Ali Eftekhari. Tungsten dichalcogenides (WS$_2$, WSe$_2$, and WTe$_2$): materials chemistry and applications. *Journal of Materials Chemistry A*, 5(35):18299–18325, 2017.

[69] Mahdi Ghorbani-Asl, Stefano Borini, Agnieszka Kuc, and Thomas Heine. Strain-dependent modulation of conductivity in single-layer transition-metal dichalcogenides. *Physical Review B*, 87(23):235434, 2013.

[70] Martin Gmitra and Jaroslav Fabian. Proximity Effects in Bilayer Graphene on Monolayer WSe$_2$: Field-Effect Spin Valley Locking, Spin-Orbit Valve, and Spin Transistor. *Physical review letters*, 119(14):146401, 2017.

[71] Cheng Gong, Hengji Zhang, Weihua Wang, Luigi Colombo, Robert M Wallace, and Kyeongjae Cho. Band alignment of two-dimensional transition metal dichalcogenides: Application in tunnel field effect transistors. *Applied Physics Letters*, 103(5):053513, 2013.

[72] Yi-Ting Hsu, Abolhassan Vaezi, Mark H Fischer, and Eun-Ah Kim. Topological superconductivity in monolayer transition metal dichalcogenides. *Nature communications*, 8:14985, 2017.

[73] Andor Kormányos, Viktor Zólyomi, Neil D Drummond, and Guido Burkard. Spin-orbit coupling, quantum dots, and qubits in monolayer transition metal dichalcogenides. *Physical Review X*, 4(1):011034, 2014.

[74] Kin Fai Mak, Kathryn L McGill, Jiwoong Park, and Paul L McEuen. The valley hall effect in MoS_2 transistors. *Science*, 344(6191):1489–1492, 2014.

[75] Sajedeh Manzeli, Dmitry Ovchinnikov, Diego Pasquier, Oleg V Yazyev, and Andras Kis. 2D transition metal dichalcogenides. *Nature Reviews Materials*, 2(8):17033, 2017.

[76] Yasuharu Nakamura and Youichi Yanase. Odd-parity superconductivity in bilayer transition metal dichalcogenides. *Physical Review B*, 96(5):054501, 2017.

[77] AH Castro Neto. Charge density wave, superconductivity, and anomalous metallic behavior in 2D transition metal dichalcogenides. *Physical review letters*, 86(19):4382, 2001.

[78] Héctor Ochoa, Ricardo Zarzuela, and Yaroslav Tserkovnyak. Emergent gauge fields from curvature in single layers of transition-metal dichalcogenides. *Physical review letters*, 118(2):026801, 2017.

[79] Xiaofeng Qian, Junwei Liu, Liang Fu, and Ju Li. Quantum spin Hall effect in two-dimensional transition metal dichalcogenides. *Science*, 346(6215):1344–1347, 2014.

[80] Yu Saito, Tsutomu Nojima, and Yoshihiro Iwasa. Highly crystalline 2D superconductors. *Nature Reviews Materials*, 2(1):16094, 2017.

[81] Xiaodong Xu, Wang Yao, Di Xiao, and Tony F Heinz. Spin and pseudospins in layered transition metal dichalcogenides. *Nature Physics*, 10(5):343, 2014.

[82] Xiaoxiang Xi, Zefang Wang, Weiwei Zhao, Ju-Hyun Park, Kam Tuen Law, Helmuth Berger, László Forró, Jie Shan, and Kin Fai Mak. Ising pairing in superconducting $NbSe_2$ atomic layers. *Nature Physics*, 12(2):139, 2016.

[83] F Kadijk, R Huisman, and F Jellinek. Niobium and tantalum diselenides. *Recueil des Travaux Chimiques des Pays-Bas*, 83(7):768–775, 1964.

[84] F Kadijk and F Jellinek. On the polymorphism of niobium diselenide. *Journal of the Less Common Metals*, 23(4):437–441, 1971.

[85] Andrea Splendiani, Liang Sun, Yuanbo Zhang, Tianshu Li, Jonghwan Kim, Chi-Yung Chim, Giulia Galli, and Feng Wang. Emerging photoluminescence in monolayer MoS_2. *Nano letters*, 10(4):1271–1275, 2010.

[86] Gui-Bin Liu, Wen-Yu Shan, Yugui Yao, Wang Yao, and Di Xiao. Three-band tight-binding model for monolayers of group-VIB transition metal dichalcogenides. *Physical Review B*, 88(8):085433, 2013.

[87] Kai Xu, Zhenxing Wang, Xiaolei Du, Muhammad Safdar, Chao Jiang, and Jun He. Atomic-layer triangular WSe_2 sheets: synthesis and layer-dependent photoluminescence property. *Nanotechnology*, 24(46):465705, 2013.

[88] Zongyou Yin, Hai Li, Hong Li, Lin Jiang, Yumeng Shi, Yinghui Sun, Gang Lu, Qing Zhang, Xiaodong Chen, and Hua Zhang. Single-layer MoS_2 phototransistors. *ACS nano*, 6(1):74–80, 2011.

[89] RS Sundaram, M Engel, A Lombardo, R Krupke, AC Ferrari, Ph Avouris, and M Steiner. Electroluminescence in single layer MoS_2. *Nano letters*, 13(4):1416–1421, 2013.

[90] Goki Eda and Stefan A Maier. Two-dimensional crystals: managing light for optoelectronics. *ACS nano*, 7(7):5660–5665, 2013.

[91] Philipp Tonndorf, Robert Schmidt, Philipp Böttger, Xiao Zhang, Janna Börner, Andreas Liebig, Manfred Albrecht,

Christian Kloc, Ovidiu Gordan, Dietrich RT Zahn, et al. Photoluminescence emission and raman response of monolayer MoS_2, $MoSe_2$, and WSe_2. *Optics express*, 21(4):4908–4916, 2013.

[92] Weijie Zhao, Zohreh Ghorannevis, Leiqiang Chu, Minglin Toh, Christian Kloc, Ping-Heng Tan, and Goki Eda. Evolution of electronic structure in atomically thin sheets of WS_2 and WSe_2. *ACS nano*, 7(1):791–797, 2012.

[93] Namphung Peimyoo, Jingzhi Shang, Chunxiao Cong, Xiaonan Shen, Xiangyang Wu, Edwin KL Yeow, and Ting Yu. Nonblinking, intense two-dimensional light emitter: monolayer WS_2 triangles. *ACS nano*, 7(12):10985–10994, 2013.

[94] Néstor Perea-López, Ana Laura Elías, Ayse Berkdemir, Andres Castro-Beltran, Humberto R Gutiérrez, Simin Feng, Ruitao Lv, Takuya Hayashi, Florentino López-Urías, Sujoy Ghosh, et al. Photosensor device based on few-layered WS_2 films. *Advanced Functional Materials*, 23(44):5511–5517, 2013.

[95] Jing-Kai Huang, Jiang Pu, Chang-Lung Hsu, Ming-Hui Chiu, Zhen-Yu Juang, Yung-Huang Chang, Wen-Hao Chang, Yoshihiro Iwasa, Taishi Takenobu, and Lain-Jong Li. Large-area synthesis of highly crystalline WSe_2 monolayers and device applications. *ACS nano*, 8(1):923–930, 2013.

[96] He Tian, Matthew L Chin, Sina Najmaei, Qiushi Guo, Fengnian Xia, Han Wang, and Madan Dubey. Optoelectronic devices based on two-dimensional transition metal dichalcogenides. *Nano Research*, 9(6):1543–1560, 2016.

[97] Di Xiao, Gui-Bin Liu, Wanxiang Feng, Xiaodong Xu, and Wang Yao. Coupled spin and valley physics in monolayers of MoS_2 and other group VI dichalcogenides. *Physical review letters*, 108(19):196802, 2012.

[98] Wolfgang Nolting. *Theoretical Physics 7: Quantum Mechanics-Methods and Applications*. Springer, 2017.

[99] M Vijayakumar and MS Gopinathan. Spin-orbit coupling constants of transition metal atoms and ions in density functional theory. *Journal of Molecular Structure: THEOCHEM*, 361(1-3):15–19, 1996.

[100] G Nicolay, F Reinert, S Hüfner, and P Blaha. Spin-orbit splitting of the L-gap surface state on Au (111) and Ag (111). *Physical Review B*, 65(3):033407, 2001.

[101] Roland Winkler. Spin-orbit coupling effects in two-dimensional electron and hole systems. *Springer Tracts in Modern Physics*, 191:1–8, 2003.

[102] Miki Nagano, Ayaka Kodama, T Shishidou, and T Oguchi. A first-principles study on the Rashba effect in surface systems. *Journal of Physics: Condensed Matter*, 21(6):064239, 2009.

[103] Lars Petersen and Per Hedegård. A simple tight-binding model of spin–orbit splitting of sp-derived surface states. *Surface science*, 459(1-2):49–56, 2000.

[104] Guru Khalsa, Byounghak Lee, and Allan H MacDonald. Theory of t_{2g} electron-gas Rashba interactions. *Physical Review B*, 88(4):041302, 2013.

[105] S LaShell, BAa McDougall, and E Jensen. Spin splitting of an Au (111) surface state band observed with angle resolved photoelectron spectroscopy. *Physical review letters*, 77(16):3419, 1996.

[106] H. Nakamura et al. Spin splitting and strain in epitaxial monolayer WSe_2 on graphene. *To be submitted*, 2019.

[107] A Kumar and PK Ahluwalia. Electronic structure of transition metal dichalcogenides monolayers 1H-MX_2 (M= Mo,

W; X= S, Se, Te) from ab-initio theory: new direct band gap semiconductors. *The European Physical Journal B*, 85(6):186, 2012.

[108] Yilei Li, Alexey Chernikov, Xian Zhang, Albert Rigosi, Heather M Hill, Arend M van der Zande, Daniel A Chenet, En-Min Shih, James Hone, and Tony F Heinz. Measurement of the optical dielectric function of monolayer transition-metal dichalcogenides: MoS_2, $MoSe_2$, WS_2, and WSe_2. *Physical Review B*, 90(20):205422, 2014.

[109] Aurelien Manchon, Hyun Cheol Koo, Junsaku Nitta, SM Frolov, and RA Duine. New perspectives for Rashba spin–orbit coupling. *Nature materials*, 14(9):871, 2015.

[110] Francisco Guinea, MI Katsnelson, and AK Geim. Energy gaps and a zero-field quantum Hall effect in graphene by strain engineering. *Nature Physics*, 6(1):30, 2010.

[111] N Levy, SA Burke, KL Meaker, M Panlasigui, A Zettl, F Guinea, AH Castro Neto, and MF Crommie. Strain-induced pseudo–magnetic fields greater than 300 tesla in graphene nanobubbles. *Science*, 329(5991):544–547, 2010.

[112] R Suzuki, M Sakano, YJ Zhang, R Akashi, D Morikawa, A Harasawa, K Yaji, K Kuroda, K Miyamoto, T Okuda, et al. Valley-dependent spin polarization in bulk MoS_2 with broken inversion symmetry. *Nature nanotechnology*, 9(8):611, 2014.

[113] Aaron M Jones, Hongyi Yu, Nirmal J Ghimire, Sanfeng Wu, Grant Aivazian, Jason S Ross, Bo Zhao, Jiaqiang Yan, David G Mandrus, Di Xiao, et al. Optical generation of excitonic valley coherence in monolayer WSe_2. *Nature nanotechnology*, 8(9):634, 2013.

[114] John R Schaibley, Hongyi Yu, Genevieve Clark, Pasqual Rivera, Jason S Ross, Kyle L Seyler, Wang Yao, and Xi-

aodong Xu. Valleytronics in 2D materials. *Nature Reviews Materials*, 1(11):16055, 2016.

[115] Wei Han. Perspectives for spintronics in 2D materials. *APL Materials*, 4(3):032401, 2016.

[116] Kasun Premasiri and Xuan PA Gao. Tuning spin-orbit coupling in 2D materials for spintronics: a topical review. *Journal of Physics: Condensed Matter*, 31(19):193001, 2019.

[117] Liang Fu and Charles L Kane. Superconducting proximity effect and Majorana fermions at the surface of a topological insulator. *Physical review letters*, 100(9):096407, 2008.

[118] Roman M Lutchyn, Jay D Sau, and S Das Sarma. Majorana fermions and a topological phase transition in semiconductor-superconductor heterostructures. *Physical review letters*, 105(7):077001, 2010.

[119] Satoshi Sasaki, Zhi Ren, AA Taskin, Kouji Segawa, Liang Fu, and Yoichi Ando. Odd-parity pairing and topological superconductivity in a strongly spin-orbit coupled semiconductor. *Physical review letters*, 109(21):217004, 2012.

[120] Jelena Klinovaja, Peter Stano, Ali Yazdani, and Daniel Loss. Topological superconductivity and Majorana fermions in RKKY systems. *Physical review letters*, 111(18):186805, 2013.

[121] Lin Wang, Tomas Orn Rosdahl, and Doru Sticlet. Platform for nodal topological superconductors in monolayer molybdenum dichalcogenides. *Physical Review B*, 98(20):205411, 2018.

[122] CWJ Beenakker. Search for Majorana fermions in superconductors. *Annu. Rev. Condens. Matter Phys.*, 4(1):113–136, 2013.

[123] Peter Fulde and Richard A Ferrell. Superconductivity in a strong spin-exchange field. *Physical Review*, 135(3A):A550, 1964.

[124] AI Larkin and IUN Ovchinnikov. Inhomogeneous state of superconductors(Production of superconducting state in ferromagnet with Fermi surfaces, examining Green function). *Soviet Physics-JETP*, 20:762–769, 1965.

[125] Zhen Zheng, Ming Gong, Xubo Zou, Chuanwei Zhang, and Guangcan Guo. Route to observable Fulde-Ferrell-Larkin-Ovchinnikov phases in three-dimensional spin-orbit-coupled degenerate Fermi gases. *Physical Review A*, 87(3):031602, 2013.

[126] Gil Young Cho, Jens H Bardarson, Yuan-Ming Lu, and Joel E Moore. Superconductivity of doped Weyl semimetals: Finite-momentum pairing and electronic analog of the 3He-A phase. *Physical Review B*, 86(21):214514, 2012.

[127] Keliang He, Nardeep Kumar, Liang Zhao, Zefang Wang, Kin Fai Mak, Hui Zhao, and Jie Shan. Tightly bound excitons in monolayer WSe$_2$. *Physical review letters*, 113(2):026803, 2014.

[128] Xiao-Xiao Zhang, Yumeng You, Shu Yang Frank Zhao, and Tony F Heinz. Experimental evidence for dark excitons in monolayer WSe$_2$. *Physical review letters*, 115(25):257403, 2015.

[129] JP Echeverry, B Urbaszek, Thierry Amand, Xavier Marie, and IC Gerber. Splitting between bright and dark excitons in transition metal dichalcogenide monolayers. *Physical Review B*, 93(12):121107, 2016.

[130] Xiao-Xiao Zhang, Ting Cao, Zhengguang Lu, Yu-Chuan Lin, Fan Zhang, Ying Wang, Zhiqiang Li, James C Hone, Joshua A Robinson, Dmitry Smirnov, et al. Magnetic

brightening and control of dark excitons in monolayer WSe$_2$. *Nature nanotechnology*, 12(9):883, 2017.

[131] K Sugawara, T Sato, Y Tanaka, S Souma, and T Takahashi. Spin-and valley-coupled electronic states in monolayer WSe$_2$ on bilayer graphene. *Applied Physics Letters*, 107(7):071601, 2015.

[132] Sung-Kwan Mo, Choongyu Hwang, Yi Zhang, Mauro Fanciulli, Stefan Muff, J Hugo Dil, Zhi-Xun Shen, and Zahid Hussain. Spin-resolved photoemission study of epitaxially grown MoSe$_2$ and WSe$_2$ thin films. *Journal of Physics: Condensed Matter*, 28(45):454001, 2016.

[133] Hai Li, Gang Lu, Yanlong Wang, Zongyou Yin, Chunxiao Cong, Qiyuan He, Lu Wang, Feng Ding, Ting Yu, and Hua Zhang. Mechanical Exfoliation and Characterization of Single-and Few-Layer Nanosheets of WSe$_2$, TaS$_2$, and TaSe$_2$. *Small*, 9(11):1974–1981, 2013.

[134] Wei Liu, Jiahao Kang, Deblina Sarkar, Yasin Khatami, Debdeep Jena, and Kaustav Banerjee. Role of metal contacts in designing high-performance monolayer n-type WSe$_2$ field effect transistors. *Nano letters*, 13(5):1983–1990, 2013.

[135] H Sahin, Sefaattin Tongay, S Horzum, W Fan, J Zhou, J Li, J Wu, and FM Peeters. Anomalous Raman spectra and thickness-dependent electronic properties of WSe$_2$. *Physical Review B*, 87(16):165409, 2013.

[136] Hai Li, Jumiati Wu, Zongyou Yin, and Hua Zhang. Preparation and applications of mechanically exfoliated single-layer and multilayer MoS$_2$ and WSe$_2$ nanosheets. *Accounts of chemical research*, 47(4):1067–1075, 2014.

[137] Wei Zhe Teo, Elaine Lay Khim Chng, Zdeněk Sofer, and Martin Pumera. Cytotoxicity of exfoliated transition-metal

dichalcogenides (MoS_2, WS_2, and WSe_2) is lower than that of graphene and its analogues. *Chemistry–A European Journal*, 20(31):9627–9632, 2014.

[138] M Koperski, K Nogajewski, A Arora, V Cherkez, P Mallet, J-Y Veuillen, J Marcus, P Kossacki, and M Potemski. Single photon emitters in exfoliated WSe_2 structures. *Nature nanotechnology*, 10(6):503, 2015.

[139] Carmen C Mayorga-Martinez, Adriano Ambrosi, Alex Yong Sheng Eng, Zdeněk Sofer, and Martin Pumera. Transition metal dichalcogenides (MoS_2, $MoSe_2$, WS_2 and WSe_2) exfoliation technique has strong influence upon their capacitance. *Electrochemistry Communications*, 56:24–28, 2015.

[140] Hema CP Movva, Amritesh Rai, Sangwoo Kang, Kyounghwan Kim, Babak Fallahazad, Takashi Taniguchi, Kenji Watanabe, Emanuel Tutuc, and Sanjay K Banerjee. High-mobility holes in dual-gated WSe_2 field-effect transistors. *ACS nano*, 9(10):10402–10410, 2015.

[141] Ajit Srivastava, Meinrad Sidler, Adrien V Allain, Dominik S Lembke, Andras Kis, and A Imamoğlu. Optically active quantum dots in monolayer WSe_2. *Nature nanotechnology*, 10(6):491, 2015.

[142] Babak Fallahazad, Hema CP Movva, Kyounghwan Kim, Stefano Larentis, Takashi Taniguchi, Kenji Watanabe, Sanjay K Banerjee, and Emanuel Tutuc. Shubnikov–de Haas oscillations of high-mobility holes in monolayer and bilayer WSe_2: Landau level degeneracy, effective mass, and negative compressibility. *Physical review letters*, 116(8):086601, 2016.

[143] Hao Li, Lei Ye, and Jianbin Xu. High-performance broadband floating-base bipolar phototransistor based on

WSe$_2$/BP/MoS$_2$ heterostructure. *Acs Photonics*, 4(4):823–829, 2017.

[144] Hema CP Movva, Babak Fallahazad, Kyounghwan Kim, Stefano Larentis, Takashi Taniguchi, Kenji Watanabe, Sanjay K Banerjee, and Emanuel Tutuc. Density-Dependent Quantum Hall States and Zeeman Splitting in Monolayer and Bilayer WSe$_2$. *Physical review letters*, 118(24):247701, 2017.

[145] Zefang Wang, Jie Shan, and Kin Fai Mak. Valley-and spin-polarized Landau levels in monolayer WSe$_2$. *Nature nanotechnology*, 12(2):144, 2017.

[146] Janghyuk Kim, Michael A Mastro, Marko J Tadjer, and Jihyun Kim. Heterostructure WSe$_2$-Ga$_2$O$_3$ junction field-effect transistor for low-dimensional high-power electronics. *ACS applied materials & interfaces*, 10(35):29724–29729, 2018.

[147] Kyounghwan Kim, Nitin Prasad, Hema CP Movva, G William Burg, Yimeng Wang, Stefano Larentis, Takashi Taniguchi, Kenji Watanabe, Leonard F Register, and Emanuel Tutuc. Spin-Conserving Resonant Tunneling in Twist-Controlled WSe$_2$-hBN-WSe$_2$ Heterostructures. *Nano letters*, 18(9):5967–5973, 2018.

[148] Chang-Hsiao Chen, Chun-Lan Wu, Jiang Pu, Ming-Hui Chiu, Pushpendra Kumar, Taishi Takenobu, and Lain-Jong Li. Hole mobility enhancement and p-doping in monolayer WSe$_2$ by gold decoration. *2D Materials*, 1(3):034001, 2014.

[149] Liang Chen, Bilu Liu, Ahmad N Abbas, Yuqiang Ma, Xin Fang, Yihang Liu, and Chongwu Zhou. Screw-dislocation-driven growth of two-dimensional few-layer and pyramid-like WSe$_2$ by sulfur-assisted chemical vapor deposition. *ACS nano*, 8(11):11543–11551, 2014.

[150] Chunming Huang, Sanfeng Wu, Ana M Sanchez, Jonathan JP Peters, Richard Beanland, Jason S Ross, Pasqual Rivera, Wang Yao, David H Cobden, and Xiaodong Xu. Lateral heterojunctions within monolayer MoSe$_2$–WSe$_2$ semiconductors. *Nature materials*, 13(12):1096, 2014.

[151] Hailong Zhou, Chen Wang, Jonathan C Shaw, Rui Cheng, Yu Chen, Xiaoqing Huang, Yuan Liu, Nathan O Weiss, Zhaoyang Lin, Yu Huang, et al. Large area growth and electrical properties of p-type WSe$_2$ atomic layers. *Nano letters*, 15(1):709–713, 2014.

[152] Jianyi Chen, Bo Liu, Yanpeng Liu, Wei Tang, Chang Tai Nai, Linjun Li, Jian Zheng, Libo Gao, Yi Zheng, Hyun Suk Shin, et al. Chemical Vapor Deposition of Large-Sized Hexagonal WSe$_2$ Crystals on Dielectric Substrates. *Advanced Materials*, 27(42):6722–6727, 2015.

[153] Sarah M Eichfeld, Lorraine Hossain, Yu-Chuan Lin, Aleksander F Piasecki, Benjamin Kupp, A Glen Birdwell, Robert A Burke, Ning Lu, Xin Peng, Jie Li, et al. Highly scalable, atomically thin WSe$_2$ grown via metal–organic chemical vapor deposition. *ACS nano*, 9(2):2080–2087, 2015.

[154] Yongji Gong, Sidong Lei, Gonglan Ye, Bo Li, Yongmin He, Kunttal Keyshar, Xiang Zhang, Qizhong Wang, Jun Lou, Zheng Liu, et al. Two-step growth of two-dimensional WSe$_2$/MoSe$_2$ heterostructures. *Nano letters*, 15(9):6135–6141, 2015.

[155] Ming-Yang Li, Yumeng Shi, Chia-Chin Cheng, Li-Syuan Lu, Yung-Chang Lin, Hao-Lin Tang, Meng-Lin Tsai, Chih-Wei Chu, Kung-Hwa Wei, Jr-Hau He, et al. Epitaxial growth of a monolayer WSe$_2$-MoS$_2$ lateral pn junction with an atomically sharp interface. *Science*, 349(6247):524–528, 2015.

[156] Bilu Liu, Mohammad Fathi, Liang Chen, Ahmad Abbas, Yuqiang Ma, and Chongwu Zhou. Chemical vapor deposition growth of monolayer WSe_2 with tunable device characteristics and growth mechanism study. *Acs Nano*, 9(6):6119–6127, 2015.

[157] Yuqiang Ma, Bilu Liu, Anyi Zhang, Liang Chen, Mohammad Fathi, Chenfei Shen, Ahmad N Abbas, Mingyuan Ge, Matthew Mecklenburg, and Chongwu Zhou. Reversible semiconducting-to-metallic phase transition in chemical vapor deposition grown monolayer WSe_2 and applications for devices. *ACS nano*, 9(7):7383–7391, 2015.

[158] Chendong Zhang, Yuxuan Chen, Amber Johnson, Ming-Yang Li, Lain-Jong Li, Patrick C Mende, Randall M Feenstra, and Chih-Kang Shih. Probing critical point energies of transition metal dichalcogenides: surprising indirect gap of single layer WSe_2. *Nano letters*, 15(10):6494–6500, 2015.

[159] Sarah M Eichfeld, Víctor Oliveros Colon, Yifan Nie, Kyeongjae Cho, and Joshua A Robinson. Controlling nucleation of monolayer WSe_2 during metal-organic chemical vapor deposition growth. *2D Materials*, 3(2):025015, 2016.

[160] Kyoung-Duck Park, Omar Khatib, Vasily Kravtsov, Genevieve Clark, Xiaodong Xu, and Markus B Raschke. Hybrid tip-enhanced nanospectroscopy and nanoimaging of monolayer WSe_2 with local strain control. *Nano letters*, 16(4):2621–2627, 2016.

[161] Malleswararao Tangi, Pawan Mishra, Chien-Chih Tseng, Tien Khee Ng, Mohamed Nejib Hedhili, Dalaver H Anjum, Mohd Sharizal Alias, Nini Wei, Lain-Jong Li, and Boon S Ooi. Band alignment at GaN/single-layer WSe_2 interface. *ACS applied materials & interfaces*, 9(10):9110–9117, 2017.

[162] Xiaotian Zhang, Tanushree H Choudhury, Mikhail Chubarov, Yu Xiang, Bhakti Jariwala, Fu Zhang, Nasim

Alem, Gwo-Ching Wang, Joshua A Robinson, and Joan M Redwing. Diffusion-Controlled Epitaxy of Large Area Coalesced WSe$_2$ Monolayers on Sapphire. *Nano letters*, 18(2):1049–1056, 2018.

[163] HJ Liu, L Jiao, L Xie, F Yang, JL Chen, WK Ho, CL Gao, JF Jia, XD Cui, and MH Xie. Molecular-beam epitaxy of monolayer and bilayer WSe$_2$: a scanning tunneling microscopy/spectroscopy study and deduction of exciton binding energy. *2D Materials*, 2(3):034004, 2015.

[164] Kleopatra Emmanouil Aretouli, Dimitra Tsoutsou, Polychronis Tsipas, Jose Marquez-Velasco, Sigiava Aminalragia Giamini, Nicolaos Kelaidis, Vassilis Psycharis, and Athanasios Dimoulas. Epitaxial 2D SnSe$_2$/2D WSe$_2$ van der Waals heterostructures. *ACS applied materials & interfaces*, 8(35):23222–23229, 2016.

[165] Jun Hong Park, Suresh Vishwanath, Xinyu Liu, Huawei Zhou, Sarah M Eichfeld, Susan K Fullerton-Shirey, Joshua A Robinson, Randall M Feenstra, Jacek Furdyna, Debdeep Jena, et al. Scanning tunneling microscopy and spectroscopy of air exposure effects on molecular beam epitaxy grown WSe$_2$ monolayers and bilayers. *ACS nano*, 10(4):4258–4267, 2016.

[166] Masaki Nakano, Yue Wang, Yuta Kashiwabara, Hideki Matsuoka, and Yoshihiro Iwasa. Layer-by-Layer Epitaxial Growth of Scalable WSe$_2$ on Sapphire by Molecular Beam Epitaxy. *Nano letters*, 17(9):5595–5599, 2017.

[167] V Yu Fominski, SN Grigoriev, Jean-Pierre Celis, RI Romanov, and VB Oshurko. Structure and mechanical properties of W–Se–C/diamond-like carbon and W–Se/diamond-like carbon bi-layer coatings prepared by pulsed laser deposition. *Thin Solid Films*, 520(21):6476–6483, 2012.

[168] SN Grigoriev, V Yu Fominski, AG Gnedovets, and RI Romanov. Experimental and numerical study of the chemical composition of WSe_x thin films obtained by pulsed laser deposition in vacuum and in a buffer gas atmosphere. *Applied Surface Science*, 258(18):7000–7007, 2012.

[169] V Yu Fominski, SN Grigoriev, AG Gnedovets, and RI Romanov. On the mechanism of encapsulated particle formation during pulsed laser deposition of WSe_x thin-film coatings. *Technical Physics Letters*, 39(3):312–315, 2013.

[170] SN Grigoriev, V Yu Fominski, RI Romanov, AG Gnedovets, and MA Volosova. Shadow masked pulsed laser deposition of WSe_x films: Experiment and modeling. *Applied Surface Science*, 282:607–614, 2013.

[171] Tamie AJ Loh, Daniel HC Chua, and Andrew TS Wee. One-step synthesis of few-layer WS_2 by pulsed laser deposition. *Scientific reports*, 5:18116, 2015.

[172] Tamie AJ Loh and Daniel HC Chua. Origin of hybrid 1T-and 2H-WS_2 ultrathin layers by pulsed laser deposition. *The Journal of Physical Chemistry C*, 119(49):27496–27504, 2015.

[173] Zhaoqiang Zheng, Tanmei Zhang, Jiandomg Yao, Yi Zhang, Jiarui Xu, and Guowei Yang. Flexible, transparent and ultra-broadband photodetector based on large-area WSe_2 film for wearable devices. *Nanotechnology*, 27(22):225501, 2016.

[174] Farman Ullah, Yumin Sim, Chinh Tam Le, Maeng-Je Seong, Joon I Jang, Sonny H Rhim, Bien Cuong Tran Khac, Koo-Hyun Chung, Kibog Park, Yangjin Lee, et al. Growth and Simultaneous Valleys Manipulation of Two-Dimensional $MoSe_2$-WSe_2 Lateral Heterostructure. *ACS nano*, 11(9):8822–8829, 2017.

[175] H Terrones, E Del Corro, S Feng, JM Poumirol, D Rhodes, D Smirnov, NR Pradhan, Z Lin, MAT Nguyen, AL Elias, et al. New first order Raman-active modes in few layered transition metal dichalcogenides. *Scientific reports*, 4:4215, 2014.

[176] Weijie Zhao, Zohreh Ghorannevis, Kiran Kumar Amara, Jing Ren Pang, Minglin Toh, Xin Zhang, Christian Kloc, Ping Heng Tan, and Goki Eda. Lattice dynamics in mono-and few-layer sheets of WS_2 and WSe_2. *Nanoscale*, 5(20):9677–9683, 2013.

[177] Duy Le, Alexei Barinov, Edwin Preciado, Miguel Isarraraz, Iori Tanabe, Takashi Komesu, Conrad Troha, Ludwig Bartels, Talat S Rahman, and Peter A Dowben. Spin–orbit coupling in the band structure of monolayer WSe_2. *Journal of Physics: Condensed Matter*, 27(18):182201, 2015.

[178] Adrien Allain and Andras Kis. Electron and hole mobilities in single-layer WSe_2. *ACS nano*, 8(7):7180–7185, 2014.

[179] Dirk J Groenendijk, Michele Buscema, Gary A Steele, Steffen Michaelis de Vasconcellos, Rudolf Bratschitsch, Herre SJ van der Zant, and Andres Castellanos-Gomez. Photovoltaic and photothermoelectric effect in a double-gated WSe_2 device. *Nano letters*, 14(10):5846–5852, 2014.

[180] Douglas H Lowndes, DB Geohegan, AA Puretzky, DP Norton, and CM Rouleau. Synthesis of novel thin-film materials by pulsed laser deposition. *Science*, 273(5277):898–903, 1996.

[181] DB Chrisey, A Pique, RA McGill, JS Horwitz, BR Ringeisen, DM Bubb, and PK Wu. Laser deposition of polymer and biomaterial films. *Chemical Reviews*, 103(2):553–576, 2003.

[182] Sebastian Fa, Hans-Ulrich Krebs, et al. Calculations and experiments of material removal and kinetic energy during pulsed laser ablation of metals. *Applied surface science*, 96:61–65, 1996.

[183] PR Willmott and JR Huber. Pulsed laser vaporization and deposition. *Reviews of Modern Physics*, 72(1):315, 2000.

[184] T Scharf and HU Krebs. Influence of inert gas pressure on deposition rate during pulsed laser deposition. *Applied Physics A*, 75(5):551–554, 2002.

[185] Udo W Pohl. *Epitaxy of Semiconductors: Introduction to Physical Principles*. Springer Science & Business Media, 2013.

[186] Jens Als-Nielsen and Des McMorrow. *Elements of modern X-ray physics*. John Wiley & Sons, 2011.

[187] Jo Bo Nelson and DP Riley. An experimental investigation of extrapolation methods in the derivation of accurate unit-cell dimensions of crystals. *Proceedings of the Physical Society*, 57(3):160, 1945.

[188] Lyman G Parratt. Surface studies of solids by total reflection of x-rays. *Physical review*, 95(2):359, 1954.

[189] Francisco Tiago Leitao Muniz, Marcus Aurélio Ribeiro Miranda, Cássio Morilla dos Santos, and José Marcos Sasaki. The scherrer equation and the dynamical theory of X-ray diffraction. *Acta Crystallographica Section A: Foundations and Advances*, 72(3):385–390, 2016.

[190] What is a synchrotron? https://www.esrf.eu/about/synchrotron-science/synchrotron, May 2019.

[191] Peter Blaha, Karlheinz Schwarz, Georg KH Madsen, Dieter Kvasnicka, and Joachim Luitz. wien2k. *An augmented*

plane wave+ local orbitals program for calculating crystal properties, 2001.

[192] John P Perdew, Kieron Burke, and Matthias Ernzerhof. Generalized gradient approximation made simple. *Physical review letters*, 77(18):3865, 1996.

[193] John P Perdew and Yue Wang. Accurate and simple analytic representation of the electron-gas correlation energy. *Physical Review B*, 45(23):13244, 1992.

[194] Satoru Ichinokura. *Observation of Superconductivity in Epitaxially Grown Atomic Layers: In Situ Electrical Transport Measurements.* Springer, 2017.

[195] Andrea C Ferrari and Denis M Basko. Raman spectroscopy as a versatile tool for studying the properties of graphene. *Nature nanotechnology*, 8(4):235, 2013.

[196] Amit S Pawbake, Mahendra S Pawar, Sandesh R Jadkar, and Dattatray J Late. Large area chemical vapor deposition of monolayer transition metal dichalcogenides and their temperature dependent Raman spectroscopy studies. *Nanoscale*, 8(5):3008–3018, 2016.

[197] Elena del Corro, A Botello-Méndez, Yannick Gillet, Ana Laura Elias, Humberto Terrones, Simin Feng, Cristiano Fantini, Daniel Rhodes, Narayan Pradhan, Luis Balicas, et al. Atypical exciton–phonon interactions in WS_2 and WSe_2 monolayers revealed by resonance raman spectroscopy. *Nano letters*, 16(4):2363–2368, 2016.

[198] Xin Zhang, Xiao-Fen Qiao, Wei Shi, Jiang-Bin Wu, De-Sheng Jiang, and Ping-Heng Tan. Phonon and Raman scattering of two-dimensional transition metal dichalcogenides from monolayer, multilayer to bulk material. *Chemical Society Reviews*, 44(9):2757–2785, 2015.

[199] Humberto R Gutiérrez, Nestor Perea-López, Ana Laura Elías, Ayse Berkdemir, Bei Wang, Ruitao Lv, Florentino López-Urías, Vincent H Crespi, Humberto Terrones, and Mauricio Terrones. Extraordinary room-temperature photoluminescence in triangular WS_2 monolayers. *Nano letters*, 13(8):3447–3454, 2012.

[200] Michiko Kusunoki, Wataru Norimatsu, Jianfeng Bao, Koichi Morita, and Ulrich Starke. Growth and features of epitaxial graphene on SiC. *Journal of the Physical Society of Japan*, 84(12):121014, 2015.

[201] Th Finteis, M Hengsberger, Th Straub, K Fauth, R Claessen, P Auer, P Steiner, S Hüfner, P Blaha, M Vögt, et al. Occupied and unoccupied electronic band structure of WSe_2. *Physical Review B*, 55(16):10400, 1997.

[202] Jonathon Mark Riley, Worawat Meevasana, Lewis Bawden, M Asakawa, T Takayama, T Eknapakul, TK Kim, M Hoesch, S-K Mo, H Takagi, et al. Negative electronic compressibility and tunable spin splitting in WSe_2. *Nature nanotechnology*, 10(12):1043, 2015.

[203] Stefano Agnoli, Alberto Ambrosetti, Tevfik Onur Mentes, Alessandro Sala, Andrea Locatelli, Pier Luigi Silvestrelli, Mattia Cattelan, Sarah Eichfeld, Donna D Deng, Joshua A Robinson, et al. Unraveling the Structural and Electronic Properties at the WSe_2–Graphene Interface for a Rational Design of van der Waals Heterostructures. *ACS Applied Nano Materials*, 1(3):1131–1140, 2018.

[204] Rui Zhang, Vasileios Koutsos, and Rebecca Cheung. Elastic properties of suspended multilayer WSe_2. *Applied Physics Letters*, 108(4):042104, 2016.

[205] Samir Mammadov, Jürgen Ristein, Julia Krone, Christian Raidel, Martina Wanke, Veit Wiesmann, Florian Speck,

and Thomas Seyller. Work function of graphene multilayers on SiC (0001). *2D Materials*, 4(1):015043, 2017.

[206] Eslam Khalaf. Mesoscopic phenomena in topological insulators, superconductors and semimetals. 2017.

[207] Igor Žutić, Jaroslav Fabian, and S Das Sarma. Spintronics: Fundamentals and applications. *Reviews of modern physics*, 76(2):323, 2004.

[208] R J Elliott. Theory of the effect of spin-orbit coupling on magnetic resonance in some semiconductors. *Physical Review*, 96(2):266, 1954.

[209] Y Yafet. g–Factors and spin-lattice relaxation of conduction electrons. In *Solid state physics*, volume 14, pages 1–98. Elsevier, 1963.

[210] Yu A Bychkov and É I Rashba. Properties of a 2D electron gas with lifted spectral degeneracy. *JETP lett*, 39(2):78, 1984.

[211] Gene Dresselhaus. Spin-orbit coupling effects in zinc blende structures. *Physical Review*, 100(2):580, 1955.

List of Figures

List of Tables

List of publications

1. A. Mohammed, H. Nakamura, P. Wochner, S. Ibrahimkutty, A. Schulz, K. Müller, U. Starke, B. Stuhlhofer, G. Cristiani, G. Logvenov, and H. Takagi. Pulsed laser deposition for the synthesis of monolayer WSe$_2$. *Appl. Phys. Lett.*, 111, 073101, 2017.

2. H. Nakamura, A. Mohammed, Ph. Rosenzweig, K. Matsuda, K. Nowakowski, K. Küster, P. Wochner, S. Ibrahimkutty, U. Wedig, H. Hussain, J. Rawle, C. Nicklin, B. Stuhlhofer, G. Cristiani, G. Logvenov, H. Takagi, and U. Starke. Spin splitting and strain in epitaxial monolayer WSe$_2$ on graphene. *Phys. Rev. B*, 101, 165103, 2020.

Acknowledgement

This thesis work is the result of many different people with varying degree of contributions. I could not have completed this work without the support and guidance of Prof. Hidenori Takagi and Dr. Hiroyuki Nakamura. They have been a constant feedback for my gradual development, both academically and personally. They taught me the skills to accomplish high quality work and more importantly, taught me how to unlearn. In addition, they provided an opportunity to acquire Japanese work culture and patience to maintain the momentum towards a set goal. I'm thankful for the work environment they provided throughout my time at Max Planck Institute in Stuttgart.

Dr. Gennady Logvenov and his group were instrumental in the design and development of the *hybrid*-pulsed laser deposition (h-PLD) system which is the heart of the present work. Georg Cristiani and Benjamin Stuhlhofer helped me with the technical details, installation and running of the h-PLD system. This work could not have lifted off without their critical support, later joined by Kathrin Pflaum. Prof. Dr. Ulrich Starke and his students provided high quality monolayer graphene substrates and performed ARPES measurements. Dr. Mitsuharu Konuma and Dr. Kathrin Müller supported the work with XPS and UPS measurements. We thank Dr. Peter Wochner for his wonderful support and guidance for the efficient use of synchrotron beamtimes. Shyjumon Ibrahimkutty for his occasional shouts to protect Pila-

tus during our synchrotron beamtimes. We thank the supporting staff at both ANKA, Germany and Diamond Light Source, UK during our beam times. Armin Schulz helped us with the Raman spectroscopy and the analysis. Grateful to the directors at the MPI FKF and IS for providing a lively environment for the exchange of scientific ideas. In addition, I should thank them for allowing me to use some of their instruments when required for my thesis work.

Quite a lot of other people were also helpful with their experience and technical know-how. Their support made my work hassle free, enjoyable, and an interesting learning experience. Everyone from our Takagi group were reliable and greatly helpful when needed. Administrative staff helped me with the infamous German bureaucracy, especially Sabine Paulsen, Birgit King and Frank Gottschalk. Thanks to Ulrich Wedig and Ulrike Niemann for helping helping me with the German translation.

I'm fortunate to be surrounded by so many brilliant students who helped me in ways difficult to express in words. My journey to this point could not have been possible without the help of my friends and family. My mother Khamar Shahani and brother Yousuf Ali were strong moral support along with my maternal grandmother who passed away in the last stage of this writing, as well as support of other family members. Whereas my friends Kansel, Sandra, Friederike and Milena turned out to be irreplaceable The four quarter worth having than the hundred cents. Finally, I thank my medical team who helped me keep my sanity intact.